Energie & Umwelt
Energy & Environment

274

Thermochemical Modeling of Laves Phase Containing Ferritic Steels

Aurélie Jacob

Member of the Helmholtz Association

JÜLICH FORSCHUNGSZENTRUM

Energie & Umwelt / Energy & Environment
Band / Volume 274
ISBN 978-3-95806-070-8

JÜLICH FORSCHUNGSZENTRUM

Thermochemical Modeling of Laves Phase Containing Ferritic Steels

Aurélie Jacob

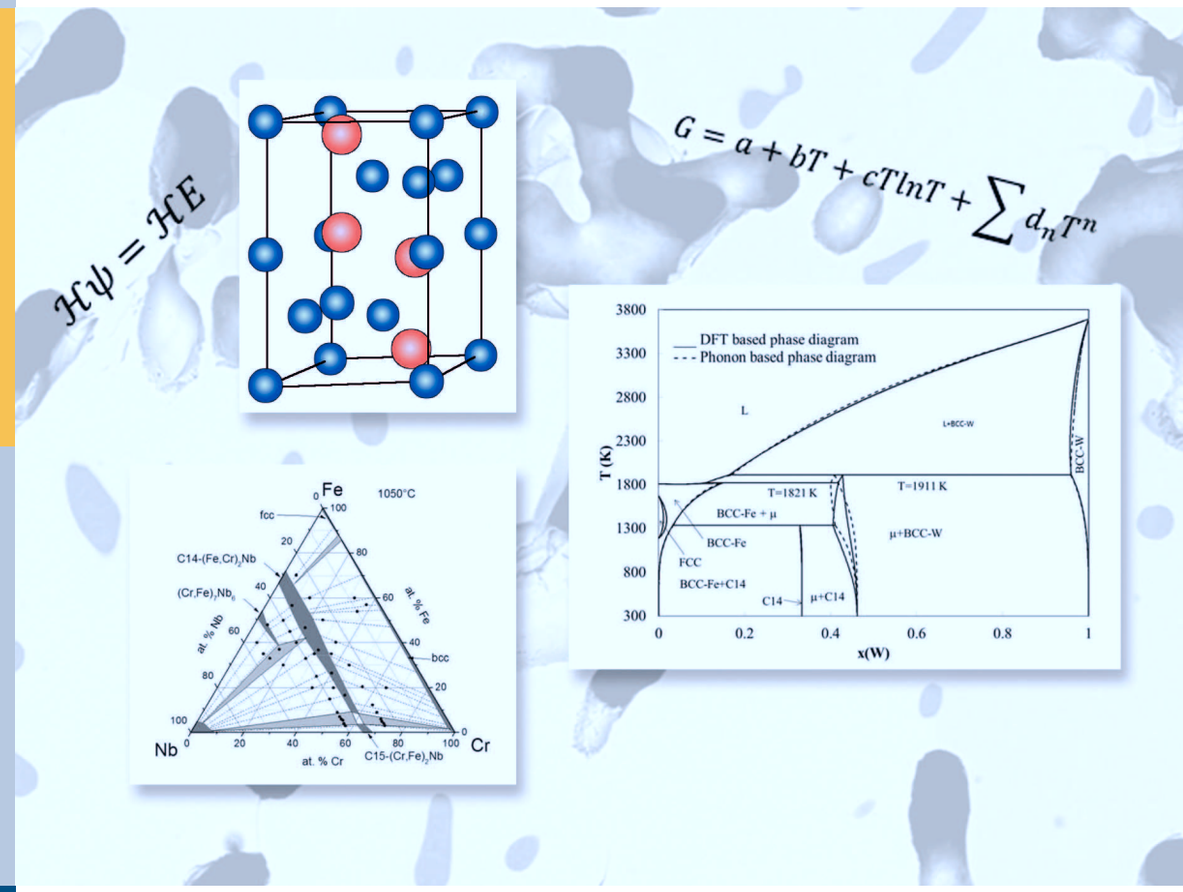

Energie & Umwelt / Energy & Environment
Band / Volume 274
ISBN 978-3-95806-070-8

JÜLICH FORSCHUNGSZENTRUM

Schriften des Forschungszentrums Jülich
Reihe Energie & Umwelt / Energy & Environment Band / Volume 274

Forschungszentrum Jülich GmbH
Institute of Energy and Climate Research (IEK)
Microstructure and Properties of Materials (IEK-2)

Thermochemical Modeling of Laves Phase Containing Ferritic Steels

Aurélie Jacob

Schriften des Forschungszentrums Jülich
Reihe Energie & Umwelt / Energy & Environment Band / Volume 274

ISSN 1866-1793 ISBN 978-3-95806-070-8

Bibliographic information published by the Deutsche Nationalbibliothek.
The Deutsche Nationalbibliothek lists this publication in the Deutsche Nationalbibliografie; detailed bibliographic data are available in the Internet at http://dnb.d-nb.de.

Publisher and Distributor: Forschungszentrum Jülich GmbH
Zentralbibliothek
52425 Jülich
Tel: +49 2461 61-5368
Fax: +49 2461 61-6103
Email: zb-publikation@fz-juelich.de
www.fz-juelich.de/zb

Cover Design: Grafische Medien, Forschungszentrum Jülich GmbH

Printer: Grafische Medien, Forschungszentrum Jülich GmbH

Schriften des Forschungszentrums Jülich
Reihe Energie & Umwelt / Energy & Environment, Band / Volume 274

D 82 (Diss. RWTH Aachen University, 2015)

ISSN 1866-1793
ISBN 978-3-95806-070-8

The complete volume is freely available on the Internet on the Jülicher Open Access Server (JuSER) at www.fz-juelich.de/zb/openaccess.

Abstract

For energy technology, development of new materials is required to be used for boiler and steam turbines with high thermal cyclability, creep strength and excellent corrosion resistance in steam and high temperatures and also at downtime in water. Crofer 22H, a new kind of steel jointly developed at Forschungszentrum Juelich and Thyssen Krupp, has already shown promising results in laboratory tests. The formation of Laves phase particles improves the materials' properties such as creep strength while the high Cr-content of 22 % provides excellent corrosion resistance. Unfortunately, the formation of Laves phase competes with the formation of other phases. In order to further improve this type of ferritic steels, knowledge of thermodynamics of the intermetallic systems forming the Laves phases $(Fe,Cr,Si)_2(Nb,W)$ is required for the calculation of phase stability as a function of composition and temperature. The Calphad method is of great help for the calculation of phase stability in technical materials. This kind of calculation is based on thermodynamic databases. Calculations with the commercial steel database have shown to be inaccurate since not all considered alloy systems have been modeled up to now. The present work aims to provide a thermodynamic optimization of the systems containing Laves phases.

Thermodynamic data of Laves phase containing systems were obtained by the Calphad method with an optimization of the sub-systems containing Laves phases. The Calphad method relies on the input data for the considered system, their quality and their quantity are of primary importance for the obtained thermodynamic assessment. In the present work, several methods have been used in order to provide consistent thermodynamic calculations of the phase equilibria.

A combined experimental and modeling approach was chosen to determine the phase equilibria and thermodynamic properties in the systems Fe-W, Cr-Fe-Nb and Fe-Nb-Si. DFT calculations were done for all mentioned systems for the determination of the energy of formation of the compounds through the chosen model. In the Fe-W system, in addition to the DFT calculations which are restricted to 0 K, phonon calculations were performed in order to obtain the temperature dependence of the Gibbs energies which were used to improve the Calphad modeling.

Kurzfassung

Für Anwendungen in der Energietechnik werden kriechfeste und korrosionsbeständige Hochtemperaturwerkstoffe auf Eisenbasis benötigt, die zukünftig in Dampfturbinen und Kesseln eingesetzt werden, um möglichst hohe Lastflexibilität, Zyklierfähigkeit und Korrosionsfestigkeit sowohl im Betrieb als auch bei Stillstand zu gewährleisten. Während die gegenwärtig eingesetzten Werkstoffe im Wesentlichen auf ferritisch-/martensitischem Gefüge mit 9-12 % Chrom beruhen, bieten Lavesphasenverstärkte ferritische Werkstoffe mit 15-22 % Chrom das Potential nicht nur für Anwendungstemperaturen bis zu 650 °C, sondern weisen auch ausgezeichnete Korrosionsbeständigkeit in Wasserdampf und in wässrigen Lösungen auf.

Das Problem bei der Entwicklung derartiger Werkstoffe besteht darin, dass die entsprechenden Phasendiagramme vielfach nur bedingt bekannt sind und entsprechende thermochemische Daten über die infrage kommenden Lavesphasen und ihre Zusammensetzung fehlen, um mittels der Calphadmethode die entsprechenden Zustandsdiagramme zu berechnen.

Mittels DFT-Methoden ergänzt durch experimentelle Untersuchungen ist es möglich, die fehlenden Daten und Zusammensetzungen zu bestimmen und die Genauigkeit sowohl der experimentell ermittelten, als auch der mittels Calphad berechneten Zustandsdiagramme erheblich zu verbessern.

Auf diese Weise ist es gelungen, die Phasengleichgewichte in den binären Systemen Fe-W, Cr-Nb sowie den ternären Systemen Cr-Fe-Nb und Fe-Nb-Si zu bestimmen. Für die in diesen Systemen auftretenden Lavesphasen wurden die thermochemischen Eigenschaften mittels DFT bestimmt, für das System Fe-W wurden zusätzlich zu den DFT-Berechnungen Phononen-Berechnungen durchgeführt, um die Temperaturabhängigkeit der Bildungsenergie zu berücksichtigen, was für die Anwendung bei hohen Temperaturen von besonderer Bedeutung ist.

Contents

[illegible]

[illegible]

[illegible] λ [illegible]

[illegible]

2. [illegible]

σ

μ

μ

Introduction

The development of new materials is one of the technology challenges of this century especially in the conversion of energy. Indeed with a decrease of the natural resources and an increase of the demand, there is a necessity of improving the efficiency of the actual technology and to develop new ones. For the provision of energy, fossil fuels remain a secure provision for the next decades to change the energy supply system. Improvement of the efficiency of the actual technology is required to extend the provision of the primary resources. The efficiency of the technology allows also a reduction of the footprint on the environment. An improvement of the efficiency has so two advantages: reduction of the amount of fuel and reduction of CO_2 for the global warming.

For an improvement of the efficiency up to 50 % for steam power plants, the necessary conditions of vapor pressure would be around 700 °C/300 bars. The use of ferritic martensitic steels with respect to creep strength for steam power plants applications is limited to about 600 to 620°C. New steels with a high chromium content of around 20 % with intermetallic Laves phase particles dispersed in a ferritic matrix have shown to be potentially good candidates due to their good creep strength and oxidation behavior. In contrast to the ferritic martensitic steels they have a high corrosion resistance at downtime.

Many technologies are involved in the process of the development of new materials. The development of new materials for an industrial application relies on the prediction of the behavior of the material under working condition. For example, if the material is used under the sea (e.g. offshore wind power) or in high sea level (e.g. gas turbine for plane), the working conditions are different, in the first corrosion issue due to the salt has to be taken into account and in the second high modification of the working temperature. In both cases, it is necessary to know the behavior of the material to predict its working time and its cost. For a fastest development of material with a specific task it is necessary to understand its behavior. The behavior of materials under operating conditions can nowadays easily be predicted using

σ

Scope of the work

Iron based alloys can be used for high temperature materials. In presence of carbon, the alloy forms steel. Steels are well known materials since antiquity but it is since the 18th century that industrial production of steels has been done.

There are different kinds of steel, e.g. ferritic, austenitic and ferritic-martensitic. They differ by their composition, microstructure and crystal structures. Ferritic-martensitic steels with 9-12 % Cr are used in steam power plants working below 600°C. Increasing the working temperature would allow an improvement of the efficiency of the process, but these types of materials fail due to an increase of creep and of the oxidation rates. Instead austenitic steels and Ni-alloys can be used but these materials are expensive and prone thermo-mechanical fatigue degradation due to their higher thermal expansion coefficients compared to ferritic and ferritic-martensitic steels.

Ferritic-martensitic steels with higher Cr content than 12 % show to be potentially good candidate for high temperature but exhibit lower creep strength. An interesting approach of steel design is to add some elements forming Laves phases [2]. Indeed the precipitation of Laves phase in high chromium ferritic steels improves tensile, creep and oxidation properties. Such new ferritic steel has been developed in the IEK-2 institute at Forschungszentrum Jülich and commercialized under the name Crofer 22H® [1].

The Laves phases in Crofer 22H are due to the addition of Nb and W as well as Si to compare the Crofer AP® [3]. In presence of Fe and Cr, the Laves phases (Fe,Cr,Si)(Nb,W) form as fine precipitates dispersed in the ferritic steel matrix improving the materials properties such as creep and yield strength and oxidation behavior. In laboratory, this new kind of steel has shown to be potentially a good candidate for uses in steam power plants. Nevertheless, the promising results obtained were not reproducible at the industrial scale. It is supposed to be due to a competition with the formation of σ

Chapter I – Contents of the study

I. Ferritic steel

A ferritic steel for high temperature applications, Crofer 22H [1], has been developed as an interconnector materials for advanced SOFC systems. It belongs to the second generation of this type of materials developed at Forschungszentrum Juelich.

The first generation Crofer 22 AP exhibits excellent oxidation resistance over long operation time without significant loss in electric conductivity. This can be attributed to the extremely low content of Si and Al, which tend to form internal oxides as well as the subscale oxide layers especially of SiO_2. These oxide layers exhibit very low electric conductivity resulting in high degradation of SOFC components. These high losses in electronic conductivity can be generated by low Al and Si contents in the interconnector steels.

The disadvantage of low Al and Si contents is that Crofer 22AP has to be produced using technologies like vacuum or inert gas melt which are expensive. The addition of Nb and Si results in formation of Nb-silicides in the steel, which are stable enough to prevent a subscale silica formation below chromia layers and pick up dissolved oxygen. This allows to avoid the use of conventional costly technologies. Addition of W results in increased creep strength of this type of Laves reinforced steels which has been designated Crofer 22H [1].

Crofer 22H [1] is a ferritic steel with high chromium content (20 mol%). Due to its good creep and corrosion resistance, Crofer 22H is also a potential candidate for application in combustion power plants as steam turbine. In ferritic steel the good strength comes from chromium based carbides [6]. Instead the high temperature strength can be improved by the presence of Laves phases. The precipitation of Laves phase in the matrix of ferritic steel is due the presence of the alloying elements W and Nb. These two elements play a role on the improvement of the creep resistance, oxidation behavior and strength compared with the previous steel of the same type, Crofer 22 AP [7]. These two elements in

Table 1 . Furthermore the presence of Si favors the precipitation of Laves phase in the matrix of the ferritic steel.

	Fe	Cr	C	N	S	Mn	Si	Al	W	Nb	Ti	La	P	Cu
At.%	**65.68**	**21.12**	**0.006**	**0.007**	**0.003**	**0.74**	**0.29**	**0.046**	**9.33**	**1.57**	**0.16**	**0.47**	**0.02**	**0.54**

Table 1 - Composition of Crofer 22H ® in atomic %. Source: http://www.fcdic.com/ja/member/data/Crofer22H.pdf

It has been shown that the presence of precipitates like Laves phase containing Nb and W improves the yield strength by a factor of 1.4 at 600 °C and 2.7 at 800 °C [7] and improve considerably the creep resistance [2,7]. The good behavior of the Crofer 22H found in the laboratory could not be reproduced at the industrial scale. It has been found that there is a competition between the precipitation of the Laves phase and several unwanted carbides and nitrides [2,4] that deteriorate the material properties.

The composition of the Laves phase forming in the Crofer 22H has been experimentally determined by Kuhn et al. [2] using a model alloy with a composition close to that from the Crofer 22H. The composition of the AB_2 Laves phase is given in the Table 2.

	Fe	*Cr*	*Si*	*Nb*	*W*
Mol %	*53.29*	*12.93*	*4.128*	*19.36*	*11.83*

Table 2 – Composition of the Laves phase in the Crofer 22H determined experimentally by Kuhn et al. [2].

Using the Thermo-Calc software [8] it has been shown that there is no perceptible solubility of Si in the Laves phase [2] whereas W-solubility is overestimated [6]. The absence of Si in the Laves phase is explained by the missing thermodynamic data in the database. Nevertheless, silicon plays a significant role on the dissolution, grain growth and stability of the Laves phase.

II. Literature survey

1. Laves phases

Laves phases have been discovered by James Friauf in 1927, and then investigation of these intermetallic phases have been done by Laves, Schulze and co-workers. Schulze who was working in Dresden (Democratic Republic of Germany at that time) was very active in the research of Laves phases but the cold war prevented to show the results to the international community and most of the work has been forgotten or lost. A recent review [9] showed some of the results made during this time. More recently the Max Plank Society has run a research initiative called "The Nature of Laves" and focused on different aspects of Laves phases. The work made on the properties of Laves phases has been extensively published, some parts have been reviewed by Stein and co-workers [10,11] and some general trends on the properties of Laves phases have been established.

Laves phases form the largest group of intermetallic phases, more than 1400 for binary and ternary systems [10] are documented. Laves phases show topological close-packed structures and they crystallize within the formula AB_2. There are three different polytypes: the cubic $MgCu_2$ type (strukturbericht designation C15), the hexagonal $MgZn_2$ type (C14) and the hexagonal $MgNi_2$ type (C36). Their crystal structures are closely related: they can be described by different stacking sequences of the same types of layers. The crystalline structures are represented in *Figure 1. In each of the three kinds of Laves phase, the coordination number (CN) is 16 for A (CN_{A-A}=4, CN_{A-B}=12) and 12 for B (CN_{B-A}=6, CN_{B-B}=6).*

C15 type Cu_2Mg Fd-3m	C14 type $MgZn_2$ $P6_3/mmc$	C36 type $MgNi_2$ $P6_3/mmc$
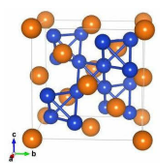	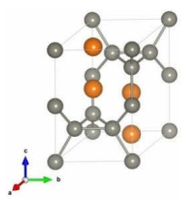	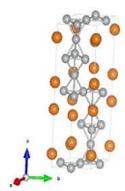
Cu: 16d (5/8, 5/8, 5/8) **Mg**: 8a (0, 0, 0)	**Mg**: 4f (1/3, 2/3, z) **Zn**: 2a (0, 0, 0) 6h (x, 2x, 1/4)	**Mg:** 4e (0, 0, z) 4f (1/3, 2/3, z) **Ni:** 4f (1/3, 2/3, z) 6g (1/2, 0, 0) 6h (x, 2x, 1/4)

Figure 1 – Structure models and crystallography of the three different Laves phase polytypes.

The Laves phases form with specific requirements, e.g. the radii of the two elements forming them are related by $r_A/r_B = (3/2)^{1/2} = 1.225$ (ideal radius ratio), a specific valence electron concentration (see *Figure 2*) and electroneutrality. These three parameters are the most important properties for the formation of Laves phases. Some relations have been established between the formation of the type of Laves phase, the ideal radius and the electron concentration. In fact Laves phases form with a radius ratio between 1.05 and 1.68 [12] because the true radius differs from the Goldschmidt ideal radius [13]. Depending on the valence electron concentrations (*Figure 2*), a specific polytype of the Laves phase is preferred, but there are many exceptions. The C36 polytype is often described as metastable (in many systems) and is a transition phase between the C14 and C15 polytypes [14].

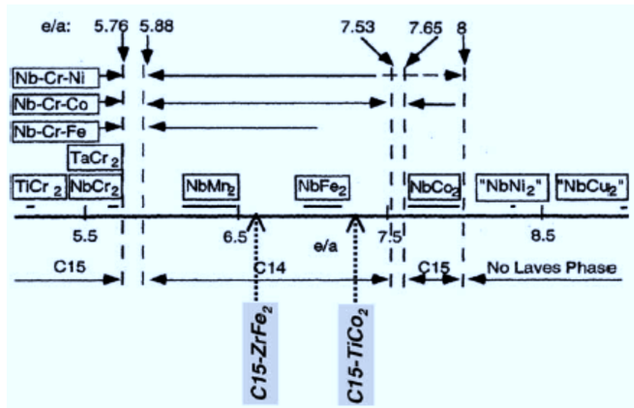

Figure 2 – Scheme of the stability of the Laves phase polytypes as function as the valence electron concentration according to [10].

From binary to ternary systems, different ways are possible for the formation of Laves phases. In the present work, there is evidence of binary C14 or C15 Laves phase $(Fe,Cr,Si)_2(Nb,W)$ depending on the concentration of the elements, and these are the most common Laves phase polytypes. The dissolution of a third element presents different advantages [11]:

- promotion of the formation of Laves phase,
- higher stability of the Laves phase.

There are high solubilities of a third element (Si or Al) in C14 phases (e.g. Fe-Nb-Si [15], Fe-Nb-Al [16]) and a modification of the polytype from C15 in the binary to C14 by addition of Si or Al in different ternary systems (e.g. Cr-Nb-Si [17], Cr-Nb-Al [18]).

The polytypes depend on the elements forming the Laves phase. In both binary and ternary systems, it is possible to find the same polytype of Laves phase, and on the other side it is not possible to extrapolate from ternary to a binary systems [19]. Indeed, a third element may promote the formation of a certain

Table 2). Considering the five elements mentioned above, it can be formed the following systems:

- Binary: Fe-Nb, Fe-W, Cr-Nb

and

- Ternary Fe-Cr-Nb, Fe-Nb-Si, Fe-Si-W and Cr-Nb-Si.

Out of these different mentioned systems a careful literature survey has been done in the following part. In the present work, the interest is the development of a suitable thermodynamic database for the ferritic alloy Crofer 22H containing the different Laves phases as a function of temperature. Our interest has been focused in a first approach on the literature useful for the thermodynamic modeling of the different systems (i.e. experimental data, thermodynamic modeling).

2. Silicon in Laves phase

There are several studies about the role of addition of Si in steel and its role in the formation of Laves phase. Silicon plays a role on the nucleation and growth of the Laves phase [5]. In many ternary systems Si dissolves in the C14 Laves phase, stabilizing it due to the decrease of the electron concentration (e/a) [21,22]. In the case of a C15 Laves phase in a binary system, the presence of Si provokes a structural modification and allows the formation of C14.

3. Thermodynamic stability of Laves phase containing system

The literature survey includes experimental as well as theoretical knowledge on the different systems previously mentioned.

3.1 Cr-Nb

A lot of studies have been done on the Cr-Nb system due to its importance for Fe and Ni based alloys. The Landolt-Börnstein [23] and the Massalski [24] compilation of phase diagrams show the presence of two different polytypes of Laves phase C15 at low temperature and C14 at high temperature.

Costa Neto et al. [25] have done a thermodynamic assessment of this phase diagram using the available experimental data at that time. They considered the two polytypes of Laves phase (C14 and C15). The most recent calculated phase diagram calculation of this system is given by Paul [illegible]

[illegible] *Figure 3).*

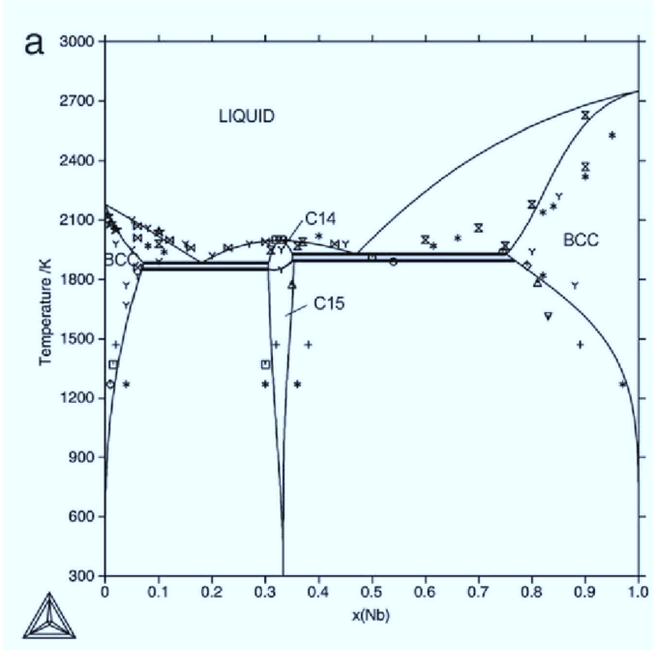

Figure 3 – Calculated phase diagram according to and from Pavlů et al. [26].

Figure 2 (or seen in the work of hu et al. [27] as well as in the review of Stein et al. [10]). In 2010, Aufrecht et al. [28] showed the metastability of the high temperature phases. Indeed until this time, the presence of C14 phase was extrapolated from higher order systems and some misinterpretation of results were done. In the case of Laves phase, a binary phase cannot be postulated from ternary or quaternary systems. A complete review of this system has been carried out during the time of the present work [29]. A new experimental investigation has been done by Stein et al. [18] following the investigation of Aufrecht [28] in order to check the melting temperatures of this system previously done

Table 3 is stable.

Phase	Pearson Symbol	Space Group	Prototype	Lattice parameters [Å]	Reference
Cr_2Nb	**cF24**	**Fd-3m (227)**	**Cu_2Mg**	**a=6.96**	**[23]**

Table 3 – Crystallographic information present the Cr-Nb binary system.

3.2 Fe-Nb

The paper of Paul et al. [31] reviewed the system with data which were available before 1[illegible]3. Using different experimental data from literature, Srikanth et al. [32] optimized the phase diagram and found a rather good agreement with experimental values. Thermodynamic assessment of the iron-niobium system was given using the Calphad method in 2000 by Toffolon and Servant [33]. Due to some disagreement between different assessments [3[illegible]] and experimental investigations [34] of this phase diagram, [illegible] et al. [3[illegible]] completely reinvestigated this system experimentally using EPMA, EDS, SEM and DTA. They determined the Curie temperature at T=1042K for a composition of Nb at 13.5 at. [illegible]. The system forms Laves phase (C14) by a congruent reaction at T=1[illegible]1[illegible]K and the μ [illegible]

Figure 4 and compared with experimental data.

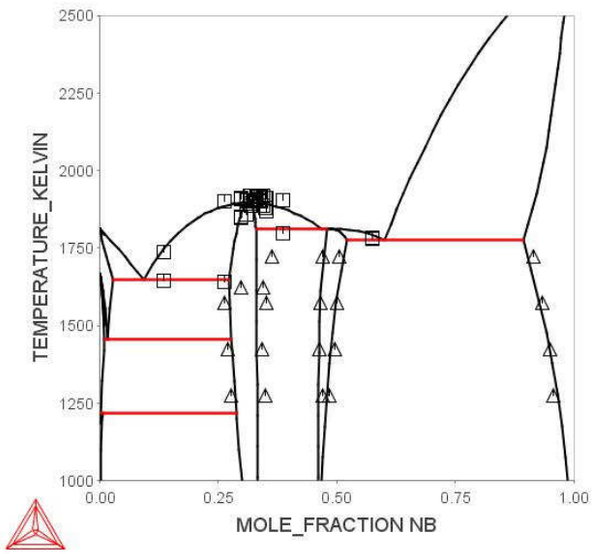

Figure 4 – Fe-Nb phase diagram calculated by Khvan et al. [40] *using the Calphad method compared with experimental data from EPMA (triangles) and DTA (squares)* [35].

In addition to the two pure elements forming BCC structure, there are the C14 Laves (Fe_2Nb) and the μ (Fe_7Nb_6) phases. The C14 Laves phase crystallizes in hexagonal structure as mentioned previously (Laves phases) and the μ phase has a rhombohedral structure. The lattice parameters as well as the Wyckoff position are developed in *Table 4*.

Phase	**Pearson Symbol**	**Space Group**	**Prototype**	**Lattice parameters [Å]**	**References**
Fe_2Nb	hP12	P63/mmc (no. 194)	$MgZn_2$	a=4.8414 c=7.8933	[20]
Fe_7Nb_6	hR39	R-3m (no. 166)	W_6Fe_7	a=4.926 c= 26.80	[41]

Table 4 – Crystallographic informations for the intermetallic phases present in Fe-Nb system.

3.3 Fe-W

The Fe-W system is of great interest as refractory alloy. Nevertheless due to the hardness and the high melting point of W, it is rather difficult to handle it experimentally. The literature shows some disagreement, indeed the Massalski's compilation of binary phase diagrams [24] and the Landolt-Börnstein [42,43] show two completely different phase diagrams.

In the original papers, there are also different interpretations of this phase diagram. In the version of Sinha et al. [44], they presented the existence of the Laves phase and of the μ [illegible] δ [illegible]

[illegible] Figure 5) similar to the work of Sinha et al. [44] and Kirchner et al. [45] but did not find the presence of δ [illegible] μ [illegible]

Figure 6. He based his thermodynamic assessment on the experimental phase diagram of Kostakis [49]. He pointed out that the results presented by Henig and Hofman [46] are dubious. This assessment is a reference for more complex systems and integrated into a commercial database (i.e. TCFE6). Nowadays the intermetallic phases are described by different models than the ones used by Gustafson [48].

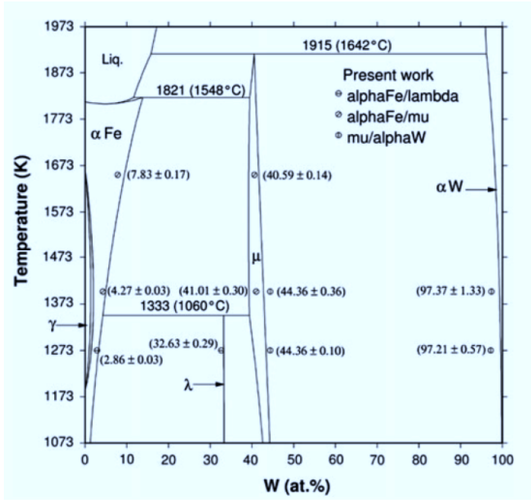

Figure 5 – Experimental phase diagram of Fe-W from [47].

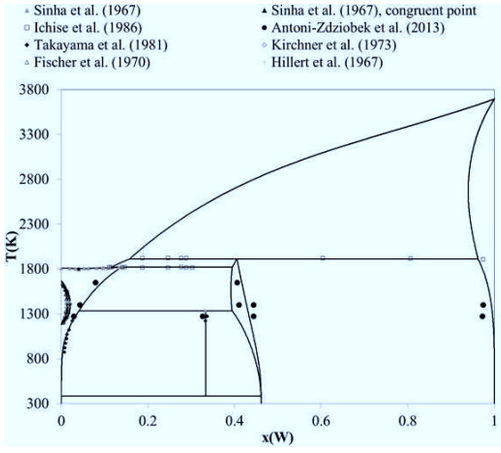

Figure 6 – Calculated phase diagram Fe-W [48] compared with experimental data.

As mentioned in the previous paragraph, there are two intermetallic phases in the Fe-W system, the Laves phase crystallising in C14 polytype and the μ *Table 5).*

Phase	Pearson Symbol	Space Group	Prototype	Lattice parameters [Å]	References
Fe_2W	hP12	P63/mmc (no. 194)	$MgZn_2$	a=4.731, c=7.70	[50]
Fe_7W_6	hR39	R-3m (no. 166)	W_6Fe_7	a=4.756 c= 25.728	[44]

Table 5 – Crystallographic data of the C14 laves phase in the Fe-W system as given by [44] and [50].

3.1 Cr-Nb-Si

Due to its technological importance the Cr-Nb-Si system has been extensively studied. The first experimental investigations have been carried out by Goldschmidt and Brandt [51]. They postulated in addition to the binary phases the presence of five ternary compounds. Some binary phases show a high extension into the ternary phase diagram. Chao et al. [52] used diffusion multiple method for the determination of the phase equilibria. They found only three ternary phases. Both versions of phase diagram disagree between themselves on many points as pointed out by Shao [53] who wanted to make a thermodynamic optimization of this system.

In addition to the binary phases, David et al. [17] described this system with four ternary compounds and made a new thermodynamic optimization based on their literature evaluation and some new experimental investigations using diffusion multiples.

Following these studies there were a lot of other investigations on this system to clarify the different controversies from previous studies. Liquidus projection on the Cr-Nb side was proposed by Bewlay et al. [54]. The last assessment on this system was done by David et al. [17] as shown in *Figure 7*. ***This system will not be further investigated in the present work. Nevertheless the thermodynamic assessment of this system would need to be reconsidered, due to new experimental knowledge (i.e. [54]) and the recent controversy in the literature on the Cr-Nb binary system (see [122]).***

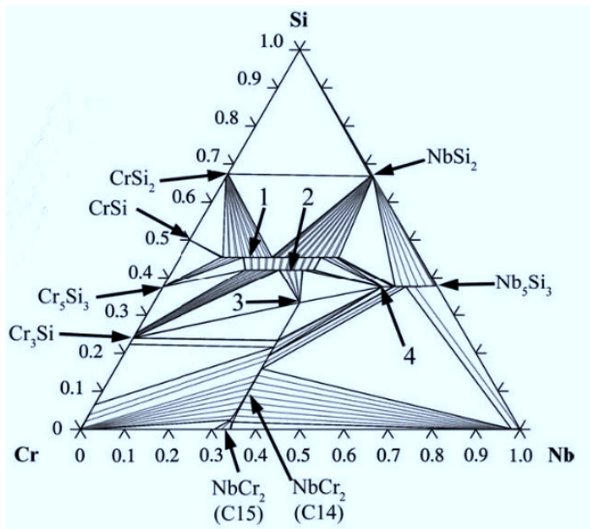

Figure 7 – Calculated isothermal section at 1473 K as given by David et al. [17] with the numbers 1=$(Cr,Nb)_6Si_5$, 2=$(Cr,Nb)_{11}Si_8$, 3=CrNbSi, 4=$CrNb_4Si_3$.

There are four different ternary compounds according to David et al. [17] The crystallography of the ternary compounds is given in Table 6.

Phase	Pearson Symbol	Space Group	Prototype	Lattice parameters [Å]	References
CrNbSi	hP9	P-6m	ZrNiAl	a=6.598 c=3.359	[55]
$CrNb_4Si_3$	tI32	I4/mcm	W_5Si_3	a=9.877 c=4.934	[56]
$Cr_4Nb_2Si_5$	oI44	Ibam	$Cr_4Nb_2Si_5$	a=15.81 b=7.497 c=4.879	[57]
$Cr_7Nb_4Si_8$	oP76	Pnma	$Cr_7Nb_4Si_8$	a=13.27 b=15.90 c=4.892	[58]

Table 6 – Crystallography of the ternary compounds of the Cr-Nb-Si system.

3.2 Fe-Nb-Si

Only few articles concern experimental data for this system. Most of the literature deals with crystallographic investigations of the numerous ternary compounds and solid solution phases found in this system. Goldschmidt [5] first proposed a version of the Fe-Nb-Si phase diagram (*Figure 8 ****). His investigation is incompatible with the actual knowledge of the Fe-Nb (i.e. postulation of σ*

Figure 9) into the ternary system and found a smaller extend into it (also in the binary Fe-Nb). They did not find a σ

Figure 10) studied the extension of the Laves and the μ

Figure 11.

As this system has primary importance for steel industry, new experimental investigations have been provided during the time of the present work. Wang et al. [15] studied three isothermal sections of the phase diagram and found six ternary compounds. The proposed isothermal section at 1373 K is given in Figure 12. Their investigation does not provide any data for the liquidus projection of the system which are nevertheless relevant informations for the thermodynamic optimization.

No thermodynamic assessment of this system is available in the literature. The calculation of an isothermal section using the commercial database TCFE6 is given in Figure 13. This representation of the phase diagram is incompatible with the actual knowledge of the phase diagram. The Laves phase is

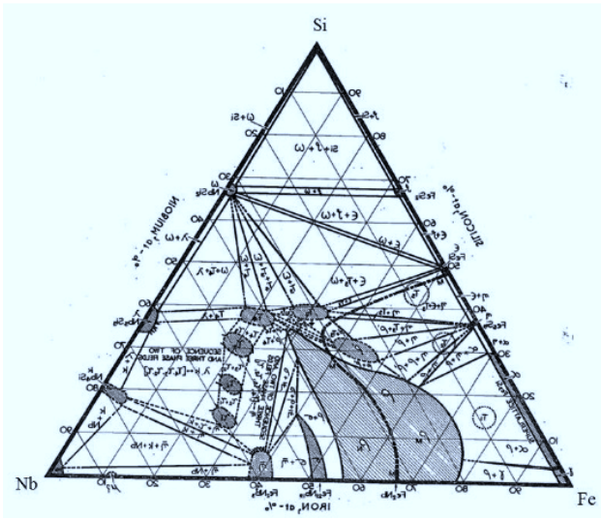

Figure 8 – Experimental phase diagram according to Goldschmidt [59], section at 1273K.

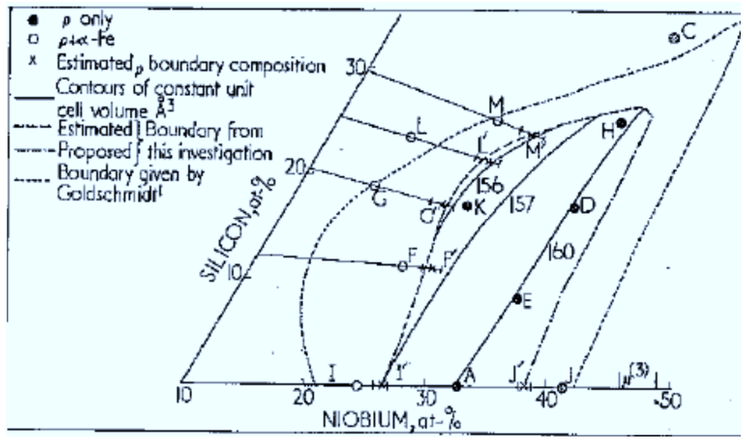

Figure 9 – Experimental phase diagram at 1573 K according to Denham [20].

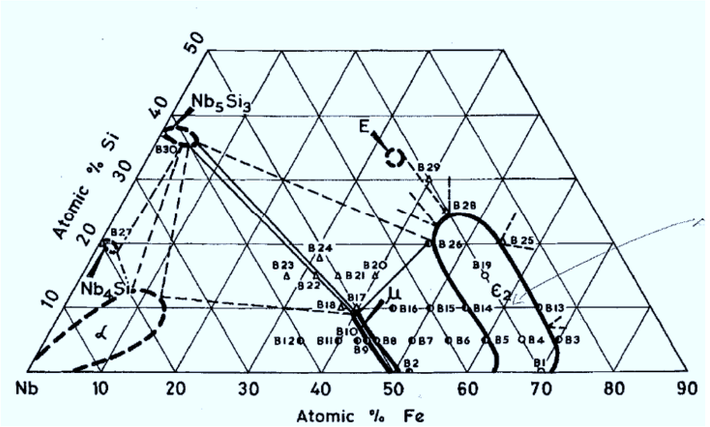

Figure 10 - Experimental phase diagram at 1373 K according to Singh [61].

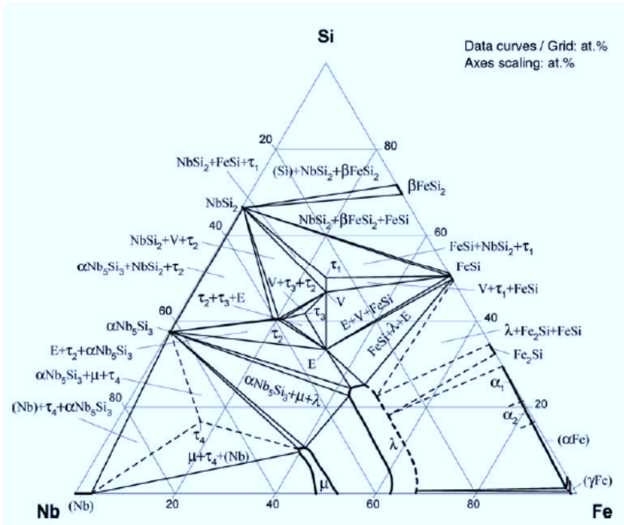

Figure 11 – Isothermal section of Fe-Nb-Si at 1423 K as proposed in Landolt-Börnstein [60].

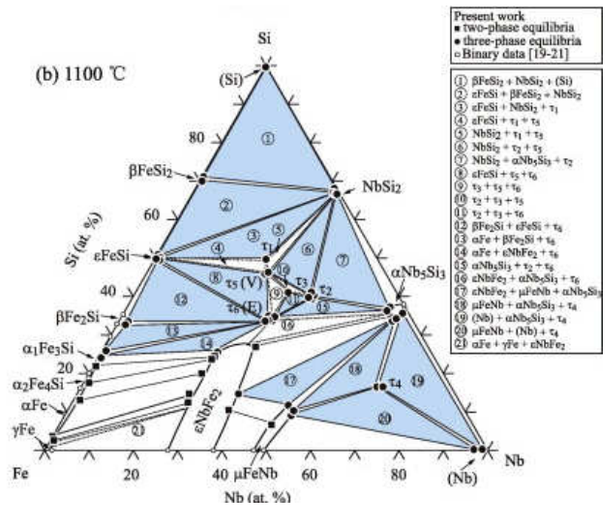

Figure 12 – Experimental phase diagram from Wang et al. [15] *at 1373 K.*

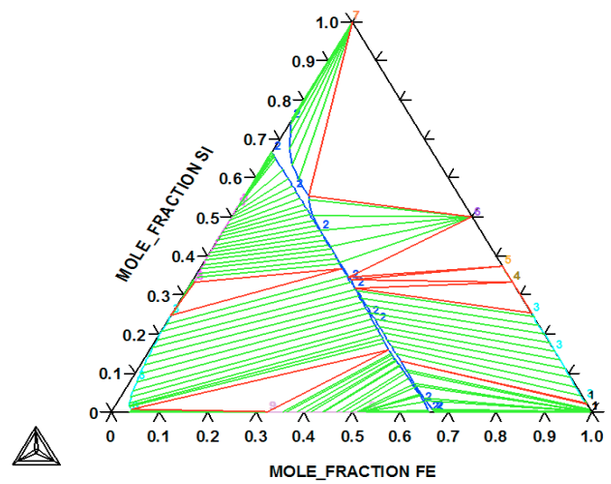

Figure 13 – Calculated phase diagram at 1323 K using the TCF6 database.

Figure 10). He showed that Si does not affect the symmetry of the crystal structure, only the lattice parameters changed. Si dissolves also in the μ

- FeNbSi
- $FeNbSi_2$
- $Fe_3Nb_4Si_5$
- $FeNb_4Si$
- $Fe_4Nb_4Si_7$
- $FeNb_2Si_2$

The crystal structures of the different compounds are reported below (*Table 7*) *with their respective references.*

Phase	Pearson Symbol	Space Group	Prototype	Lattice parameters [Å]	References
$FeNbSi_2$	**oP48**	**Pbam(55)**	**$ZrCrSi_2$**	**a=7.576 b=9.733 c=7.576**	**[55]**
$Fe_4Nb_4Si_7$	**tI60**	**I4/mmm (139)**	**$Zr_4Co_4Ge_7$**	**a=12.652 c=4.981**	**Landolt Börnstein [60] based on [63]**
FeNbSi	**oP12**	**Pnma(62)**	**TiNiSi**	**a=6.231 b=3.677 c=7.190**	**[63]**
$FeNb_2Si_2$	**tP198**	**$P4_2/mcm$ (132)**	**Co_2Si**	**a=23.76 c=4.959**	**[62]**
$Fe_3Nb_4Si_5$	**hP12**	**P63/mmc (194)**	**$MgZn_2$**	**a=4.868 c=7.758**	**[64]**
$FeNb_4Si$	**tP12**	**P4/mcc (124)**	**Nb_4CoSi**	**a=6.193 c=5.056**	**[65]**

Table 7 – Crystal structures of the ternary compounds present in the Fe-Nb-Si phase equilibria.

3.3 Cr-Fe-Nb

The first study concerning the Cr-Fe-Nb phase diagram has been proposed by Kaloev et al. [66] with an isothermal section at 1000°C (*Figure 14*). Later they published a second isothermal section at 700°C [67] (*Figure 15*). This phase diagram is characterized by huge solid solution of the two binary Laves phases formed by Fe_2Nb-Cr_2Nb.

Gujicic et al. [68] studied the influence of Fe in the C15-Cr_2Nb Laves phase. They observed a change of polytype structure at low Fe content (> 7 at. % of Fe). This change of polytype is due to a change in the electron concentration. Nevertheless, in the literature there are no informations for the liquidus projection as well for the reaction scheme diagram. Further experimental investigations are necessary for a good thermodynamic optimization of this system.

There is no ternary compound mentioned in the literature up to now.

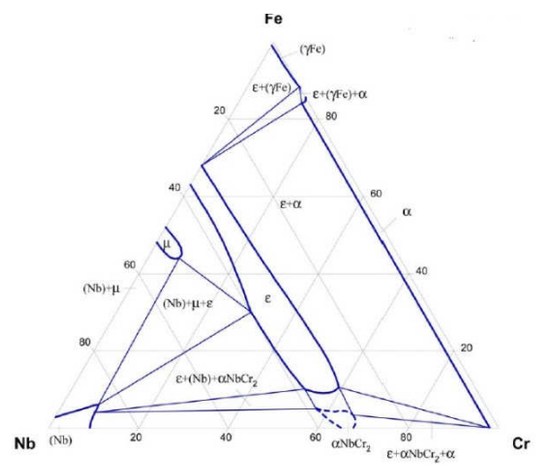

Figure 14 - Isothermal section at 1273K given by Kaloev [66] *according to the Landolt-Börnstein database* [69].

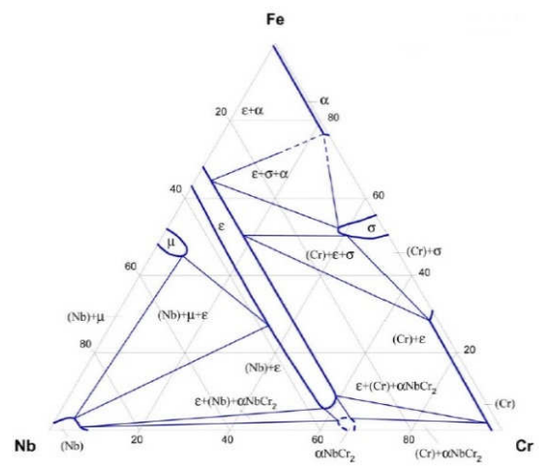

Figure 15 - Isothermal section at 973K given by Kaloev [67] *according to the Landolt-Börnstein database* [69].

3.4 Fe-W-Si

The Fe-W-Si phase diagram is of great interest for industrial processes due to the hardness and refractory properties of W. Adding tungsten in ferritic steel improves the material properties like hardness, hot strength and yield strength. The Landolt-Bönrstein [70] (*Figure 16*) gives a brief overview of the work that has been done. An older review from Raynor et al. [71] gives a larger overview of the system and shows the complexity of this ternary system. Most of their review is based on the work of Vogel et al. [72]. Using all available information they have made some tentative of an isotherm and a complex reaction scheme based on their actual knowledge. They mentioned the presence of two ternary compounds (FeW_2Si and FeWSi) which form from the reactions between Fe_7W_6 and FeSi.

The calculated phase diagram from the commercial database TCFE6 given in *Figure 17* shows disagreement with the phase diagram proposed in the literature. It has to be mentioned that no assessment of this system exists in the literature and this calculation is an extrapolation from binary systems.

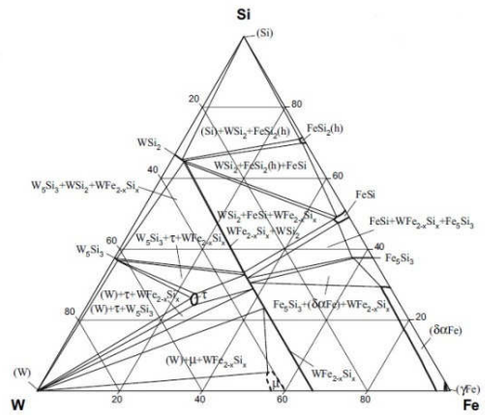

Figure 16 - Experimental isothermal section at T=1273K of Fe-W-Si according to Landölt-Bornstein [70].

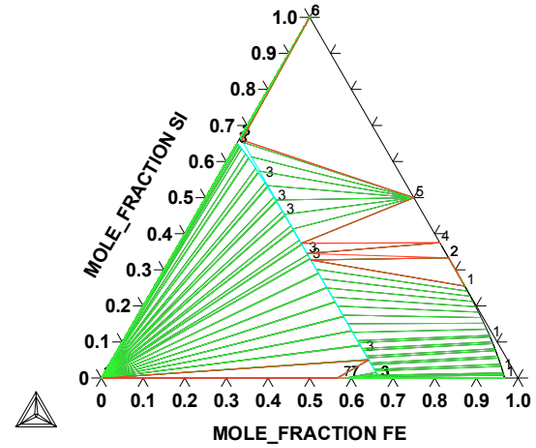

Figure 17 – Calculated phase diagram of Fe-W-Si using the commercial TCF6 database.

The crystallographic structure of FeWSi has been investigated by Gladyvaskii [50]. FeWSi has a C14 Laves phase type structure. From the binary Fe_2W to FeWSi there is a complete solid solution.

Table 8.

Phase	Pearson Symbol	Space Group	Prototype	Lattice parameters [Å]	References
FeWSi	**hP12**	**$P6_3/mmc$ (194)**	**$MgZn_2$**	**a= 4.738 c= 7.66**	**Landolt Börnstein [70] according to [65]**
FeW_2Si	**oP26**	**Pbam (55)**	**W_2FeSi**	**a=7.817 b=9.283 c=4.755**	**Landolt Börnstein[70]**

Table 8 – Crystallographic data of the compound in the ternary system Fe-W-Si.

3.5 Summary of the literature survey

The assessment of the different systems forming Laves phase in Crofer 22H are given in *Table 9 summarizing the literature survey. In this table, we reported also the associate binary systems of the ternary systems containing Laves phase.*

System	Presence of the Laves phases	Last thermodynamic assessment via Calphad method
Fe-Nb	x (C14) Fe_2Nb	[40]
Fe-W	x (C14) Fe_2W	[48]
Cr-Nb	x (C15, C14*)	[26]
Fe-Cr-Nb	x (C15, C14) $(Fe,Cr)_2Nb$	No assessment
Fe-Nb-Si	x (C14) $(Fe,Si)_2Nb$	No assessment
Fe-Si-W	x (C14) $(Fe, Si)_2W$	No assessment
Cr-Nb-Si	x (C15,C14)	[17]
Fe-Cr	None	[73]
Fe-Si	None	[74]
Nb-Si	None	[75]
Si-W	None	[76]

*Table 9 – Summary of the literature survey of the thermodynamic assessment on the ternary and binary systems containing Laves phase. *The assessment made by Pavlů et al. [26] on the Cr-Nb system take into account the presence of C14 Laves phase, nevertheless it has been experimentally shown by Aufrecht et al. [28] the non-stability of this phase. Reassessment of this system was done during the present study [29].*

The thermodynamic modeling of laves phase containing systems in Crofer 22H which has been reviewed in this literature survey showed that there is a lack of information in many binary and ternary systems. As any thermodynamic modeling of a ternary system can be well achieved with suitable associate binary systems, we first concentrated on the thermodynamic modeling of binary systems which have not been well investigated. Therefore the binary systems were investigated:

- Cr-Nb
- Fe-W

Chapter II – Methods

I. Introduction

In order to develop thermodynamic optimization of phase diagram for Laves phase containing systems in Crofer 22H [1] several methods have been used. Indeed, the optimization of phase diagrams carried out in the framework of the Calphad method relies (see part II) not only on mathematical models but also on several inputs. The primary inputs are the knowledge of the experimental phase diagram and thermodynamic properties of the considered system. It is not always possible to obtain all necessary data from experiments (i.e. enthalpy of formation of the metastable end-members), in this case the recourse to other methods to access these data is necessary. Density Functional Theory (DFT) has been widely used to access the energy of the compounds, especially the metastable ones. DFT results are restricted to 0 K but provide already an accurate approximation to compare the results at 298 K given experimentally. With the extension of the computational power it is nowadays also possible to perform phonon calculations (vibrational properties) to access the thermodynamic functions of compounds over a wide temperature range.

It is a combination of these different methods in different systems that were used in the frame of this investigation. The methods used are:

- Experimental phase diagram determination
- Calphad methods for the optimization of the phase diagram
- DFT calculations
- Phonon calculations
- Recalculation of phase diagram

In this chapter, the different methods used will be explained.

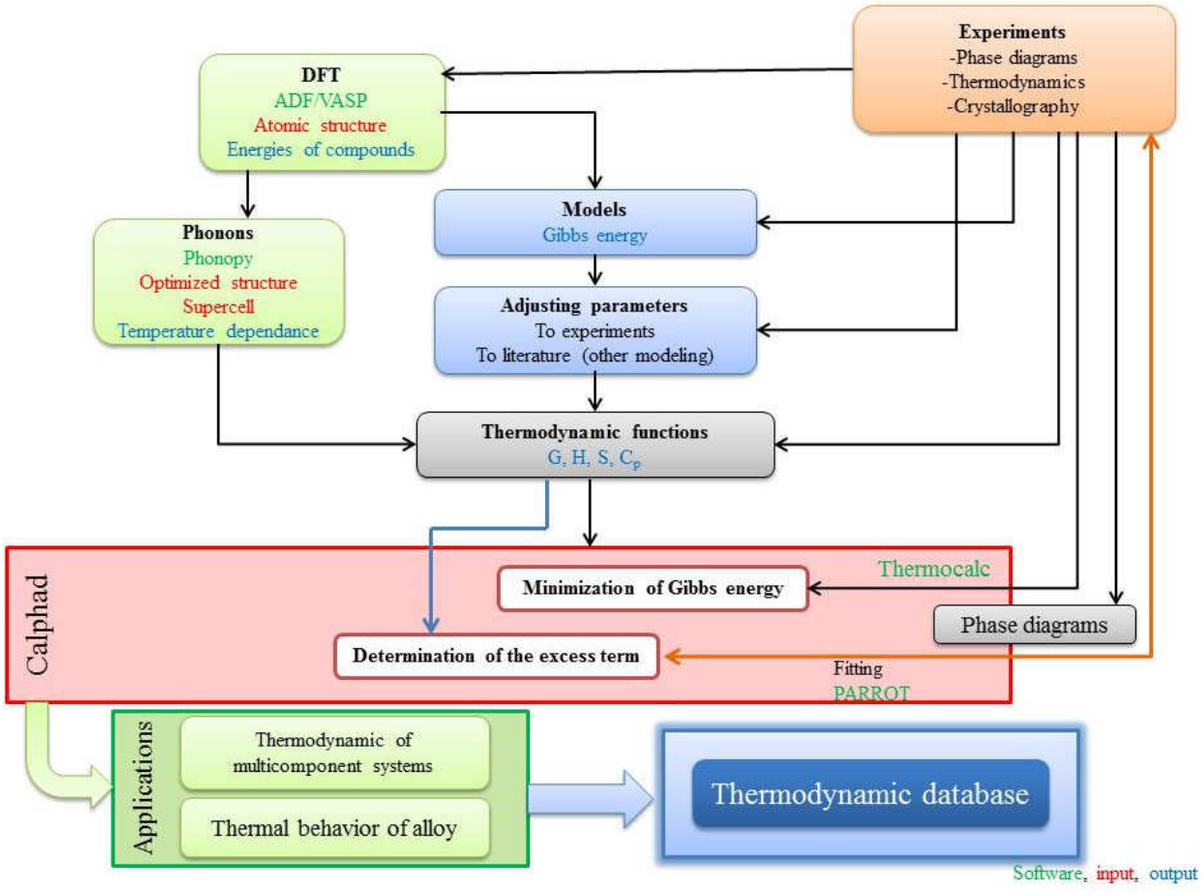

Figure 18 – Flowchart of the different methods used for the optimization of phase diagram.

II. Experimental phase diagram investigations

A phase diagram is a graphical representation of the phase transitions/transformations during heating and cooling. It is of primary importance for the understanding of phase formation. Phase diagrams are very useful for the development of alloys but also in metallurgy. In addition, experimental phase diagrams are the first information necessary for the Calculation of Phase Diagrams (Calphad) method and the optimization of the considered system as it is not possible to predict phases by this method without defining them first.

For the determination of phase diagrams, several methods can be used and several analytical tools are necessary. First, the samples should be prepared from very high purity metals and in high purity atmosphere. In the present work, we used metals with a purity of 99.99 %. The samples were then melted together in a levitation induction furnace under high purity Ar atmosphere. Different techniques are then used to determine specific properties of the phase diagram. Samples which are heat treated at different temperatures (longer when the temperature is low in order to establish thermodynamic equilibrium in samples) and then quenched, allow the construction of isothermal sections. Vertical sections and liquidus projections are constructed from data obtained by a dynamic method (differential thermal analysis – DTA). The samples are then analyzed by analytical methods like metallography or X-ray diffraction (XRD). Metallography allows the analysis of the microstructure (number of phases and invariant reactions) with techniques like scanning electron microscope (SEM). A coupling of the SEM with energy dispersive X-ray spectroscopy (EDX) allows the determination of the chemical composition of the phases. The crystallographic structures of the phases are analyzed by XRD allowing to know the symmetry of the structure and the lattice parameters.

The construction of a phase diagram can also be done by diffusion couple methods. This method can reduce the amount of samples required for phase diagram construction. This method is based on local equilibria at the phase interfaces [77].

III. Calculation of Phase diagrams (Calphad)[1]

1. Introduction

Calphad is the common acronym for CALculation of PHAse Diagrams, or rather, computer coupling of phase diagrams and thermochemistry. This is a method for the calculation of thermodynamic equilibrium of multicomponent systems using a minimization of the Gibbs energy of the system. The Gibbs energy of each possible phase in the system is defined in mathematical form by a Gibbs energy model. The derivation of the Gibbs energy models relies on experimental and ab initio input. Any other thermodynamic property can be derived over temperature, composition and/or pressure from the Gibbs energy.

In the present work, the goal of the thermodynamic modeling is to calculate phase equilibria for different specific systems forming Laves phases (binary or ternary systems) in order to build a suitable thermodynamic database for steel (i.e. Crofer 22H) applicable also for other materials with similar composition and phases) in order to study its stability under working conditi Additionally such thermodynamic databases can be used to develop new materials (i.e. manufacturing of the material and control of the formation of wanted/unwanted phases) and for other simulation tools (i.e. phase field modeling) for the description of the microstructure of the materials. Thermodynamic modeling has been carried out where no previous modeling has been done (a new modeling of an existing known system is necessary if inconsistent with the present work).

The thermodynamic modeling is called an assessment. A good assessment starts with a careful literature search and a critical review of the considered system (i.e. experimental phase diagram, thermodynamic data, previous thermodynamic models). Within different works it can happen that the same kind of data are in disagreement, in this case, a choice (assessment) should be done on which data have to be kept and which should not be considered. The thermodynamic assessment allows the calculation of the phase diagram as well as other thermodynamic properties through an optimization for the determination of the Gibbs energy of all the phases in the system.

---

[1] Chapter based on the book: Computational thermodynamics, the calphad method [78]

2. Models for the Gibbs energy

The Calphad method [78] is based on statistical thermodynamics. To model a system, it is necessary to choose a mathematical form to describe the thermodynamic function (i.e. Gibbs energy). This mathematical form should rely on physical models in order to provide reasonable extrapolations [79]. The Gibbs energy, rather than other thermodynamic functions, is used to model the phase diagram as it includes pressure and temperature as natural variables.

The Calphad method is based on the minimization of the Gibbs energy allowing the calculation of thermodynamic equilibrium. The general expression of the Gibbs energy is given below:

$$G = \sum_{\alpha} N^{\alpha} G_m^{\alpha}(T, P, x_i) \qquad \textit{Eq. 1}$$

This expression can be expanded and then is given as:

$$G_m^{\alpha} = {}^{srf}G_m^{\alpha} + {}^{cfg}G_m^{\alpha} + {}^{mgn}G_m^{\alpha} + {}^{E}G_m^{\alpha} \qquad \textit{Eq. 2}$$

The three first terms of this equation (Eq. 2) refer to an ideal Gibbs energy of mixing. The first term ${}^{srf}G_m^{\alpha}$ [illegible] ${}^{srf}G^{\alpha}$ [illegible] *Eq. 3:*

$${}^{srf}G^{\alpha} = \sum_{i} x_i \, {}^{0}G_i^{\alpha}(T) \qquad \textit{Eq. 3}$$

The second term ${}^{cfg}G_m^{\alpha}$ [illegible]

$${}^{cfg}G_m^{\alpha} = RT \sum_{i=1}^{n} x_i \ln(x_i) \qquad \textit{Eq. 4}$$

The term ${}^{mgn}G_m^{\alpha}$ [illegible]

$$G_m = \sum_{i=1}^{n} x_i \, {}^0G_i + RT \sum_{i=1}^{n} x_i \ln(x_i) \qquad \textit{Eq. 5}$$

For a real solution, the excess terms need to be taken into account to describe the thermodynamics of the system. Atoms are distributed randomly over the solution and have different energies of interaction with each other creating an excess of energy [80]. According to this, the total Gibbs energy of a substitutional regular solution model is:

$$G_m = \sum_{i=1}^{n} x_i \, {}^0G_i + RT \sum_{i=1}^{n} x_i \ln(x_i) + {}^EG_m \qquad \textit{Eq. 6}$$

And the ${}^EG_m^{\alpha}$ *Eq. 2, Eq. 6) is the excess Gibbs energy. This parameter is specifically developed in the paragraph dedicated to it (see4.b Modeling of the Gibbs energy).*

Any other thermodynamic quantities can be derived in the same way as the Gibbs energy, since they are temperature derives ofEq. 1:

Entropy

$$S = -\left(\frac{dG}{dT}\right) \qquad \textit{Eq. 7}$$

Heat capacity

$$C_P = -T\left(\frac{d^2G}{dT^2}\right) \qquad \textit{Eq. 8}$$

2.1 Unary phase

In order to be consistent with previous work, it is convenient to work on a common basis for the description of the pure elements (also called unary phase in the Calphad community). The unary database has been built for this purpose by Dinsdale [1] and used as a common basis by SGTE (Scientific Group Thermodata Europe) for the community in order to build consistent data. The molar Gibbs energy is expressed as:

$$G_m^{\alpha} = a + bT + cTlnT + \sum d_n T^n \qquad \textit{Eq. 9}$$

Eq. 9). Most of the unary phases are metastable, but with the development of computational tools, it is nowadays possible to access to them. Using phonon calculations (lattice vibration), new unary data can be obtained for the description of the pure elements in different crystallographic forms. Calculation of metastable/unstable states is encouraged for the description of the pure elements but the question may be asked if there is any physical reliability of such results. Indeed while some of the pure elements in a certain structure can be computed without showing metastability (i.e. pure Cr in σ□ □□ □□ □ □ □ σ□□□□□ □□ □□ □□ □ □□□ □□ □ □ □ □□□□ □ □□ □ □□ □□ □□ □

2.2 <u>The compound energy formalism=sublattice modeling</u>

The compound energy formalism has been developed in order to model thermodynamic properties of solution phases with homogeneity rang and different sublattices □□4□. It is a purely mathematical model which allow to give an analytical expression of the Gibbs energy for a phase with two or more sublattices□□4□. According to the compound energy formalism, the total Gibbs energy can be written as in *Eq. 2.*

σ

μ σ

Laves phase:

There are three different polytypes of Laves phases (i.e. named C15, C14 and C36 depending on their crystallographic structure) (see Literature survey).The three different polytypes are closely related but crystallize in different space groups as shown in the introduction (see page 7). The Laves phase can be written AB_2. In the present work, the addition of a third element occupies preferentially the B side (e.g. Fe-Nb-Si [20]). Commonly a two-sublattice model is used, allowing each atom to go into each sublattice. This model does not change with the type of polytype. It can be written (**$(A,B,C)(A,B,C)_2$ for a ternary system.**

The use of a two-sublattice model is well accepted to describe the three different polytypes, nevertheless it is ongoing discussion to use more complex sublattice models (e.g. three-sublattice model for the C14) as each of the different polytypes has a different set of Wyckoff positions. It has not been proved yet if more complex sublattice models would improve the thermodynamic modeling of the different Laves phases.

μ-phase:

The μ [illegible] R-3m. The atoms occupy in five different Wyckoff positions. The description of the crystal structure is given in Table 10. This would be rather expensive to calculate the energies of all different end-members using high performance computing. In order to reduce the number of end-members, some sublattices can be combined. Joubert and Dupin [85] therefore suggested a four-sublattice model. The ideal μ [illegible]

$(A,B,C)(B)_4(A,B,C)_2(A,B,C)_6$.

In the present work, we will use this model to describe the μ [illegible]

Space group R-3m (no. 166)
Pearson symbol hR39
Lattice parameters a=4.926 Å, c= 26.80 Å
Model W_6Fe_7

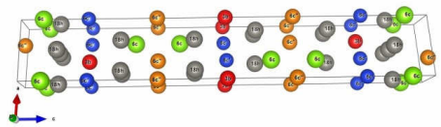

Wyckoff position	x	y	z	CN
3b (red)	0	0	½	12
6c (green)	0	0	0.055	14
6c'(blue)	0	0	0.165	16
6c'' (orange)	0	0	0.333	15
18h (grey)	0.5	0.5	0.09	12

Table 10 – Crystallographic structure information of the μ phase according to [85].

σ phase:

The σ phase crystallizes in the space group $P4_2/mnm$ and the atoms are distributed on five different Wyckoff positions (*Table 11*). It can in general be written as $A_2^{12}B_4^{15}C_8^{14}D_8^{12}E_8^{14}$ where the lower index indicates the number of atoms per position and the upper index indicates the coordination number [87]. With the point of view of crystallography a three-sublattice model $(A,B)_{10}(B)_4(A,B)_{16}$ is the most convenient [13,86]. The first sublattice is defined by $A_2^{12}D_8^{12}$, the second by B_4^{15} and the third by $C_8^{14}E_8^{14}$. By extension this model can be written $(A,B)_{10}(B,C)_4(A,B,C)_{16}$. This model was recently used for the ternary system Fe-Nb-V [88] and will be used for the description of the σ phase in the system Cr-Fe-Nb (see Chapter Thermodynamic optimization of Cr-Fe-Nb).

Space group $P4_2/mnm$ (no. 136)
Pearson symbol tP30
Lattice parameters a= 8.785 to 10.060 Å [86]
c=4.553 to 5.23 Å [86]
Model: FeCr

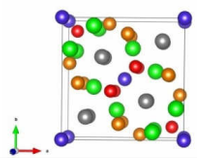

Wyckoff position	x	y	z	CN
2a (blue)	0	0	0	12
4f (red)	0.399	x	0	15
8i (orange)	0.464	0.131	0	14
8i' (green)	0.741	0.066	0	12
8j (grey)	0.183	0.183	0.251	14

Table 11 – Crystallographic description of the σ phase.

3. Input data

Any thermodynamic modeling relies on the quality of the input data. The modeling of multicomponent systems requires the knowledge of the different stable phases in the defined system. The Calphad method cannot predict the stability of a phase that has not been experimentally established and defined

- **Phase diagram data: to model the phase equilibria it is important to have a picture of the experimental phase diagram. No thermodynamic modeling of a phase diagram can be done without the knowledge of the experimental phase equilibria. Stable phases and phase boundaries (tie-lines) are the primary informations to be taken into account for modeling. Within the phase diagram information, the invariant equilibria are of primary importance for the optimization of the Gibbs energy model parameters;**
- **Thermodynamic data: Any available thermodynamic information for a phase are of primary importance for modeling of the phase diagram as they directly provide the link to the Gibbs energy of the considered phases;**
- **Crystallographic data: in Calphad modeling, the phases are defined by their crystallography (e.g. BCC, FCC□). Furthermore, this kind of information is necessary to define the sublattice model that would be used to describe the phase in the compound energy formalism (see 2.b** *The compound energy formalism).*
- **Ab initio data: Ab initio data are not experimental data, nevertheless these kind of calculations are based on the electronic structure of the elements and have shown to be a versatile method to get the energies of the compound [89,90] at 0K and is useful information in absence or in complement to experiments. They are of primary importance for the determination of the energies of hypothetical compounds (e.g. end-members of the CEF models). Previously, Gibbs energies of hypothetical compounds were estimated or optimized to fit to experimental data. More details about this method are given in the Chapter Density Functional Theory (p. 46).**

- **Phonon calculations: Ab initio calculations are restricted to 0K and do not allow to give the temperature dependence of the free energy [91]. Phonon (lattice vibrations) are calculated by displacing atoms in a supercell and computing the forces by DFT. (see Chapter Phonon calculations, p. 53).**

The combination of the different input parameters will allow the modeling of phase diagrams with more or less accuracy depending on the number of input data and their reliability (measurements errors, purity of the samples…).

For a particular system, many publications can be found in the literature, some of them can disagree. Therefore, a careful choice should be done since the modeling cannot be done by using two contradictory sets of information.

4. Optimization of parameters in the Gibbs energy models

4.1 Principle

In the previous part, the importance of the choice of data and of the models has been discussed. The modeling of phase equilibria requires the knowledge of the Gibbs energy, which is the representation of the interaction between the species. The Gibbs energy is the property that is modeled during an optimization process as it is not often possible to find its values for the considered phase in the literature. All information gathered for the phase diagram of interest (experimental phase diagram data, thermodynamic data, DFT results, etc…) is used as set of input parameters for the modeling. The modeling of the phase diagram is completed, when it has passed a complete optimization process. A successful optimization process allows a correct representation of the phase diagram (i.e. compared to the experimental knowledge of it), nevertheless, even if the representation of the phase diagram seems to be correct it is not always the case for the thermodynamic properties (i.e. enthalpy of mixing, activities). A wrong representation of a low order system can lead to troubles for the description of higher order systems.

4.2 Modeling of the Gibbs energy

The modeling of the Gibbs energy is the key pointof Calphad modeling. Its determination is done via an optimization process using for instance the Parrot module in the case of Thermo-Calc. The optimization starts from a set of chosen experimental values and of mathematical models, then the optimization will be done by fitting the calculated Gibbs energy (according to the chosen mathematical model) to the experimental data (according tothe critical review). The parrot module uses a least-square method by minimizing the weighted sum of differences between calculated and experimental values. The fitting done provides the excess Gibbs energies of the phases. In Calphad methodology, the excess Gibbs energy is expressed as a summationover the different interactions between species:

$$^{E}G_m = \sum_i \sum_{j>i} x_i x_j L_{ij} \qquad \textit{Eq. 10}$$

Where L_{ij} [illegible]

$$\Delta G^E = x_i x_j \sum_{i=0}^{n} L_i \left(x_i - x_j\right)^i \qquad \textit{Eq. 11}$$

During Calphad optimization procedure, the excess energy is often described with a linear temperature dependence $\boldsymbol{L_i = a_i + b_i T}$ [illegible]

$$L_i = h_{0i}\exp\left(-T \times \frac{s_{0i}}{h_{0i}}\right) \qquad \textit{Eq. 13}$$

Where h_{0i} [illegible] s_{0i} [illegible]

[illegible] *Eq. 12), the exponential dependence of the L parameter can be obtained by a simple fitting through an usual assessment. Nevertheless as previously explained most of the studies forget the physical importance of this parameter and a simple fitting can reveal non-physical behavior. It has been shown by Schmid-Fetzer et al. [94] that the Kaptay exponential equation [92] can also cause a miscibility gap artifact at low temperatures as shown in their paper even if this last can well reproduce the boundary conditions at high temperature. Kaptay [95] showed that in order to avoid high temperature miscibility gap by using the linear equation (Eq. 13) the excess entropy is set up to s* ≥ [illegible]

$$L_i = (h_{0i} - Ts_{0i})\exp\left(-T \times \frac{s_{0i}}{h_{0i}}\right) \qquad \textit{Eq. 14}$$

So in both cases, the L parameter (e.g. linear and exponential) can lead to artificial miscibility gap at high temperature for the linear dependence and at low temperature for the exponential one. It is probably too early to judge the last proposition of Kaptay [95] (combination of linear and exponential equation) to model the excess Gibbs energy.

In conclusion, none of these models for the Gibbs energy can lead to realistic behavior of the phase diagrams if there are only few available experimental data and they are constrained to realistic behavior. ***The optimization of the parameters in the Gibbs energy models should be done with great***

care of the experimental data respecting the phase boundaries as well as the thermodynamic data of the system and the laws of thermodynamics.

4.3 Optimization process in the present work

As explained previously, any optimization can be done with several inputs. The amount of available data will contribute to the determination of the Gibbs energy, with more or less accuracy. Nevertheless, it is difficult to judge the quality of a successful optimization of a phase diagram. The use of an optimized binary system in higher order system can reveal some deficiencies.

As any optimization can only be successfully reached with a sufficient amount of available data, in the present work, several methods to obtain the missing data of the literature have been combined.

At first, experiments have been performed to determine the phase diagrams where the available data were scarce and/or missing (e.g. see Chapter Experimental determination of Cr-Fe-Nb, p. 10).

It can be difficult to obtain experimental data in some systems due to the high melting point and slow diffusivity. In this case, computer simulation tools can be of great help for the determination of missing data. In the present work, DFT calculations were used for the determination of enthalpies of formation.

For the binary Fe-W system, DFT with phonon calculations for the determination of temperature dependence of the Gibbs energy of the end-members have been combined, which was tried for the first time in the optimization of a phase diagram.

IV. Density Functional Theory

1. Introduction

Materials properties are governed by electronic interaction between atoms, at this scale the nature of matter is governed by the law of quantum mechanics. For molecular electronic calculations, density functional theory is one of the most advanced methods and has already shown to be a versatile way of the calculation of materials properties in condensed matter and chemistry.

The main purpose of density functional theory is the solution of the time-independent Schrödinger equation for many electron interactions. For the density functional theory (DFT) calculations, the Vienna Ab initio Software Package (VASP) [96] and Amsterdam Density Functional (ADF) [97,98] have been used.

Based on quantum theory, the starting point of any calculations for density functional theory (DFT) is the many body Hamiltonian function in order to solve the Schrödinger equation.

$$\mathcal{H}\psi = E\psi \qquad \textit{Eq. 15}$$

Where ψ [illegible] $\mathcal{H}$ [illegible] *Eq. 16*

$$\begin{aligned}\hat{\mathcal{H}} &= \hat{\mathcal{H}}_e + \hat{\mathcal{H}}_n + \frac{1}{2}\sum_{i=1}^{N}\sum_{I=1}^{N_n}\frac{Z_I}{|R_I - r_i|} \\ &= \sum_{i=1}^{N} -\frac{\nabla_i^2}{2} + \frac{1}{2}\sum_{i\neq j}^{N}\frac{1}{|r_i - r_j|} + \sum_{I=1}^{N_n} -\frac{\nabla_I^2}{2M_I} + \frac{1}{2}\sum_{I\neq J}^{N_n}\frac{Z_I Z_J}{|R_I - R_J|} \qquad \textit{Eq. 16} \\ &\quad + \frac{1}{2}\sum_{i=1}^{N}\sum_{I=1}^{N_n}\frac{Z_I}{|R_I - r_i|}\end{aligned}$$

Where $\hat{\mathcal{H}}_e$ [illegible] $\hat{\mathcal{H}}_n$ [illegible] *Eq. 16).*

2. Born-Oppenheimer approximation

As it is a difficult task to solve the Schrödinger equation itself, some approximation needs to be done to calculate the electronic structure for many electrons. The positions of the nuclei and electrons should be defined. The Born-Oppenheimer approximation considers that due to the great difference of masses between the electrons and nuclei, the movement of the electrons is considered to be much faster as the nuclei's movement. Solution for a fixed position of the atomic nucleus is done. This allows to find the lowest energy configuration of the electron known as the ground state. This approximation reduces drastically the complexity of the calculation in this case the system is considered adiabatic, e.g. the lattice dynamics and the electrons are treated independently.

The two terms containing the ionic coordinates can be rewritten using an external potential $v_{ext}(\ )$ [illegible]

$$\hat{\mathcal{H}} = \sum_{i=1}^{N}\left(-\frac{\nabla_i^2}{2} + v_{ext}\right) + \frac{1}{2}\sum_{i\neq j}^{N}\frac{1}{|r_i - r_j|} \qquad \textit{Eq. 17}$$

Even considering this approximation the Schrödinger equation is rarely solvable analytically with more than two electrons. The Born-Oppenheimer approximation is valid as soon as a small ionic movement does not change the electronic wave function.

3. The Hohenberg-Kohn theorem

Basic theorems of the DFT are directly derived from the postulate of Hohenberg and Kohn [99].

Theorem 1: The external potential $v_{ext}(\vec{r})$ [illegible] $\rho(\vec{r})$ [illegible] $v_{ext}(\vec{r})$

$$E[n(r)] = T[n(r)] + v_{ext}[n(r)] + V_{ee}[n(r)] \qquad \textit{Eq. 18}$$

4. The Kohn-Sham approach

For many body electrons, it remains difficult to solve the Schrödinger equation. In 1965, Kohn and Sham [100] made the postulation that one-electron formulation can be applied to a system containing N interacting electrons by introducing a suitable local potential in addition to any external potentials $v_{ext}(r)$ [illegible]

$$[T + v_{ext}(r) + v_c(r) + v_{xc}(r)]\varphi_i = \varepsilon_i \varphi_i \qquad \textit{Eq. 19}$$

Where T is the kinetic energy. v_{xc} [illegible] E_{XC} [illegible]

$$v_{xc}(r) = \frac{\delta E_{XC}[\rho]}{\delta \rho(r)} \qquad \textit{Eq. 20}$$

The exact electronic charge density is defined by the N occupied one-electron molecular orbitals φ_i [illegible] ε_i

$$\rho = \sum_i^N |\varphi_i|^2 \qquad \textit{Eq. 21}$$

The exchange correlation energy is unknown, and is defined by the functional exchange and correlation energy $E_{XC}[\rho]$

4.1 <u>The exchange correlation energy</u>

To get accurate values from DFT calculations, the challenge is to determine correctly the exchange correlation energy E_{XC} [illegible]

$$E_{XC}^{LDA}[n(r)] = \int d^3r\, E_{XC}^{uniform}\left(n(r)\right) \qquad \textit{Eq. 22}$$

The LDA approximation doesn't take into account the real charge densities that are varying strongly. This exchange correlation function fails for the description of strongly correlated materials (i.e. materials containing delocalized s- and p- electrons as well as localized partially filled d- and f-shells). As a concrete example, iron (Fe) in bcc lattice is unstable within the LDA [78].

Since the original paper of Kohn and Sham [100], other exchange correlation potentials have been developed as the generalized gradient approximation (GGA), that is an improvement of the local density approximation by incorporating an additional term into the exchange correlation and describes better the systems with inhomogeneous electron density.

$$E_{XC}^{GGA}[n] = \int d^3r\, E_{XC}\left(n(r), |\nabla_n|\right) \qquad \textit{Eq. 23}$$

For bulk properties, it is recommended to use the GGA since it gives better agreement with experiments [89].

4.2 Basis sets

To solve the Kohn-Sham equations, there are different approaches. Here explanations for the approaches which have been used in the present work are given. Due to the lack of exact analytical solution, basis sets are used to describe the numerical expansion of the independent-particle wave-function φ_i *Eq. 19). For the calculation the efficiency of the basis set is essential.*

The plane wave basis set

The plane wave basis set is appropriate for periodic systems and often used in combination with pseudo-potentials. The periodicity of the system is introduced in the wave function. The number of plane wave depends on the energy cut-off. The plane wave basis is used in VASP [96].

Slater type basis sets

It is a function resembling to the true atomic orbitals. This function is centered at the true nucleus. This basis sets is used in ADF [97,98].

4.3 Self-consistency loop

As it remains difficult to solve numerically these equations, the solution is done via a self-consistency loop as shown below in *Figure 19*. Within each self-consistency loop, a charge density n_i is used to generate a new Kohn-Sham potential (denoted H in the *Figure 19*). Out of this self-consistency, a new charge density is calculated and the loop restarts until the self-consistency is achieved.

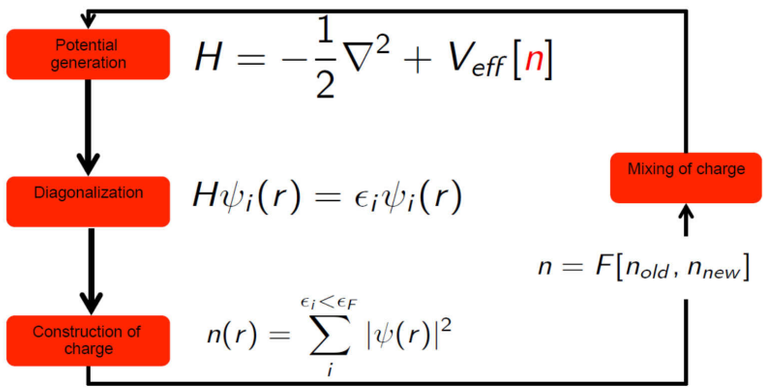

Figure 19 – Scheme of the self-consistency loop as reproduced in ref. [101].

5. Description of the electrons: all-electrons and pseudo-potential methods

5.1 All-electrons method

The wave function is defined for all electrons in the system. The potential is inversely proportional to the distance between electrons and the nucleus (~Z/r). The core states are treated as completely localized whereas the valence states are rather delocalized.

5.2 Pseudo-potential methods

The use of pseudo-potential method allows to avoid to take into account the core electron explicitly and is less demanding with respect to computational resources. It regards an atom as a perturbation of

5.3 The projector augmented wave method (PAW)

The projector augmented wave method (PAW) is an unification between all-electron and pseudo-potential methods. It has been introduced by Blöchl 103. Depending on the region of the space, the wave functions have different behavior: the wave function is fairly smooth in the bonding region, it oscillates rapidly close to the nucleus. In order to combine these two different aspects of the behavior of the wave function, Blöchl suggested to divide it into the following parts: 1) atom centered sphere, 2) envelope function outside the spheres. This method provides better access to physical properties (i.e. magnetism).

5.4 Periodicity of the system

A solid consists of many atoms (10^{24} atoms per mole), it would be rather expansive or impossible to compute a real solid. However, a solid consists of an infinite as repeated unit cell (i.e. periodic system). This property is used to reduce the number of atoms necessary to simulate a real solid, the number of atoms is now restricted to an unit cell (containing a couple of atoms) or a couple of unit cells (i.e. when studying defects in solids). The three lattice parameters and the angle between the vectors can be used to define the unit cell in the real direct space (Bravais lattice).

Using the Bloch's theorem, the density is periodic so the wave function is expressed as:

$$\Psi_k^n(r) = \mathrm{u}_k^n(r)\exp(ik.r) \qquad \textit{Eq. 24}$$

Where $\mathrm{u}_k^n(r)$ [illegible]

5.5 Brillouin zone integration

The sampling of k-points within the BZ is a crucial property for the accuracy if the convergence of the calculation. The integration over the Brillouin zone can be reduced by using the symmetry of the structure, the integration is then reduced in the irreducible Brillouin zone. There are several methods to calculate the integration over the Brillouin zone: 1) the tetrahedron method which consists of dividing up the Brillouin zone into tetrahedra, 2) sampling of special k-point as used in the Monkhorst-Pack grids for example. In the Monkhorst-Pack scheme [104], in order to choose a suitable number of k-points, it is proposed to distribute the k-points homogeneously within the first Brillouin zone.

6. DFT calculations in the present work

As previously mentioned, two different codes for the present work (i.e. ADF-BAND [97,98], VASP [96]) have been used. The differences between these two codes are summarized in the *Table 12.*

Code	Basis Set	Potential	BZ integration
ADF	**Slater type Orbital**	**Full electron**	**Quadratic tetrahedron**
VASP	**Plane-Wave**	**Pseudo**	**Monkhorst-Pack**

Table 12 – Summarized of the different approximations used in ADF [97,98] and VASP [96].

In the present work, DFT calculations have been used for the determination of the energy of several compounds in different systems. Referring to the pure elements associated to the considered compound, the enthalpies of formation were calculated. The enthalpies of formation of a compound are given by Eq. 25:

$$\Delta_f H\left(A_x B_y\right) = E_{A_x B_y} - \frac{x}{x+y} E_A - \frac{y}{x+y} E_B \qquad \textit{Eq. 25}$$

These enthalpies of formation were then used as input data for the thermodynamic modeling of the considered system according to the compound energy formalism (see Calphad, 2.2).

In addition, DFT calculations were used to calculate the forces in supercell structures for the determination of thermodynamic properties via phonon calculations.

V. Phonon calculations

1. Theory

DFT calculations are very useful at 0 K to determine energy of defined system. Nevertheless, the calculations at 0K do not include vibrational properties generated by temperatures above 0K. In order to be able to calculate properties of solids at ambient conditions (e.g. temperature), phonon calculations are a useful consideration to take into account. The influence of vibrations creating entropy becomes an important parameter to be taken into account in order to properly simulate materials properties at higher temperature.

To simulate the temperature dependence in a solid, phonon calculations based on short displacement method have been used. The atoms vibrate around their equilibrium positions (the ground state is previously reached by optimizing the geometry of compound using DFT at 0K). This is modeled by using a simple harmonic oscillator. The harmonic approximation provides a good picture to consider temperature dependence without doing too much approximation.

The energy state of a quantum harmonic oscillator is:

$$E_0 = \frac{1}{2}\hbar\omega \qquad \textit{Eq. 26}$$

With $\hbar$ [illegible] ω [illegible] *k , the energy can be computed, thus the energy is:*

$$E(k,\nu) = \hbar\omega\left[\frac{1}{2} + n(k,\nu)\right] \qquad \textit{Eq. 27}$$

Where $n(k,\nu)$ [illegible] ν [illegible] *k [105]. The number of phonons* $n(k,\nu)$ [illegible]

$$n(k,\nu) = n(\omega,T) = \left[\exp\left(\frac{\hbar\omega(k,\nu)}{k_B T}\right) - 1\right]^{-1} \qquad \textit{Eq. 28}$$

Eq. 27 and Eq. 28, the energy of a crystal within the harmonic approximation is given by, for simplification we can write $(k, \nu) = \omega$

$$E = \sum \hbar\omega \left[\frac{1}{2} + \left[\exp\left(\frac{\hbar\omega}{k_B T}\right) - 1\right]^{-1}\right] \qquad \textit{Eq. 29}$$

This is the representation of the internal energy. Deriving Eq. 29 with respect to the temperature provides the heat capacity at constant volume:

$$C_V = \left(\frac{\partial E}{\partial T}\right)_V = \sum k_B \left(\frac{\hbar\omega}{k_B T}\right)^2 \frac{\exp\left(\frac{\hbar\omega}{k_B T}\right)}{\left[\exp\left(\frac{\hbar\omega}{k_B T}\right) - 1\right]^2} \qquad \textit{Eq. 30}$$

At high temperature $k_B T \gg \hbar\omega$ C_V [illegible] k_B [illegible] C_V [illegible] $g(\omega)$ [illegible]

$$E = \int \hbar\omega g(\omega) \left[\frac{1}{2} + \left[\exp\left(\frac{\hbar\omega}{k_B T}\right) - 1\right]^{-1}\right] d\omega \qquad \textit{Eq. 31}$$

2. Thermodynamics

2.1 <u>Harmonic approximation</u>

At constant volume, different thermodynamic quantities can be calculated from the phonon density of state:

Free energy

$$F_{Ph}(T) = k_B T \int_0^{\infty} ln\left(2sinh\left(\frac{\hbar\omega}{2k_B T}\right)\right) g(\omega) d\omega \qquad \textit{Eq. 32}$$

The vibrational entropy is obtained from the harmonic phonon calculations:

$$S\,(T) = -T\left(\frac{\partial F}{\partial T}\right)_V = k_B \int \left(-ln\left[1 - \exp\left(\frac{-\hbar\omega}{k_B T}\right) + \frac{\left(\frac{\hbar\omega}{k_B T}\right)}{\exp\left(\frac{-\hbar\omega}{k_B T}\right) - 1}\right]\right) g(\omega) d\omega \qquad \textit{Eq. 33}$$

Heat capacity at constant volume can be calculated as follows:

$$C_v\,(T) = \int g(w) \frac{(\hbar w)^2}{k_B T} \frac{\exp\left(\hbar w / k_B T\right)}{\left(\exp\left(\hbar w / k_B T\right) - 1\right)^2} dw \qquad \textit{Eq. 34}$$

The harmonic approximation works under constant volume. This approximation does not take into account the pressure, whereas experiments are at least carried out under atmospheric pressure. The harmonic approximation does not allow to take into account the thermal expansion, the phonon-phonon interactions as well as the thermal conductivity.

The results obtained can be represented by a simple mathematical model. Phonons provide in domination the heat capacity, and the different models are given for the heat capacity. In the present contribution we give a short overview of the Einstein model, the Debye model and the polynomial function.

2.2 <u>Einstein model</u>

The Einstein model makes the postulation that all modes in the density of state have the same frequency ω_E [illegible]

$$\omega_i = \omega_E \qquad \textit{Eq. 35}$$

Therefore the heat capacity is:

$$C_V = \left(\frac{\partial E}{\partial T}\right)_V = \sum k_B \left(\frac{\hbar\omega_E}{k_B T}\right)^2 \frac{\exp\left(\frac{\hbar\omega_E}{k_B T}\right)}{\left[\exp\left(\frac{\hbar\omega_E}{k_B T}\right) - 1\right]^2} \qquad \textit{Eq. 36}$$

At high temperatures, this rule follows also the Dulong-Petit rule, nevertheless at low temperatures, this fails and is not equal to zero as it should be.

2.3 Debye model

As the Einstein model failed to represent correctly the behavior of the heat capacity at low temperatures, the Debye model allows a better representation. In the Debye model, each mode has its own frequency. The heat capacity is given by:

$$C_v = 9Nk_B \left(\frac{T}{T_D}\right) \int_0^x \frac{e^x x^4}{(e^x - 1)} dx \qquad \textit{Eq. 37}$$

Where T_D is the Debye temperature.

2.4 Polynomial function

In thermodynamic databases the Gibbs energy functions are described with a polynomial function. The energy of a compound is described relative to the surface element reference (SER) (i.e. surface of the pure elements in their respective stable phase).

The Gibbs energy of a compound is described as:

$$G_m^\alpha = a + bT + cTlnT + D_2T^2 + D_3T^3 + D_{-1}T^{-1} \qquad \textit{Eq. 38}$$

This power series can be extended but the results are not improved much. Based on Eq. 38 the heat capacity is given by:

$$C_P = -T\left(\frac{d^2G}{dT^2}\right) = -C - 2D_2T - 6D_3T^2 - 2D_{-1}T^{-2} \qquad \textit{Eq. 39}$$

This polynomial function fails to describe the thermodynamic function below room temperature.

3. Quasi-harmonic approximation

The harmonic approximation is done at constant volume and cannot reproduce all the physical phenoma of a solid:

- Thermal properties (thermal expansion)
- Phase transitions
- Transport properties

All these properties are referring to the anharmonicity of the crystal. The anharmonicity of the system is the interaction between phonons with other phonons. In a simple approach, the anharmonicity can be modeled using the quasi-harmonic approximation [82] (i.e. phonon calculation are computed over different volumes) as it is small enough that the quasi-harmonic approximation can represent it in many cases (with some exception) [106]. Making the assumption that the anharmonicity is only restricted to the thermal expansion [105], the QHA approximation can be used.

The vibrational Helmholtz energy F in the QHA approximation can then be written:

$$F_0(V,T) = U_0(V) + \frac{1}{2}\hbar\omega_j(k,V) + k_B T \sum ln\left(1 - exp\left[-\frac{\hbar\omega_j(k,V)}{k_B T}\right]\right) \qquad \textit{Eq. 40}$$

Where the first term is the internal contribution, the second the zero point energy and the third the vibrational contribution.

In the quasi-harmonic approximation, the heat capacity at constant pressure (C_P) is obtained from:

$$C_P = C_V + VT\alpha^2 B \qquad \textit{Eq. 41}$$

Where α [illegible]

$$S\,(V,T) = S_{har} + VT\alpha^2 B \qquad \textit{Eq. 42}$$

4. Results

Several parameters influence the results of the thermodynamic properties obtained from the phonon calculation:

- Optimization of the structure: any computation of the phonon relies first on the very accurate optimization of the structure. Any structure which is not well relaxed is not in its local ground state (i.e. not in equilibrium) and phonon calculations will lead to the appearance of imaginary frequencies and show that the structure is mechanically unstable. Any parameters influencing a correct geometry optimization (i.e. k-points, energy cut-off) influence the computation of phonons.
- Size of the supercell: the size of the supercell should not be too small to obtain accurate phonon calculations. Nevertheless this one should stay as small as possible for computational reason.

In the present work, phonon calculations have been used to describe the thermodynamic functions of different compounds (stable and hypothetical). The results were then used as input for the thermodynamic modeling as described by the Calphad method.

Chapter III - Pure elements and binary boundary systems

With the development of computational power and simulation tools (i.e. DFT, phonon) it has become clear that these methods will be further used and developed [106] to understand the materials behavior. In the present work, simulation tools as DFT, phonon and Calphad modeling are used to understand the driving forces controlling the formation of the different phases present in Crofer 22H.

I. Pure elements

The thermodynamic modeling of unary phases is important as they are the basis as reference state for other intermetallic phases. In the present work, we consider the pure elements forming the Laves phase (Fe,Cr,Si)(Nb,W) in Crofer 22H in their stable form (e.g. bcc and diamond). Calculations of their total energies in their stable form (and magnetic state) are necessary for further calculations of enthalpy of formation for example, which are then used as input parameters for thermodynamic modeling. In addition, phonon calculations have been done in order to check the reliability of the results and to test some different parameters for further calculation in more complex structures.

1. Energy of formation

The energy of formation of a compound refers to the pure elements in their stable form according to *Eq. 43:*

$$\Delta_f H(A_x B_y) = E_{A_x B_y} - \frac{x}{x+y} E_A - \frac{y}{x+y} E_B \qquad \textit{Eq. 43}$$

The calculation of the enthalpy of formation of several compounds in different systems were performed in the present work, their results will be developed in a later chapter and discussed. Here results of the pure elements used as reference state are given. The total energies of the ground state of the pure elements in their stable form were calculated by DFT, and the results were compared with available data from literature. The energy of formation of the pure elements can only be compared with literature data, where the same codes and same basis function have been used as in the present work. The data presented here have been generated using VASP [96], with the PAW potential [103] within the GGA-PBE approximation. Other specific parameters as the k-points and the energy cut-off

Table 13-17 . The results were obtained by following three different steps of calculation in order to get accurate values of the total energy. For all calculations, the ground state energies were reached in three steps: 1) the volume and the atomic positions were relaxed; 2) the stresses and forces were relaxed: 3) the tetrahedron method with Blöchl correction was used for accurate calculations of the ground state. For all calculations, an accuracy 10^{-6} was set up in the self-consistency loop. Results are given in Table 13-17 for each pure element.

Species	Structure	Magnetic state	k-points	Energy cutoff (eV)	E_f (kJ.mol^{-1}.atom^{-1})	a(□)	V(□□)	Ref.
Cr	bcc	AFM	11x11x11	400	-915.229	2.8359	22.81	Present work
		-	-	-	-913.284	2.847	23.08	[107]
		AFM	12x12x12	-	-913.909	2.8375	22.846	[108]
		AFM	16x16x16	400	-931.08			[109]

Table 13 – Energy of pure Cr in the BCC structure compared with literature.

Species	Structure	Magnetic state	k-points	Energy cutoff (eV)	E_f (kJ.mol^{-1}.atom^{-1})	a(□)	V(□□)	Ref.
Fe	bcc	FM	11x11x11	400	-800.306	2.8304	22.79	Present work
					-798.397	2.822	22.5	[107]
		FM		500	-792.603	2.832	22.7	[88]
		FM		400	-792.614	2.832	22.7	[38]
		FM	12x12x12		-788.67	2.8256	22.56	[108]

Table 14 – Energy of pure Fe in BCC with the different parameters used to carry out the calculations. The results are compared with available literature data.

Table 15 – Calculated energies of Nb as well with the lattice parameters.

Species	*Structure*	*Magnetic state*	*k-points*	*Energy cutoff (eV)*	*E_f (kJ.mol^{-1}.atom^{-1})*	*a(□)*	*V(□□)*	*Ref.*
Si	*diamond*	*NM*	*11x11x11*	*400*	*-523.40*	*5.4683*	*163.51*	*Present work*
					-524.06	*5.468*		*[110]*

Table 16 – Energies and lattice parameters calculated in diamond structure compared with literature.

Species	*Structure*	*Magnetic state*	*k-points*	*Energy cutoff (eV)*	*E_f (kJ.mol^{-1}.atom^{-1})*	*a(□)*	*V(□□)*	*Ref.*
W	*bcc*	*NM*	*11x11x11*	*400*	*-1255.496*	*3.173*	*31.915*	*Present work*
					-1232.899	*3.19*	*32.46*	*[107]*

Table 17 – Energies of pure W calculated by DFT after optimization of the structure.

For all the pure elements, there is a good agreementof the present results with literature data. The small difference found is due to different approximations used for the calculations (i.e. k-points, pseudo-potential)□ and it is within the error range as any other experimental data. For calculations of the energy of formation of the different compounds, calculation of the total energy of the pure elements of the present work as reference state has been used. For compounds where energies of

2. Phonon calculations of the pure elements

To simulate the temperature dependence in the solid, we used phonon calculations based on short displacement methods. In practice, we used the supercell methods with finite displacement also called the direct method as implemented in the phonopy package [111]. The supercells were built from the optimized structures from DFT as previously described and the atoms are displaced from their equilibrium position by 0.01 Å. The accuracy of the phonon calculations can be influenced by different parameters. Of course the primary parameter to get correct phonon calculations is a good minimization of the ground state (e.g. suitable k-points, low residual forces). The other parameter that can influence the accuracy of the results is the size of the supercell.

Harmonic approximation was used to compute the thermodynamic properties at constant volume. The force constants of the different supercells were calculated with VASP, they were then used in phonopy [111] to calculate the phonon frequency and to derive their relative thermodynamic properties. The phonon contribution to the Helmholtz free energy is given by:

$$F_{phonon}(T) = \frac{1}{2}\sum_{q,\upsilon} \hbar\omega_{k,\upsilon} + k_B T \sum_{q,\upsilon} ln\left[1 - exp\left(-\frac{\hbar\omega_{k,\upsilon}}{k_B T}\right)\right] \qquad Eq.\ 44$$

Where k and $\omega_{q,\upsilon}$ [illegible]

[illegible] *Eq. 41.* [illegible]

2.1 Iron, Fe

The structure of Fe was carefully optimized taking into account the ferromagnetism. The relaxed structure (energy and lattice parameters are given in *Table 14) was then used to build a 2x2x2 supercell. The force on the displaced atoms are then computed with VASP [96]. The different forces calculated for each structure are then collected and used to calculate the phonon frequencies, which in turn are used to calculate the temperature dependent thermodynamic properties. The calculated thermodynamic data in the harmonic approximations are given in Figure 20.*

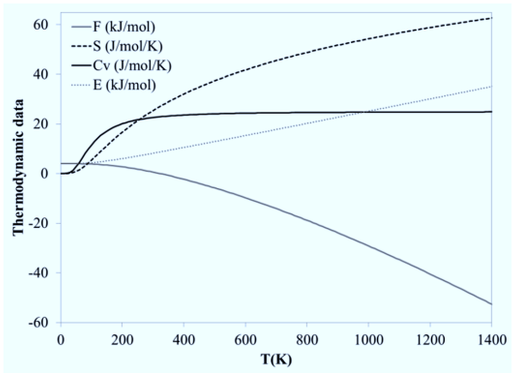

Figure 20 – Thermodynamic properties of Fe obtained the calculated phonon harmonic calculations.

In the quasi-harmonic approximation (QHA) for Fe, nine different volumes with a maximum volume change of about 12 % were used. The energy dependency of the volume at 0 K is shown in Figure 21.

The minimum of the Helmholtz free energy vs temperature (*Figure 22*) is obtained by fitting the volume-energy data to the Vinet equation of state [112] (*Eq. 45*).

$$G(T,P) = min_V\left[U(V) + F_{ph}(V,T) + PV\right] \qquad \textit{Eq. 45}$$

Thermodynamic functions of Fe are then obtained by derivation.

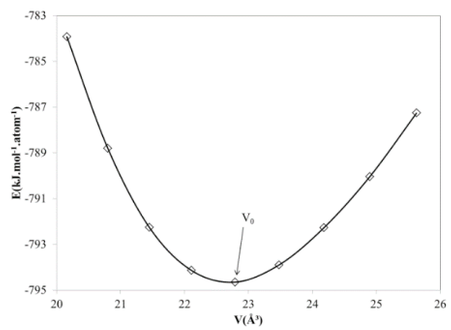

Figure 21 – Energy dependency volume for pure Fe in BCC structure given at 0K.

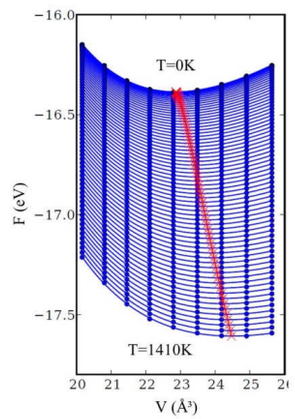

Figure 22 – Helmholtz free energy of Fe as function of volume and temperature for determination of the minimum energy (red line).

For metals, the electronic contribution influences the thermodynamic properties. Depending on the metals, their influence can be negligible or not. The higher the electron valency is, the higher the

influence of electron contribution is. Hence, for iron this influence is not negligible and its value was taken from [82] (see *Fig. 8* of the original paper) and added to the heat capacity and entropy curves (*Figure 23*a).

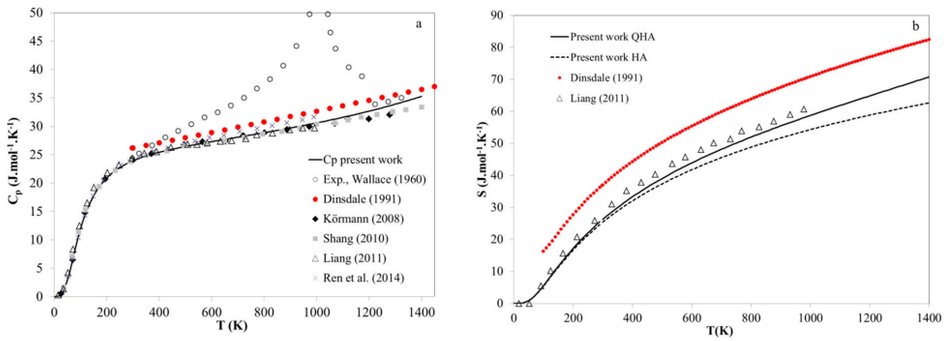

Figure 23 – a) Heat capacity of Fe compared with literature data from experiments [113] *and phonon calculated heat capacity* [114–117]. *The red point from Dinsdale* [81] *are the commonly used data in Calphad modeling for the description of pure Fe (these data don't take into account the magnetism). b) Entropy of Fe from QHA and HA phonon calculation compared with phonon QHA calculations of Liang* [116] *and the Dinsdale polynomial* [81].

The experimental results of the heat capacity of Fe cannot be fully reproduced by phonon calculations in QHA approximation due to the magnetic excitation [115]. The magnetic contribution was the subject of several studies in the literature [114,115], and show the difficulty to model Fe. In Calphad type modeling, the magnetism of iron is treated in a separate function. This leads to the difference between the phonon and the Dinsdale polynomial [81] (for example in the entropy curve - *Figure 23b*). The magnetic contribution to the enthalpy of Fe is about 8 kJ.mol^{-1} at 300 K (*Figure 24*), this can result in a non-stability of intermetallic phases (i.e. Laves-Fe_2W and μ-Fe_7W_6 phases in Fe-W system as seen in Chapter IV) whereas experiment and DFT calculations suggest the opposite.

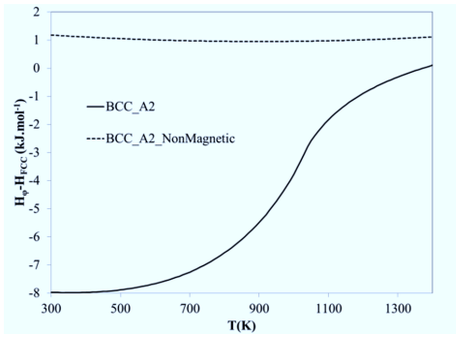

Figure 24 – Enthalpy of Fe calculated from the Dinsdale polynomial [81] and used in the Calphad modeling for the reference state of BCC Fe. The calculation of the enthalpy refers to pure Fe-FCC.

The treatments of the magnetism as an independent function in the description of the pure element [81] have to be taken into account when preforming an thermodynamic optimization of a phase diagram. In the systems where Fe is present, the enthalpies of formation of the compound should be written by taking into account the 8 kJ.mol^{-1} of difference due to the magnetism. In many of the systems studied in the present work Fe is present so the magnetic contribution has to be treated carefully.

2.2 Tungsten, W

In the same way as for Fe, phonon calculations in harmonic and quasi-harmonic approximations have been done for W. Thermodynamic properties were then obtained from them. W does not show magnetic order and its thermodynamic properties are not influenced by it. The volume dependency to the free Gibbs energy is given in *Figure 25 and the heat capacity derived from it is given in Figure 26. The electronic contribution to the heat capacity is rather small compared to that of Fe (see Fig. 8 in [82]). Nevertheless, its contribution was added to our calculated heat capacity (given in Figure 26).*

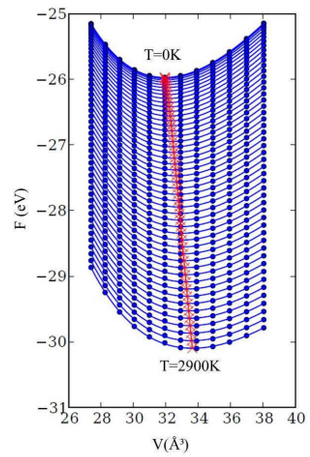

Figure 25 – Helmholtz free energy of W in QHA approximation as a function of the unit cell and temperature. The minimum values of the fitted equation of state (Vinet equation) are given by the red cross.

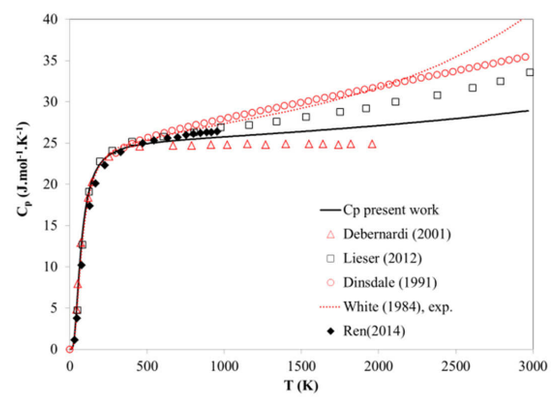

Figure 26 – Heat capacity of W calculated in the QHA approach compared with experimental data [118] *(round dotted red point), SGTE pure element from the Dinsdale polynomial* [81] *(red empty circles) and other phonon calculations in harmonic approximation* [119] *(red empty triangles) and QHA* [117,120] *(empty squares and black diamond).*

II. Binary boundary systems

1. Calculation in binary systems: Fe-Nb, Fe-Si, Nb-Si, Cr-Nb

Ab initio calculations have been performed using ADF-BAND [98] in this part of the present work in several binary systems where a lot of literature data are available to test some different parameters (i.e. SCF convergence, magnetism, functionals…) and check for consistency with experiments or/and other ab initio calculations. ADF [98] is using an all electron method for the description of the elements. This method could be seen as very accurate, nevertheless it is computationally very expensive and requires a lot of computational time, whereas it has been shown that a pseudo-potential (or PAW) method was also accurate.

The calculations have been done for stable compounds on the different considered systems. For the exchange-correlation energy, we used the generalized gradient approximation (GGA) [103] of Perdew, Burke and Ernzerhof (PBE) [121]. The magnetism was taken into account for the compounds containing Fe and Cr. The scalar relativistic ZORA effect was implemented in the calculations. The energy of formations were calculated at 0K using an energy convergence of 10^{-6}eV and a TZP basis set with small core was used.

Calculations using ADF-BAND [98] have been done in the Fe-Si, Fe-Nb, Nb-Si and Cr-Nb systems. The calculated enthalpies of formations are shown in *Figure 27-30 and compared with available literature data. The DFT calculations from the literature have been done by using VASP which is a pseudo-potential method whereas ADF-BAND is an all-electron method.*

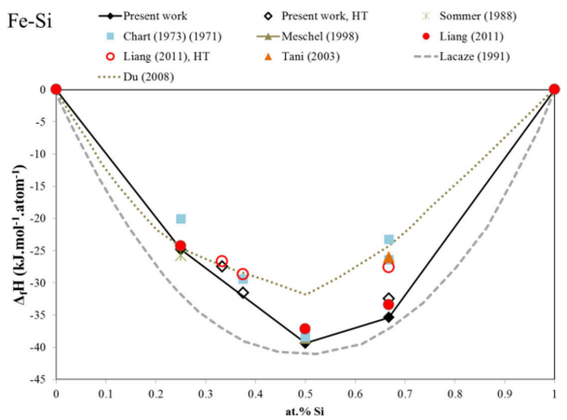

Figure 27 - Enthalpy of formation of Fe-Si of the present work (black diamond) compared with experiments [122–125] *(blue square, brown diamond, star) DFT* [116,126] *(red empty square, orange triangle) and Calphad* [127,128] *(dotted line, point line). HT=High Temperature.*

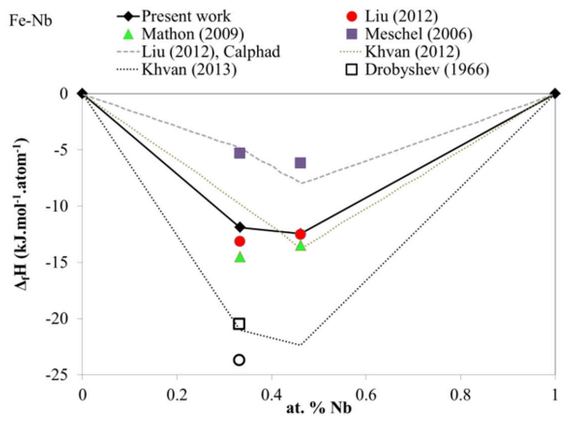

Figure 28 - Enthalpy of formation of Fe-Nb of the present work compared with experiments [36,37] (violet square, empty square), DFT [38] (red circle) and Calphad [38–40] (dotted, dashed, point lines).

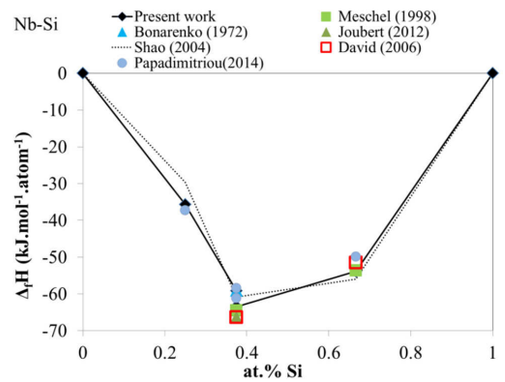

Figure 29 - Enthalpy of formation of Nb-Si compared with literature from experiments [123,129] *(blue triangle, green square), DFT* [130,131] *(green triangle, blue circle) and Calphad* [17,132] *(point line, red square).*

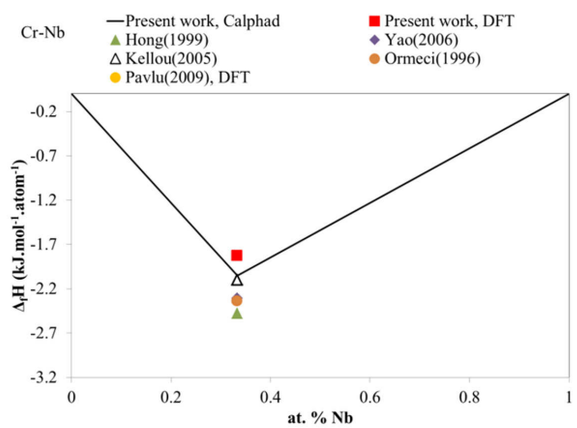

Figure 30 - Enthalpy of formation of Cr-Nb from DFT-ADF (red square) and Calphad modeling (balck line), the present results (given as present work) are published in Ref. [29] *compared with DFT calculations* [26,133–136] *(symbols).*

For all binary systems, we noticed a good agreement of our calculated enthalpies of formation with the available literature data. This shows a good reliability of the results and the two different

2. Cr-Nb

The results of the enthalpies of formation in the Cr-Nb (i.e. end-members of the C15 laves phase) have been used as input data for the thermodynamic modeling of this system and compared with the available literature (*Table 18*).

End-members	Δ			
	-1.83 (FM) **-1.72 (NM)**	**6.96** **6.93**	**Present work**
	-3.31 (FM)	**6.93**	**[26]**
	-2.48 (FM)	**6.82**	**[133]**
	-2.31 (FM)	**6.93**	**[135]**
	-2.1 (FM)	**6.94**	**[134]**
	-2.34 (FM)	**-**	**[136]**
Nb_2:Cr	**75.38 (FM)** **75.39 (NM)**	**7.51** **7.50**	**Present work**
	75.33 (FM)	**7.50**	**[26]**
Cr_2:Cr	**30.56 (FM)** **33.55 (NM)**	**6.64** **6.66**	**Present work**
	27.29 (FM)	**6.58**	**[26]**
	26.4 (FM)	**-**	**[137]**
Nb_2:Nb (NM)	**15.33 (NM)**	**7.74**	**Present work**
	16.2 (NM)	**7.69**	**[26]**
	16.2 (NM)	**-**	**[137]**

Table 18 – Enthalpy of formation of the optimized end-members from DFT calculation compared with literature data (also DFT calculations).

As mentioned in the literature review (Chapter I- Cr-Nb), the re-optimization of this system was necessary as it was shown by Aufrecht et al. [28] that the high temperature Laves phase (C14) was

Figure 31. It is in good agreement with experimental data. A full literature survey and the methods of calculation are given in Schmetterer et al. [29].

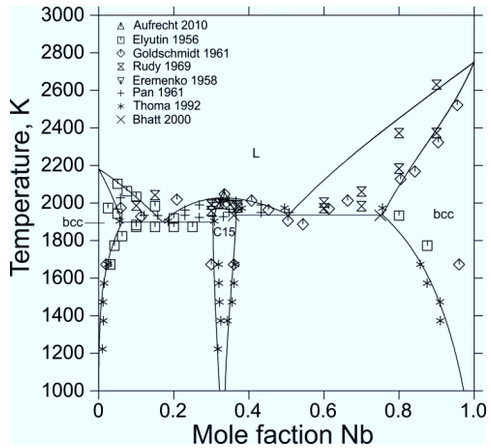

Figure 31 – Optimized phase diagram as presented by Schmetterer et al. [29] using DFT calculations of the present work and compared with available literature data [28,30,51,138–140].

New experimental data for the invariant reactions have been published by Stein et al. [18] after the publication of our assessment of the Cr-Nb system [29]. Comparison of the temperature of the invariant reaction of the calculatedand experimental data is given in Table 19.

Invariant reaction	**Calculated values [29] T(K), x(Nb)**	**Experimental values**	**Experimental values [18] T(K), x(Nb)**
E_1: L→			
C: L→			
E_2: L→			

Table 19 – Comparison of the temperature of the invariant reactions using the calculated phase diagram and the experimental values.

3. DFT calculations in other systems

Some problems have been encountered by using the ADF code [98]. Indeed already by its method, i.e. all electrons, the calculations are computationally expensive. In addition, this software had several bugs that were reported to the software developer. One of the major bugs with this program was to use a specific space group (i.e. space group 166, R-3m). For this space group one of the symmetry of the crystal structure was not correctly implemented. Three atoms of the same Wyckoff position were occupying the same position whereas they should have been shifted by translation using the correct symmetry. Nevertheless, compounds with this space group are present in several of the studied systems.

The use of another software for the computation of the energy of the structures has been considered necessary due to the several bugs as well as the time required for the computation of a structure. The commercial software VASP [96] was considered as a suitable choice for the present work. Using the VASP software, calculations of the enthalpies of formation (and phonon) have been done for end-members in the Fe-W binary system and Fe-Cr-Ni and Fe-Nb-Si ternary systems. The calculations will be developed for each system in their respective part with the details used to carry out the calculations.

Chapter IV – Modeling of Fe-W phase diagram using first-principles and phonons calculations

A part of this chapter is based on a paper accepted for publication in Calphad [141].

Introduction

Thermodynamic calculations using the Calphad method (Calculation of phase diagram) for systems with many components as found in real materials, e.g. steels and Ni-base super alloys, have become firmly established tools in industry and research. Such calculations rely on thermodynamic databases composed from many individual called phase diagram optimizations (thermodynamic assessments), predominantly done for 2-, 3- and 4-component systems and extrapolations for higher systems. While the benefits of modeling are obvious, i.e. for example savings on resource intensive experiments and tests, the accuracy of the calculations relies on the underlying thermodynamic descriptions of binary and ternary systems.

A conventional optimization is based on a set of experimental data (phase diagram data and thermodynamics) and the parameters for the chosen model are obtained in a sophisticated kind of constrained data least-square fit (the optimization). This means that the number of parameters that can be used depends on the amount of available input data – a limited amount of data only allows for the use of few model parameters. The limitations of this approach are evident from many optimized datasets where linear functions or even constant values are being used in the functions describing the Gibbs energy. This effectively means that only the enthalpy and entropy of formations can be used for the thermodynamic modeling. At high temperatures this can lead to the appearance of inverted miscibility gaps in the liquid phase as well as other problems.

In the present work, a combination of density functional theory (DFT) and phonon calculations as well as Calphad method was used to establish a new thermodynamic dataset for the binary Fe-W system. This system is relevant for steel research, in particular for the further development of Laves phase reinforced ferritic steels [1,142]. Although this system is not particularly complex it poses experimental difficulties due to the high liquidus temperatures (especially on the W-rich side), slow

λ μ

I. Literature survey

A summary of the literature survey of the Fe-W binary system was given in the literature survey (Fe-W, p 16). Furthermore, a full literature survey was written for the publication.

The Fe-W binary system contains two intermetallic phases, the Laves μ

Table 20). The phase diagram was recently reinvestigated experimentally by Antoni et al. [47] due to several controversies. The last assessment of this system was given by Gustafson [48] and is shown in Figure 6 and compared to experimental data. The invariant reactions of the system are given in Table 20 with their respective temperatures and compositions.

μ		
μ		
μ		

*Table 20 – List of the invariant reactions in Fe-W phase equilibria given in the literature and considered for the thermodynamic modeling. *The phase boundary on the W-rich side is not well defined, Ichise [143] gave a phase boundary at 97.4 %. We used this data for the peritectic temperature given by Sinha et al. [44].*

II. Modeling

In the present work, a multiscale modeling approach was chosen in order to describe the thermodynamic properties of the Fe-W system. This included the use of DFT calculations, phonon calculations and Calphad. For the latter, the PARROT module of the software Thermo-Calc [144] was employed which utilizes the sublattice or substitutional solution model for solution phases. The computer simulations preceding the Calphad type assessment therefore had to be based on the same models as imposed by Thermo-Calc. Furthermore, in order to be compatible with existing databases, the same models as in the TCFE database were used:

- a two-sublattice model **$(Fe,W)_2(Fe,W)_1$ for the Laves phase**
- a four-sublattice model **$(Fe,W)_1(W)_4(Fe,W)_2(Fe,W)_6$ for the -phase**
- substitutional solution model (one sublattice model) for the BCC, FCC and liquid phases

Main components on the sublattices are shown in bold. More details on the use of these sublattice models will be described in section II. 3 (p. 80).

1. Density Functional Theory (DFT)

DFT calculations were carried out using the VASP software package [96] using the GGA-PBE approximation for the exchange energy and projector augmented waves (PAW) [145] as basis set. For

Table 23, Table 24 and Table 25. For all calculations, the ground state energies were reached in three steps: 1) the volume and the ion positions were relaxed 2) the stresses and forces were relaxed 3) the tetrahedron smearing method with Blöchl correction [146] was used for accurate calculations of the ground state. For all calculations, an accuracy of 10^{-6} eV was set up in the self-consistency loop and an energy cutoff of 400 eV was used. The magnetism of the compounds was taken into account due to the presence of Fe. For each Fe containing compound, calculations were made in the ferro- and non-magnetic states in order to determine the more stable one. For the Fe-free end-members, a non-magnetic state was used.

The energies of formations of the end-members were calculated according to Eq. 46.

$$\Delta_f H(Fe_xW_y) = E_{Fe_xW_y} - \left[\frac{x}{x+y}E_{Fe} + \frac{y}{x+y}E_W\right] \qquad \textit{Eq. 46}$$

$E_{Fe_xW_y}$ [illegible] Fe_xW_y [illegible] *Table 23). The results of the calculated enthalpies of formation are given in Table 24 and Table 25 for each end-member of the Laves and the μ-phase.*

2. Density Functional Theory Phonon Calculations

In order to determine the temperature dependence of the Gibbs energy functions, phonon calculations were done for the end-members as well as for the pure elements. The phonon calculations allow to take into account the lattice vibrations in the crystal and to get thermodynamic properties over a range of temperature, whereas DFT calculations are limited to 0 K. These allow to get the temperature dependence of the total Gibbs energy and to be used for the Calphad assessment. Our calculations were carried out using the software package Phonopy [111], which is based on the supercell method with finite displacements [147] (also called the direct or Parlinski-Li-Kawazoe method). The supercell is built from the structures optimized as previously described, and displacements of 0.01Å were used

$$F_{phonon}(T) = \frac{1}{2}\sum_{q,\upsilon} \hbar\omega_{q,\upsilon} + k_B T \sum_{q,\upsilon} ln\left[1 - exp\left(-\frac{\hbar\omega_{q,\upsilon}}{k_B T}\right)\right] \qquad \textit{Eq. 47}$$

Where q and ν [illegible]

ω [illegible]

$$C_V = \sum k_B \left(\frac{\hbar\omega}{k_B T}\right)^2 \frac{\exp\left(\frac{\hbar\omega}{k_B T}\right)}{\left[\exp\left(\frac{\hbar\omega}{k_B T}\right) - 1\right]^2} \qquad \textit{Eq. 48}$$

VASP [145] was used to calculate the force constants of the different supercells with displaced atoms. The force constants were then used in phonopy [111] to calculate the phonon frequencies and their related thermodynamic functions (Eq. 47 and Eq. 48). Such calculations were carried out for each end-member of the Laves and μ-phases. Different sizes were used for the supercells of the Laves and the μ-phases, 2x2x2 and 2x2x1 respectively. As the c lattice parameter of the μ-phase is large compared to the a parameter, the size of the cell was not increased in this direction. Furthermore, the size of the supercell was kept as small as possible in order to keep the computational effort and time reasonable. Computational details for the various compounds are given with the results in Table 26 and Table 27.

In metallurgy, phase diagrams are usually shown for constant pressure (i.e. at 1 atmosphere) or the influence of the pressure is considered negligible. Therefore, the temperature dependence of the materials properties is not only governed by the harmonic approximation but also by thermal expansion. The corresponding thermodynamic properties should therefore be obtained for constant pressure instead of constant volume. Therefore, quasi-harmonic phonon calculations were carried out for the stable end-members λ [illegible]

Eq. 49).

$$G(T,P) = min_V\left[U(V) + F_{ph}(V,T) + PV\right] \qquad \textit{Eq. 49}$$

Where V and P are volume and pressure, respectively. U(V) expresses the total energy of the electronic structure at constant volume [112]. The Gibbs energy curve in QHA approximation for Fe_2W is given as an example in Figure 34. The heat capacity at constant pressure is then calculated from Eq. 50:

$$C_P(V,T) = C_V + VB\alpha^2T \qquad \textit{Eq. 50}$$

Where B and α [illegible] *Eq. 51:*

$$S_{QHA} = S_{ph} + VB\alpha^2T \qquad \textit{Eq. 51}$$

The volumes for the calculation of the Gibbs energy in the QHA approach were carefully chosen around the equilibrium. Some volumes too far from the equilibrium volume (□8%) were discarded as their phonon dispersion curves showed negative frequencies. The number of computed volumes as well as the minimum, equilibrated and maximum volumes are given in Table 21 for compounds where QHA approximation has been computed.

Compounds - Structure	*Number of computed volumes*	*Min V, Eq. Vol., Max Vol.(□)*
Fe_2W – C14 Laves phase	*7*	*133.12, 145.86, 159.39*
Fe_7W_6 – μ □		□ □ □ □
□□ □ □μ □		□ □ □ □ □

Table 21 – Number of volumes and volumes of the crystal structure used to compute the quasi-harmonic calculations.

3. Calphad modeling

The Fe-W phase diagram in this work was modeled according to the Calphad method. In this method the thermodynamic equilibria are calculated from parameterized expressions of the Gibbs energies of the various phases as a function of composition, temperature (and pressure). In the present work, the Thermo-Calc software [144] was used throughout. Basic information on this method can be found in [78] as well as in the previous part Chapter II, Part III, p. 34.

This method consists on modeling the total Gibbs energy of a system as explained in previous part (i.e. Chapter II).

In the CEF, each phase with an appreciable homogeneity range can be divided into a number of sublattices on which several (but not necessarily all) constituting atoms can be placed. For crystalline phases with sufficiently simple crystal structures, the sublattices can be taken or derived from the crystallographic lattices of the crystal structure. Each arrangement of one atom on each sublattice (= "constituent array") represents a limiting composition of the particular phase and is called an end-member. All end-members have their own energies of formation, most of which are hypothetical and inaccessible by experiments. In the present work, they were obtained from DFT calculations.

In Thermo-Calc [144], the interaction parameter $L_{i,j}$ [illegible]

$$L_{i,j}^{\alpha} = {}^{0}L_{i,j}^{\alpha} + {}^{1}L_{i,j}^{\alpha}(x_i - x_j) + {}^{2}L_{i,j}^{\alpha}(x_i - x_j)^2 + \cdots + {}^{n}L_{i,j}^{\alpha}(x_i - x_j)^n \qquad \textit{Eq. 52}$$

The $L_{i,j}{}^{n}$ [illegible] Eq. 53). Typically, parameters up to second order are used.

$${}^{k}L_{i,j}^{\alpha} = A + BT \qquad \textit{Eq. 53}$$

In a Calphad assessment, the end-member energies (G-terms) and interaction parameters (L-terms) are derived from available experimental and thermodynamic data. Results from atomistic simulations can either be used directly as functions of temperature or in the same way as experimental data.

3.1. Substitutional solutions: Liquid, BCC, FCC

The liquid, BCC and FCC phases are described using a substitutional solutionmodel (one sublattice model). The molar Gibbs energy is given by *Eq. 54:*

$$G_m^{\alpha} = x_{Fe}\ {}^0G_{Fe}^{\alpha} + x_W\ {}^0G_W^{\alpha} + RT(x_{Fe}\ln x_{Fe} + x_W \ln x_W) + x_{Fe}x_W L_{Fe,W}^{\alpha} \qquad \textit{Eq. 54}$$

Where x_{Fe}, x_W *are mole fractions of Fe and W respectively.* G_m^{α} [illegible] $L_{Fe,W}^{\alpha}$ [illegible] $L_{i,j}^{\alpha}$ [illegible] *Eq. 52 with linear temperature dependence (Eq. 53).*

3.1. λ-Fe_2W C14-Laves phase

The C14 AB_2 Laves phase crystallizes in the hexagonal $MgZn_2$ structure with three different Wyckoff positions (A on *4f, B on 2a and 6h). The Laves phase is shown as a line compound in the experimental Fe-W phase diagram and has been modeled by Gustafson [48] as such. At present, a two-sublattice model (***$(A,B)_2(A,B)_1$***) is frequently being used and has been implemented in various databases. In the two-sublattice model, the 2a and 6h positions are combined into one sublattice resulting in* $(Fe,W)_2(W,Fe)_1$ ***for the Fe_2W phase and the following expression for the Gibbs energy:***

$$G^{C14} = y_{Fe}^1 y_W^2 G_{Fe:W}^0 + y_W^1 y_{Fe}^2 G_{W:Fe}^0 + y_W^1 y_W^2 G_{W:W}^0 + y_{Fe}^1 y_{Fe}^2 G_{Fe:Fe}^0 + RT[2(y_{Fe}^1 ln y_{Fe}^1 + y_W^1 ln y_W^1) + (y_{Fe}^2 ln y_{Fe}^2 + y_W^2 ln y_W^2)] \qquad \textit{Eq. 55}$$

where $y_{W,Fe}^{1,2}$ [illegible] $G_{Fe:W}^0$ [illegible]

3.2. *μ-phase*

***The μ-phase shows a small homogeneity range according to the experimental data [44,47] that is shifted towards the Fe-rich side of the system at higher temperatures. Furthermore, this phase has a deficiency of W. The common four sublattice model* (Fe,W)$_1$(W)$_4$(Fe,W)$_2$(Fe,W)$_6$ combining two Fe-free** *6c positions (x=0.333 and x=0.165) into one has been used. According to experimental and theoretical investigations of this phase [85], this model allows to cover the whole homogeneity range and is compatible with other systems. According to this sublattice model, the atoms are distributed over the different Wyckoff position as showed in Table 22.*

Space group R-3m, No. 166 Wyckoff position				
3b	*6c$_1$, 6c$_2$*	*6c$_3$*	*18h*	
(Fe,W)	**(W)$_4$**	**(Fe,W)$_2$**	**(Fe,W)$_6$**	**End-member**
Fe	**W**	**Fe**	**Fe**	**Fe_6W_4**
W	**W**	**Fe**	**Fe**	**Fe_8W_5**
Fe	**W**	**W**	**Fe**	**Fe_7W_6**
W	**W**	**W**	**Fe**	**Fe_6W_7**
Fe	**W**	**Fe**	**W**	**Fe_8W_{10}**
W	**W**	**Fe**	**W**	**Fe_7W_{11}**
Fe	**W**	**W**	**W**	**FeW_{12}**
W	**W**	**W**	**W**	**W_{13}**

Table 22 - Atoms placed on the different Wyckoff position constituting the different end-members in the μ phase according to the four sublattice model [85] and name of the different end-members according to this model.

The general expression for the Gibbs energy of the μ-phase is given by Eq. 56:

$$G^{\mu} = y_{Fe}^{1} y_{W}^{2} y_{Fe}^{3} y_{Fe}^{4} G_{Fe:W:Fe:Fe}^{0} + y_{Fe}^{1} y_{W}^{2} y_{Fe}^{3} y_{W}^{4} G_{Fe:W:Fe:W}^{0}$$
$$+ y_{Fe}^{1} y_{W}^{2} y_{W}^{3} y_{Fe}^{4} G_{Fe:W:W:Fe}^{0} + y_{Fe}^{1} y_{W}^{2} y_{W}^{3} y_{W}^{4} G_{Fe:W:W:W}^{0}$$
$$+ y_{W}^{1} y_{W}^{2} y_{Fe}^{3} y_{Fe}^{4} G_{W:W:Fe:Fe}^{0} + y_{W}^{1} y_{W}^{2} y_{Fe}^{3} y_{W}^{4} G_{W:W:Fe:W}^{0}$$
$$+ y_{W}^{1} y_{W}^{2} y_{W}^{3} y_{Fe}^{4} G_{W:W:W:Fe}^{0} + y_{W}^{1} y_{W}^{2} y_{W}^{3} y_{W}^{4} G_{W:W:W:W}^{0}$$
$$+ RT[(y_{Fe}^{1} ln y_{Fe}^{1} + y_{W}^{1} ln y_{W}^{1}) + 2(y_{Fe}^{3} ln y_{Fe}^{3} + y_{W}^{3} ln y_{W}^{3})$$
$$+ 6(y_{Fe}^{4} ln y_{Fe}^{4} + y_{W}^{4} ln y_{W}^{4})] \qquad \text{Eq. 56}$$

No interaction parameters were included in the description of this phase.

4. Optimization method

The optimization of the phase diagram was done using the PARROT module implemented in the Thermo-Calc software [144]. PARROT is based on the least-squares method and allows fitting parameters in the mathematical model chosen for the description of the phases so that they represent the available experimental data.

Each phase of the Fe-W system is modeled separately. For the pure elements Fe and W, we used the unary database from SGTE according to Dinsdale [81] in order to stay consistency with other work and existing databases. The two intermetallic compounds (i.e. C14 Laves and [illegible]

4.1 BCC, Liquid, FCC

For these phases, we used the values of the excess energy given by Gustafson [44] as starting values for our optimization. We started the assessment proedure with the liquid. In addition to the phase boundary data [44], there are thermodynamic data given on the Fe-rich [14, 150] side of the system.

Table 20). While data are well known on the Fe-rich side on the phase diagram, there are less data on the W-side due the experimental difficulties caused by the high temperature and slow diffusivity. In order to model this side of the phase diagram, we used the data from Sinha and Hume-Rothery [44] for the temperature and the composition of the liquid (i.e. 1910 K and 20.6 at. % W). However, the composition of W-BCC was taken from Ichise et al. [143] (i.e. 97.4 at. %), as these data are in agreement with the extrapolation of the data from Antoni-Zdziobek et al. [47] to higher temperature. The thermodynamic data were used with lower weight than the phase boundaries. The data of Sudavstova [148] were only taken with a weight of 20 % of the data from the phase boundary data. A higher weight on these data resulted in a too stable liquid phase which would be inconsistent with the experimental phase diagram data. As previously mentioned in the literature part, the data from [148] are not well documented and can only be used with care. Lowering the weight on the thermodynamic data allowed to converge the optimization of the excess Gibbs energy for the BCC and Liquid and to provide a consistent description in good agreement with experimental data points from the literature [44,47].

At the last step of the optimization of the liquid and BCC phases, we introduced phase boundary data at lower temperature from Takayama et al. [151] and Antoni-Zdziobek et al. [47], in order to check their reliability with the actual description of the BCC phases. As these results immediately were in good agreement, full convergence and agreement between the experiments and the calculated values were quickly reached.

4.2 FCC

The excess Gibbs energy of the FCC-phase was optimized separately from the BCC and Liquid. This phase forms a closed γ [illegible]

4.3 The intermetallic phases: Laves- and μ-phases

As already mentioned in the previous section, two different approaches were taken for the description of these two phases. They will be described in the following section.

a) Using 0K enthalpies of formation from DFT calculations only

The calculated values of the enthalpy of formation from DFT simulations were used in the description of the different G-parameters of the end-members of the intermetallic phases. The data describing "pure" end-members, i.e. those containing one element only, were taken from the literature [3,137]. For λ [illegible]

Table 24 and Table 25, these values are in good agreement with the calculated end-member energies from the present work.

In the Calphad formalism, the enthalpy of formation in the Gibbs energy descriptions of the end-members typically refers to the pure elements (i.e. Fe, W) as given by the GHSERXX functions from Dinsdale [81]. These functions do not include magnetic contributions, which are added separately (for Fe in this case). In the DFT calculations magnetism is taken into account. If the enthalpies of

b) Finite temperature DFT

The results from the phonon calculations (harmonic and quasi-harmonic approximations) were used to obtain a temperature dependent description of the end-member Gibbs energies. They were treated as mathematical functions following the polynomial conventionally used in the Calphad approach as shown in *Eq. 57:*

$$G = A + BT + CTln(T) + D_2T^2 + D_3T^3 + D_{-1}T^{-1} \qquad \textit{Eq. 57}$$

This polynomial can in principle be extended to a higher power series as a function of temperature, but becomes more and more complex without contributing to the improvement of the fit to experimental or calculated values. It has to be noted that in any case this polynomial cannot be extended to low temperatures (□100K). The heat capacity is derived from this function and is given in Eq. 58:

$$C_P(T) = -T\left(\frac{\partial^2 G}{\partial T^2}\right) = -C - 2D_2T - 6D_3T^2 - 2D_{-1}T^{-2} \qquad \textit{Eq. 58}$$

Close to the melting temperature of the compound, the experimental heat capacity curves often show a nonlinear tendency. The D_3 parameter allows to take into account this effect. In the present phonon results, this non-linear behavior of the heat capacity was not found so that the D_3 parameter was not used except for the description of the Fe_7W_6 end-member.

Eq. 58 from 100 K to their high temperature limits using a nonlinear least squares fit. The B parameter of the Gibbs energy function (Eq. 57) was then obtained by fitting the previously obtained parameters (C and D_n) to the entropy curve of the phonon calculations. The resulting parameters (Table 26 and Table 27) were used as starting values for the thermodynamic assessment of the Fe-W system. For the hypothetical end-members, the parameterized Gibbs energy functions were used directly without modification in the assessment. The parameters of the λ [illegible] *Figure 40). The obtained parameters are given in Table 27.*

III. Results and discussions

1. DFT calculations

The results of the energies of formation of the pure elements Fe and W as well as their lattice parameters (output from VASP) are given in *Table 23 where they are also compared with available literature data. A lower energy than in the literature [38,88,107] was noticed in the present work. For Fe, this can be explained by the use of the highest numbers of k-mesh points in the present work, while for W there is no information about the k-mesh in the literature [107].*

			Å	

Table 23 – Energies and lattice parameters of Fe and W in their pure stable state bcc compared with literature.

For the different end-members present in the system (e.g. Laves and □-phases), the enthalpies of formation were calculated according to *Eq. 46. Enthalpy of formation results are presented in Table 24 and Table 25 with their respective optimized lattice parameters for ferro- and non-magnetic states and a comparison with available literature data. Good agreement with literature data can be seen.*

			Δ□ □ □ □	□□		□ □ □	Δ□ □ □ □ □	□□		□ □ □	
□ □	□	□ □ □	-2.83	4.659	7.757	145.86	-0.966	4.668	7.618	143.76	present work
			-8.93	-	-	-	-	-	-	-	Calphad, present work
		11x11x8	0.68	4.678	7.587	143.79					VASP, [155]
			-2.54								Exp., [154]
			-1.85								Exp., [148]
			-3.07	4.71	7.72	148.3	-0.75	4.699	7.61	145.5	VASP, [117]
	W_2Fe	11x11x7	82.29	5.152	8.19	188.29	82.29	5.152	8.19	188.29	present work
		11x11x8	82.6	5.15	8.1865	188.04					VASP, [155]
	□ Fe_2Fe	11x11x7	16.69	4.68	7.63		35.86	4.511	7.278	128.28	present work
		11x11x5	14.71	4.68	7.62	144.3	35.42	4.531	7.288	129.6	VASP, [38]
			38.81	-	-	-					VASP, [156]
		24x24x24	14.7	4.69	7.668	146.1					VASP, [157]
			31.1	-	-	-					VASP, [137]
		11x11x8	38.27	4.53	7.23	128.5					VASP, [155]
	W_2W	11x11x7					44.18	5.19	8.58	200.15	present work
		11x11x8					44.4	5.19	8.57	199.92	VASP, [155]
							43.7				VASP, [137]
		10x10x10						-	-	-	VASP, [120]

Table 24 – Enthalpies of formation of end-members in C14 Laves phase compared with literature [38,117,137,148,154–157].

			Δ			Δ			
			0.46	4.69	25.35	6.15	4.66	24.87	Present work
			-5.8	-	-	-	-	-	Calphad, present work
	Fe_8W_5	9x9x5	6.01	4.75	25.72	8.02	4.74	25.11	Present work
	Fe_7W_6	4x4x1	-3.24	4.73	25.9	-0.46	4.74	25.56	Present work
			-8.17						Calphad, present work
			-0.71						Exp., [148]
μ			-2.52	4.75	25.77	-0.71	4.743	25.30	[117]
	Fe_6W_7	9x9x5	-0.975	4.81	26.02	0.44	4.82	25.74	Present work
			-5.2						Calphad, present work
	Fe_3W_{10}	9x9x5	33.086	5.10	26.86	37.45	5.07	26.79	Present work
	Fe_2W_{11}	9x9x5	37.245	5 .13	27.098	41.08	5.11	27.30	Present work
	FeW_{12}	9x9x5	28.89	5.12	27.47	34.02	5.11	27.46	Present work
	W_{13}	9x9x5				34.53	5.122	28.347	Present work
						36			VASP, [137]

Table 25 – Enthalpies of formation of the end-members in the μ phase in Fe-W system compared with literature [117,137,148].

For the Laves and the μ- phases, the DFT calculations suggest that most of the end-members containing Fe are more stable in their ferromagnetic state so that these data were used in subsequent calculations.

2. Phonon results

In the phonon calculations, the stabilities of the end-members of the Laves and the □-phase were checked using the phonon dispersion curves. For some (hypothetical) end-members, negative (imaginary) phonon frequencies were found in their respective dispersion curves. They are the result of so-called mechanical instability of the structure at compositions of hypothetical end members that do not exist in reality but are nevertheless needed to compute the homogeneity ranges of the phases. In particular, mechanically unstable end-members were found in the □-phase for Fe_7W_6, Fe_8W_5 and FeW_{12}. Several different sets of k-points were tried, but all tested set ups showed negative phonon frequencies. For example, in the FeW_4 end-member Fe is placed on the 6c (z=0.052) position (see *Table 22), whereas in the stable structure this site is occupied by only W (experimentally proven and thermodynamically stable). Thus, the 6c position is highly unfavorable to be occupied by Fe. Furthermore, this end-member has a stoichiometry close to the composition of the Laves phase which is thermodynamically stable. Due to these reasons, no optimized structure reached a local minimum in the configurational space [83] leading to mechanical instability of the end-member in the phonon calculations. Negative phonon frequencies can be observed in a high amount. If in some cases these negative phonon frequencies can be seen as a residual artifact and a new optimization of the geometry of the crystal structure is necessary it is not the case here. The dispersion curves of* μ [illegible]

[illegible] *Figure 32.*

In addition, the heat capacity at constant pressure for Fe_2W is given.

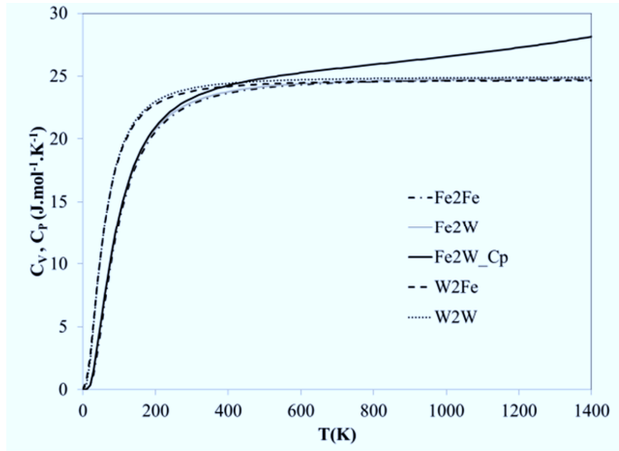

Figure 32 – Calculated heat capacity at constant volume from phonon calculations for the different end-members in the Laves phase. The heat capacity at constant pressure of the stable compound Fe_2W is given as black line obtained from quasi-harmonic approximation phonon calculations.

For Fe_7W_6, using 9x9x5 k-mesh points provided higher energies when optimizing the geometry than using a set of 4x4x1 k-mesh points. For both sets of k-mesh points, we used the optimized structure to compute phonon calculations. Using optimized geometry from 9x9x5 k-mesh point, negative phonon frequencies were present whereas this was not the case for the structure from 4x4x1 k-mesh points. To calculate the thermodynamic properties we used the optimized geometry structure from 4x4x1 k-mesh points as it represents the local minimum ground state for this structure.

The heat capacity curves are given in Figure 32 and Figure 33 for the Laves and μ-phases, respectively. All the computations of the heat capacity at constant volume reach the value of Dulong-Petit of 25 J.mol^{-1}.atom^{-1} at high temperature. For the Calphad modeling, they have been described as given in Eq. 57. The obtained parameters are given in Table 26 and Table 27 for the different end-members in the Laves and μ-phases, respectively. Nevertheless, for the thermodynamic modeling, the pure end-members λ

Eq. 57 to describe the heat capacity curves of the phonon results were then adjusted from optimization when necessary.

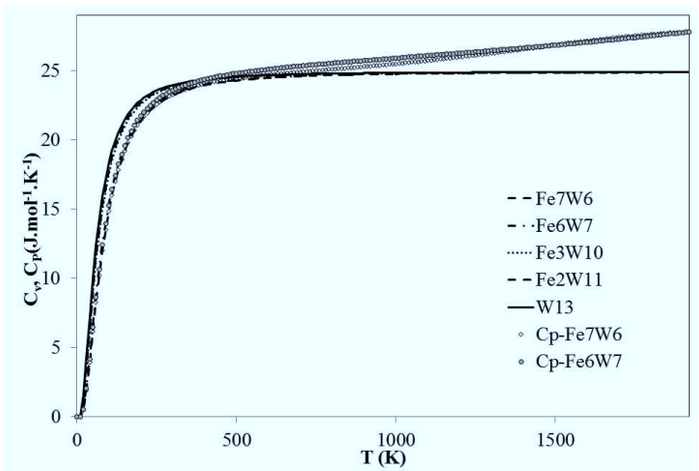

Figure 33 –Heat capacity at constant volume and pressure for the different end-members in the μ phase. The data of the end-members which showed imaginaries frequencies are not shown here.

	Magnetism	*SC*	*A*	*B*	*C*	D_2	D_{-1}
Fe_2Fe	*FM*	*2x2x2*	*50070*	*397.02*	*-72.02*	*-1.125e-3*	*181868.8*
Fe_2W	*FM*	*2x2x2*	*-8490*	*397.1*	*-72.11*	*-2.93e-3*	*190812.9*
FeW_2	*NM*	*3x3x1*	*246880*	*368.55*	*-73.41*	*-2.93e-4*	*95255.9*
W_2W	*NM*	*2x2x2*	*103590*	*374.94*	*-74.15*	*-2.94e-4*	*97122.9*

Table 26 – Optimized parameters obtained by fitting the phonon results to Eq. 58 for the end-members in the Laves phase and used as starting values for Fe_2W and W_2Fe description on the thermodynamic phonon phase diagram (SC: supercell).

Table 27 – Fitting of the phonon heat capacities curves for the μ phase according to Eq. 58 and used as starting values for the thermodynamic modeling of the phonon phase diagram.

The stable end-members (i.e. λ μ μ λ μ Figure 34, Figure 35 and Figure 36, where for each volume point the phonons were calculated. From these calculations, the heat capacity at constant pressure is obtained (Eq. 50). The heat capacities at constant pressure for λ μ Figure 39 and Figure 40. The fitted results (Eq. 57) were then used for the descriptions of these end-members in the phonon phase diagram.

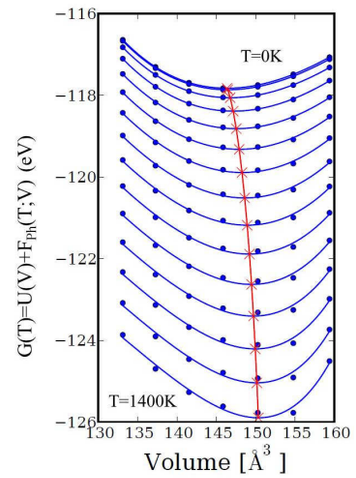

Figure 34 – Gibbs energy of Fe_2W in QHA approximation as a function of the unit cell and temperature. The minimum values of the fitted thermodynamic calculations are given by the red crosses.

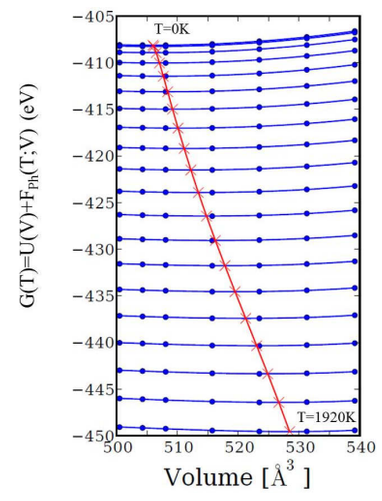

Figure 35 - Gibbs free energy (G (V, T)) of μ-Fe_7W_6 calculated using the QHA approximation. The point denotes the calculated G (V, T) at different volumes, the red crosses are the minimization of the curve according to the Vinet equation of state.

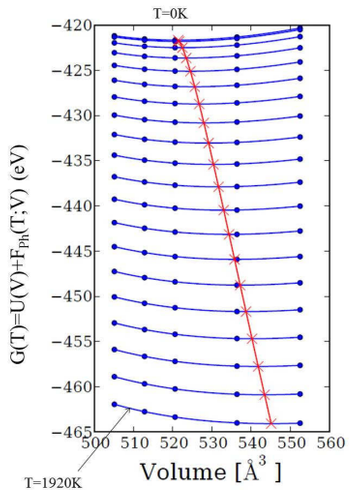

Figure 36 - Gibbs free energy (G(V,T)) of μ-Fe_6W_7 calculated using the QHA approximation.

3. Thermodynamic optimization

As mentioned in the previous part the liquid, BCC and FCC phases were modeled independently from the DFT and phonon calculations. Nevertheless as last step of the optimization, the use of DFT and/or phonon calculations influence the interaction parameters of the BCC phase. It turns out that the L_0 parameters of the BCC had to be adjusted depending on the use of the DFT or phonon. As the BCC phase is in direct interaction with the Liquid and FCC phases, their L_0 parameters were also adjusted depending on the use of DFT or phonon calculations.

3.1. DFT based phase diagram

The end-members of the intermetallic phases were defined with their respective enthalpies of formation obtained from DFT calculations (*Table 24* and *Table 25*). The enthalpies of formation of several end-members were optimized using the calculated enthalpies of formation as experimental values as the function of pure Fe described by the GHSERFE function [81] which does not include the contribution of magnetism. The obtained optimized enthalpies of formation are given in *Table 24* and *Table 25* and compared with the DFT values. There is a difference about 8 $kJ.mol^{-1}$ per Fe atom (see *Figure 24*) arising from the magnetism of Fe which is not included in the Dinsdale polynomial [81].

Table 28. The calculated phase diagram obtained from this optimization is shown in Figure 37 compared with experimental data. The calculated invariant reactions obtained from this phase diagram are given in Table 30.

	${}^{0}G^{C14}_{Fe:Fe} = 3\ {}^{0}G^{BCC\_A2}_{Fe} + 44130$	
	${}^{0}G^{C14}_{Fe:W} = 2\ {}^{0}G^{BCC\_A2}_{Fe} + {}^{0}G^{BCC\_A2}_{W} - 26803.6 + 13.5T$	
	${}^{0}G^{C14}_{W:Fe} = {}^{0}G^{BCC\_A2}_{Fe} + 2\ {}^{0}G^{BCC\_A2}_{W} + 246880$	
	${}^{0}G^{C14}_{W:W} = 3\ {}^{0}G^{BCC\_A2}_{W} + 131400$	
μ	${}^{0}G^{\mu}_{Fe:W:Fe:Fe} = 9\ {}^{0}G^{BCC\_A2}_{Fe} + 4\ {}^{0}G^{BCC\_A2}_{W} - 76287.8 + 46.48T$	
	${}^{0}G^{\mu}_{W:W:Fe:Fe} = 8\ {}^{0}G^{BCC\_A2}_{Fe} + 5\ {}^{0}G^{BCC\_A2}_{W} + 78213$	
	${}^{0}G^{\mu}_{Fe:W:W:Fe} = 7\ {}^{0}G^{BCC\_A2}_{Fe} + 6\ {}^{0}G^{BCC\_A2}_{W} - 106224.1 + 48.93T$	
	${}^{0}G^{\mu}_{W:W:W:Fe} = 6\ {}^{0}G^{BCC\_A2}_{Fe} + 7\ {}^{0}G^{BCC\_A2}_{W} - 67688.98 + 80T$	
	${}^{0}G^{\mu}_{Fe:W:Fe:W} = 3\ {}^{0}G^{BCC\_A2}_{Fe} + 10\ {}^{0}G^{BCC\_A2}_{W} + 430118$	
	${}^{0}G^{\mu}_{W:W:Fe:W} = 2\ {}^{0}G^{BCC\_A2}_{Fe} + 11\ {}^{0}G^{BCC\_A2}_{W} + 484188$	
	${}^{0}G^{\mu}_{Fe:W:W:W} = 1\ {}^{0}G^{BCC\_A2}_{Fe} + 12\ {}^{0}G^{BCC\_A2}_{W} + 375549$	
	${}^{0}G^{\mu}_{W:W:W:W} = 13\ {}^{0}G^{BCC\_A2}_{W} + 469300$	

Table 28 – Thermodynamic parameters for the description of the DFT phase diagram.

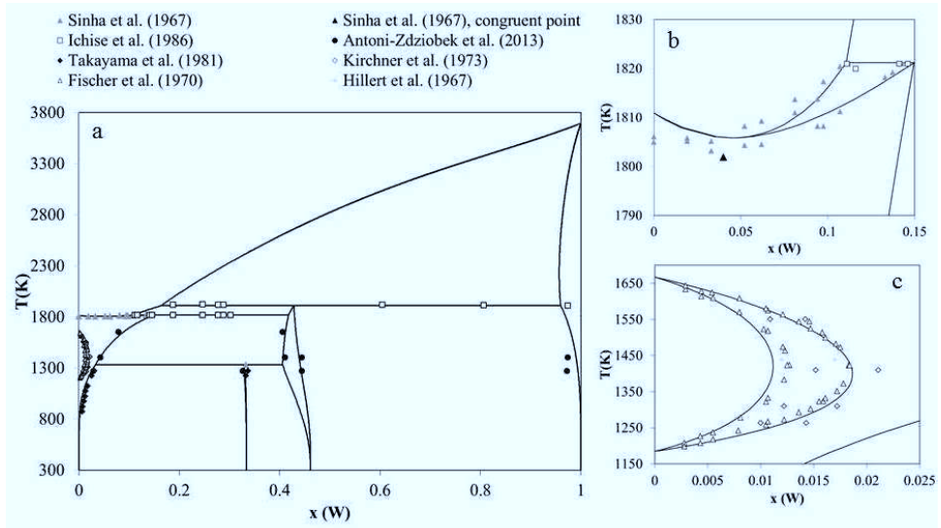

Figure 37 - Calculated phase diagram (solid line) using DFT calculations for the description of the end-members compared with experimental data [44,45,47,143,151–153]. a) Full range of the phase diagram, b) Congruent point on the Fe-rich side, c) Gamma loop.

3.2. Phase diagram based on phonon calculations

The calculated phase diagram obtained using phonon calculation is given in *Figure 38 and their respective parameters in Table 29. The particularity of our phonon calculations is that they describe a Gibbs energy function for a fixed site occupation as they are calculated for each end-member whereas the phase itself is described by a mixed occupation, which is modeled by the sublattice model formalism. The principle of the Calphad method is the minimization of the Gibbs energy, the calculation of the phase diagram is done by using the site fractions that minimize it. The use of phonon results can easily be handled for the description of ordered phases as e.g. the Laves phase. However, in the case of the μ-phase e.g. the* Fe_7W_6 *stoichiometry can be achieved by full ordering on the sublattices or mixed occupancies. As Thermo-Calc minimizes the Gibbs energy of the phase over the sublattices it results in a mixed occupancy for a given composition while the phonon data were generated for the ordered end member. As a consequence, the Gibbs energy for the composition* Fe_7W_6 *obtained from Thermo-Calc and phonon calculations deviate. In order to make comparisons with phonon data for the*

μ

μ

μ

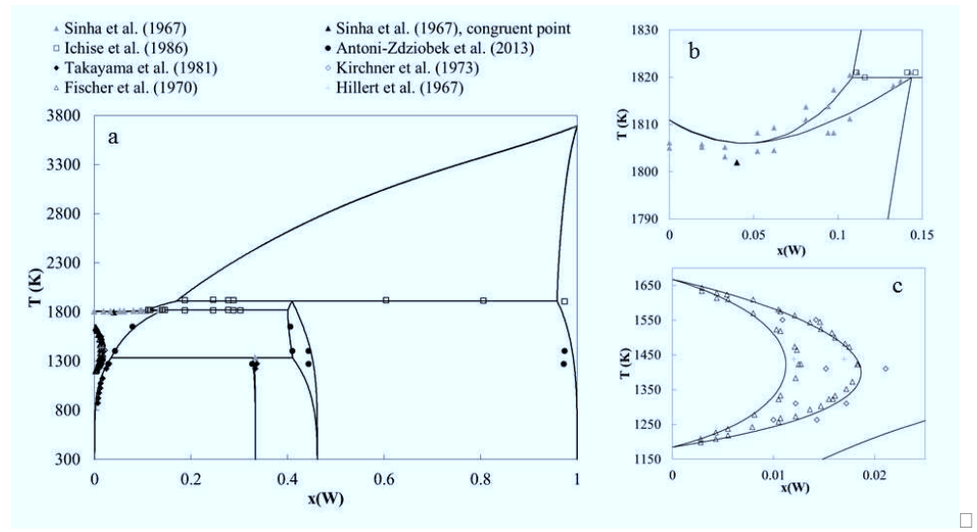

Figure 38 - Calculated phase diagram with phonon calculations for the description of the end-members compared with experimental data [44,45,47,143,151–153]. a) Full range of the phase diagram, b) Congruent point on the Fe-rich side, c) Gamma loop.

As the description of pure Fe does not include the magnetic contribution in the description given by Dinsdale [81], we optimized the enthalpy of formation of the end-members in the same way as in the DFT based phase diagram. The hypothetical end-members that are highly unstable had no need to be adjusted, whereas the stable end-members had to be fitted to the DFT results (Table 24 and Table 25) used as experimental data. The enthalpy of formation of Fe_9W_4 *also had to be optimized as it influences the phase boundary of the μ-phase on the Fe-side and also the Laves phase temperature dependence. For the mechanically unstable end-members (no heat capacity description from phonon*

	$^{0}G^{C14}_{Fe:Fe} = 3\ ^{0}G^{BCC\_A2}_{Fe} + 44130$	
	$^{0}G^{C14}_{Fe:W} = -31100.4 + 376.7T - 70.434TlnT - 4.92E^{-3}T^{2} + 166642T^{-1}$	
	$^{0}G^{C14}_{W:Fe} = +246880 + 368.28T - 73.5TlnT - 2.98E^{-4}T^{2} + 100893T^{-1}$	
	$^{0}G^{C14}_{W:W} = 3\ ^{0}G^{BCC\_A2}_{W} + 131400$	
μ	$^{0}G^{\mu}_{Fe:W:Fe:Fe} = 9\ ^{0}G^{BCC\_A2}_{Fe} + 4\ ^{0}G^{BCC\_A2}_{W} - 76329 + 39.68T$	
	$^{0}G^{\mu}_{W:W:Fe:Fe} = 8\ ^{0}G^{BCC\_A2}_{Fe} + 5\ ^{0}G^{BCC\_A2}_{W} + 78213$	
	$^{0}G^{\mu}_{Fe:W:W:Fe} = -141384.5 + 1685T - 315.63TlnT - 5.1419E^{-3}T^{2} - 1.3199E^{-6}T^{3} + 694229.8T^{-1}$	
	$^{0}G^{\mu}_{W:W:W:Fe} = -111740.6 + 1697.2T - 314.1TlnT - 0.01214T^{2} + 647792.1T^{-1}$	
	$^{0}G^{\mu}_{Fe:W:Fe:W} = +430118 + 1680.9T - 321.69TlnT - 8.17E^{-4}T^{2} + 510840.6T^{-1}$	
	$^{0}G^{\mu}_{W:W:Fe:W} = +484185 + 1675.9T - 322.00TlnT + 7.198E^{-4}T^{2} + 491025.1T^{-1}$	
	$^{0}G^{\mu}_{Fe:W:W:W} = 1\ ^{0}G^{BCC\_A2}_{Fe} + 12\ ^{0}G^{BCC\_A2}_{W} + 375549$	
	$^{0}G^{\mu}_{W:W:W:W} = 13\ ^{0}G^{BCC\_A2}_{W} + 469300$	

Table 29 – Thermodynamic parameters for the description of the phonon phase diagram.

In Figure 39 and Figure 40 the C_P curves of λ [illegible] μ [illegible] λ [illegible] μ [illegible]

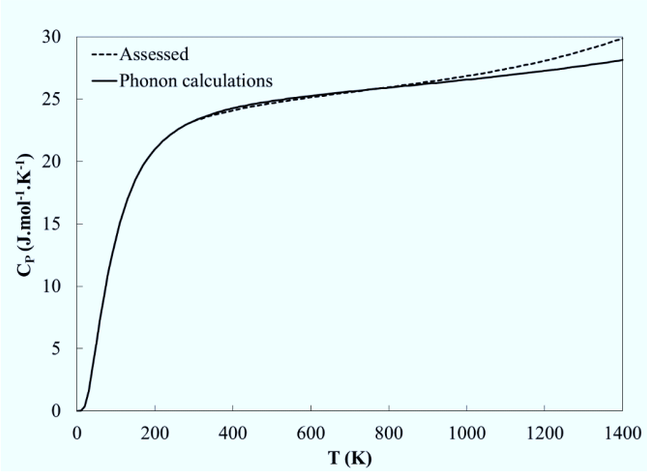

Figure 39 – Heat capacity of Fe_2W Laves phase calculated from phonon quasi-harmonic approximation (C_p) and Calphad.

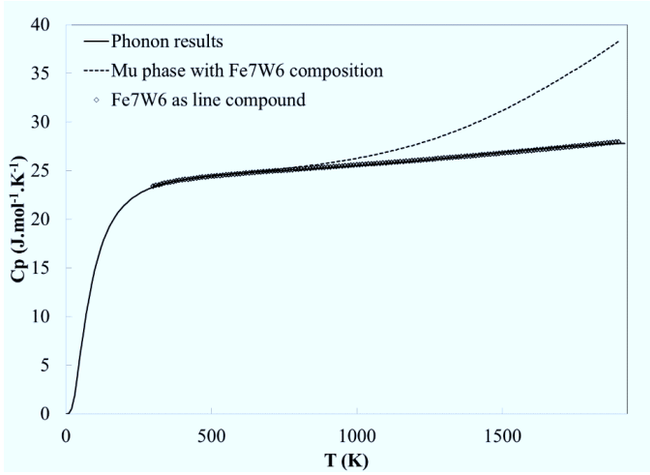

Figure 40 – Heat capacities of μ-Fe_7W_6 calculated from the phonon thermodynamic assessment compared with results from quasi-harmonic approximation.

3.3. <u>Comparison of the phase diagrams</u>

The two proposed optimized phase diagrams calculated from the respective datasets are given in Figure 41. In their general outline, they show a good agreement, and only differ in homogeneity range of the μ-phase. In the description of the phonon-based phase diagram, the homogeneity range of this phase is slightly bigger and has a phase boundaries with more pronounced curvature. In both phase diagrams, the homogeneity range of the μ

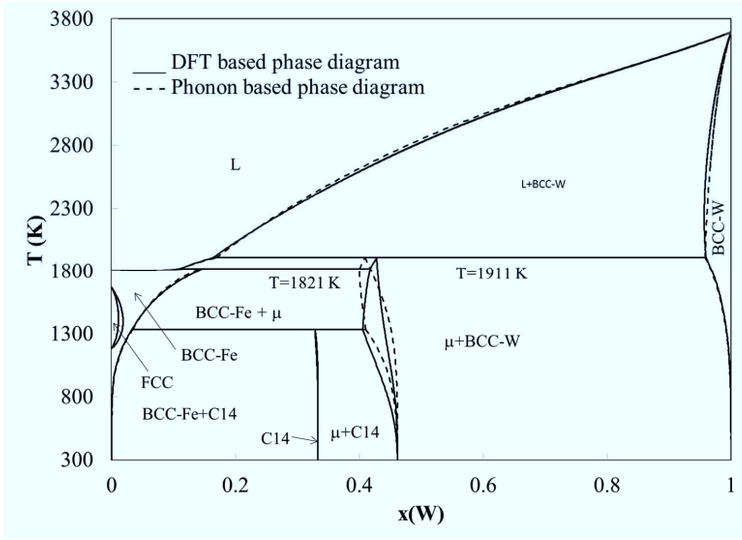

Figure 41 – Comparison of the two optimized phase diagram, with solid lines the calculated phase diagram from DFT and with dotted lines the calculated phase diagram using phonon calculations.

For both phase diagrams, the data of the invariant reactions are listed in Table 30 with their respective temperatures and phase compositions. The calculated invariant reactions from both phase diagrams are in very good agreement with experimental data (Table 20). The largest deviation from the experiments is found for the congruent melting point of the BCC phase given at 1802 K by Sinha and Hume-Rothery [44] and calculated at 1806 K using our thermodynamics descriptions. The difference of 4 K is considered acceptable due to the use of a melting temperature of BCC-Fe by Sinha and Hume-Rothery [44] 5 K below the currently accepted temperature in [45].

μ□	□ □ □ □ □ □ □ □ □ □ □	□ □ □ □ □ □ □ □ □ □ □
□ μ□ □ □	□ □ □ □ □ □ □ □ □ □ □	□ □ □ □ □ □ □ □ □ □ □
	□ □ □	□ □
□ □μ	□ □ □ □ □ □ □ □ □ □ □	□ □ □ □ □ □ □ □

Table 30 – Calculated invariant reactions obtained from the optimized phase diagrams based on DFT and phonon calculations.

The calculated enthalpies of mixing of liquid as a function of composition at 1□00 K are shown in *Figure 42, where good agreement with the data from Sudavstova [148] can be seen.*

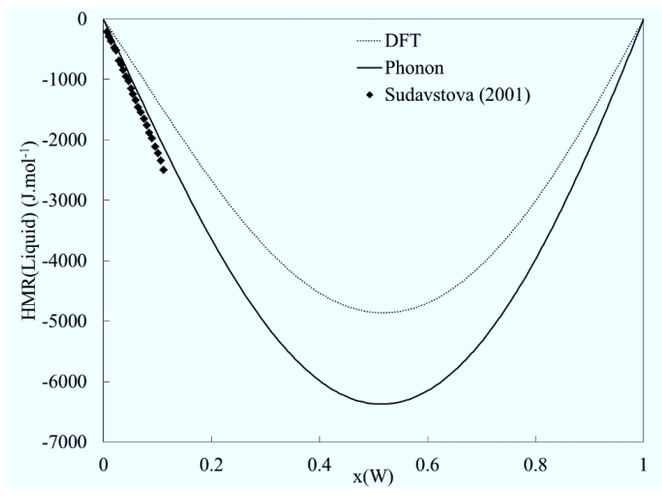

Figure 42 – Enthalpy of mixing of liquid at 1900 K calculated from the DFT and phonon optimized phase diagrams compared with data from Sudavtsova [148].

The two optimized phase diagrams show that with the progress of atomistic simulation (i.e. DFT, phonon) allow to access thermodynamic properties of intermetallic phases where experimental

Conclusion

In the present work, computational tools (DFT, phonon) were used to describe the two intermetallic phases (Laves and □-phases) where thermodynamic data were missing or controversial. As any optimization of phase diagram can be better derived with better knowledge of the thermodynamic properties of the intermetallic phases, DFT and phonon data are useful tool to obtain missing thermodynamic data.

The use of phonon calculated data could be seen as a great advantage for the description of the thermodynamic data where there are no experimental data. Nevertheless, their use should be taken with great care as they can lead to the creation of an artificial miscibility gap due to the minimization of the Gibbs energy through the sublattice as implemented in the different Calphad software codes.

In conclusion, the phonon data can be used for a better description of □ordered□ phases (e.g. the Laves phase in our study). However, for partially disordered phases they should be used with care.

The two proposed phase diagrams have shown to be consistent with the thermodynamics of the system. Two versions of the phase diagram are presented in order to leave the choice for the next user which description to be used in higher order systems.

Chapter V – The Cr-Fe-Nb system

Introduction

In the present study, the Cr-Fe-Nb ternary system was evaluated experimentally (isothermal sections, solidification and thermal behavior) and computationally (DFT and Calphad modeling) in order to have a full understanding of the phase equilibria. The present experimental data were used for the thermodynamic optimization of the system.

The study of the Cr-Fe-Nb ternary system is divided in three different sections dedicated to the different aspects of phase equilibria and methods for their determination as follows:

- Experimental determination of the isothermal sections at 700°C, 1050°C and 1350°C
- Thermal and solidification behavior of the Cr-Fe-Nb system
- Thermodynamic modeling of the Cr-Fe-Nb ternary system

Literature

A literature survey had been given in the literature survey (p. 25). The system has been studied by Kaloev et al. [66,67] at two different temperatures (i.e. 700 and 1000°C), including the determination of phase equilibria using quantitative SEM. Their results are reproduced in the system report of Landolt-Börnstein [69] with a few modifications due to new findings in the limiting binary systems.

To the knowledge of the literature, this system doesn't contain any ternary compound. In contrast a high solubility of a third element is observed in the binary phases. BCC-(Fe,Cr) form a mutual continuous solid solution at high temperatures. The dissolution of Cr in the binary phase C_2Nb-Fe laves phase is particularly high. This phase is reported to form a quasibinary system with the corresponding C_2Nb HT and LT (C14 and C15) phases which have limited solubility of Fe [158]. This would correspond to a local minimum in the ternary system as it is below the binary invariant reaction. This postulation, however, has not been proven until now and needs to be checked.

Mansour et al. [159] have investigated the temperature dependence of the Cr-Fe-Nb system in the Fe-rich corner. In their investigation they never referred to the existing knowledge of the system. They

γ [illegible]

[illegible]

[illegible]

[illegible]

[illegible]

μ [illegible]

[illegible]

[illegible]

[illegible]

[illegible]

[illegible]

[illegible]

[illegible]

[illegible]

[illegible]

[illegible] *Table 31.*

Phase	Pearson Symbol	Space Group	Struktur bericht designation	Prototype	Lattice parameters [pm]
(Fe)	cI2	Im-3m	A2	W	286.64
γ-Fe	cF4	Fm-3m	A1	Cu	365.99
(Cr)	cI2	Im-3m	A2	W	288.4
(Nb)	cI2	Im-3m	A2	W	330
Cr_2Nb	cF24	Fd-3m	C15	$MgCu_2$	518.6
Fe_2Nb	hP12	$P6_3/mmc$	C14	$MgZn_2$	a=484.14
					c=789.33
Fe_7Nb_6	hR13	R-3m	$D8_5$	Fe_7W_6	a=492.6
					c=2680
σ				σ	

Table 31 - Crystallographic data of all phases involved in the present study of Cr-Fe-Nb.

I. Experimental determination of the isothermal sections at 700°C, 1050°C and 1350°C

1. Experimental

Samples in ternary systems have been prepared from high purity metals Fe (MaTeck, 99.99 %), Nb (99.99 %, MaTeck), Cr (99.99 %, Alfa Aesar) by levitation induction heating method under high purity Ar atmosphere on a home-made device. The levitation chamber was evacuated to 10^{-5} mbar and refilled with Ar before melting the samples. The samples were then melted at least three times and turned upside down after each melting process in order to ensure a good homogenization of the samples. After alloying, the total mass of each samples was checked, the loss was less than 0.7 % from the predicted mass.

In the first step, the samples were crushed into several pieces and checked carefully with respect to inhomogeneity. No samples were found with inhomogeneity.

In the present work, three different isothermal temperatures, 700°C 1050°C and 1350°C were studied. For the two lowest temperatures, the samples were placed in alumina crucibles that were sealed in evacuated quartz tubes (10^{-5} mbar) and placed in a tubular furnace under Ar. Samples to be annealed at

α □ □ □ □ □

□□ □ □ □ □□□□ □□□ □ □ □

□□□□ □ □□□□□□ □ □

□□ □ □□□□ □ □□□□ □ □□□□□□ *Table 31.* □ □□□

2. Results and discussion

Information about the crystal structures present in the system are given in *Table 31. The selected samples for each isothermal section are given in Table 33, Table 34 and Table 35 with their respective annealing time as well as their chemical composition determined by EDX and their crystallographic structures obtained from XRD.*

From the results obtained by SEM/EDX and XRD as given in Table 33, Table 34 and Table 35, the three isothermal sections at 700, 1050 and 1350°C were constructed and are given in Figure 43, Figure 44, Figure 45, respectively.

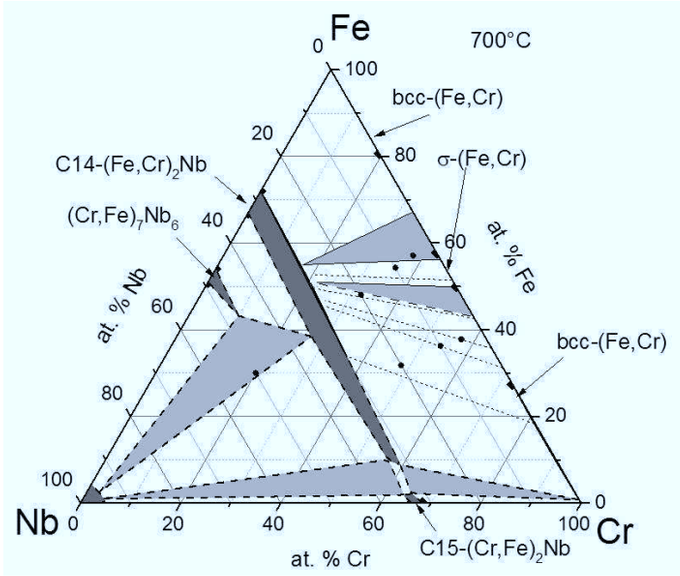

Figure 43 - Isothermal sections of Cr-Fe-Nb given at 700°C. The results showed in dashed line were extrapolated from higher temperature isothermal sections as well from binary data.

In the 700°C isothermal section, some of the results were extrapolated from higher isothermal sections, binary systems and from Kaloev et al. [67] in order to determine the different three phase fields that could not be determined with our selected samples. The results from the extrapolations are indicated by dashed lines.

The main features of this phase diagram are the extension of the two binary Laves phases (C15 on the Cr-Nb side and C14 on the Fe-Nb side) into the ternary, resulting in broad homogeneity ranges (see Figure 43, Figure 44 and Figure 45).

The change of Laves phase polytype is featured by a narrow two phase field region. The $(Fe,Cr)_2Nb$ laves phase crosses the whole phase diagram and cuts itinto two parts. On the Fe-Nb side, there is an extension of the μ

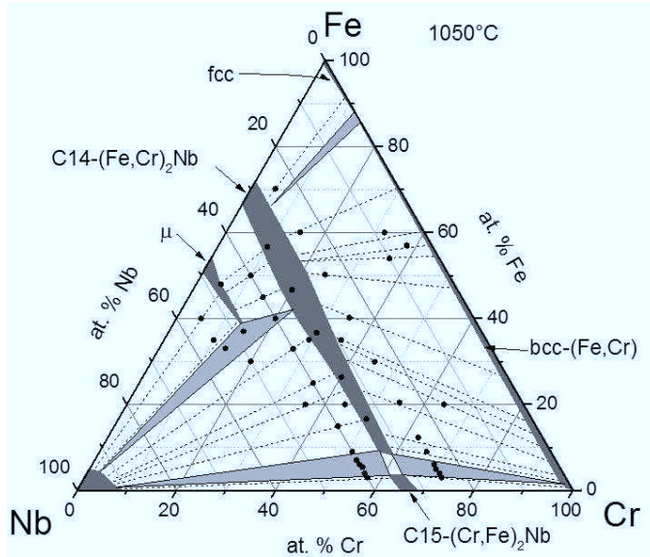

Figure 44 - Isothermal section at 1050°C. Phase equilibria are drawn according to the experimental results given in Table 34.

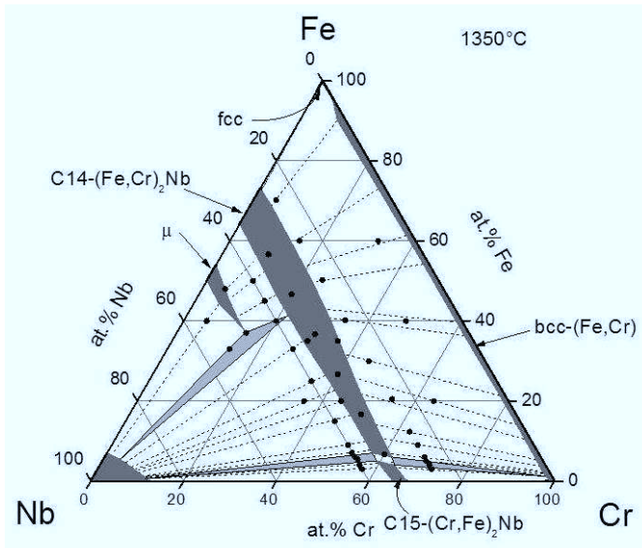

Figure 45 - Isothermal section at 1350°C according to the experimental results from SEM/EDX and XRD given in Table 35.

2.1 Extension of C15 and C14 laves phase $(Fe,Cr)_2Nb$ in the ternary system

The three different isothermal sections *(Figure 43, Figure 44 and Figure 45) show an extension from Fe_2Nb to Cr_2Nb of the Laves phase with a change of polytype at low Fe content on the Cr_2Nb side. The C15 laves phase is stable in the Cr-Nb binary system over the complete temperature range up to its congruent melting point [18,28,29], whereas the C14 laves phase type is stable in the Fe-Nb binary system. It is a common phenomenon that small additions of a third element result in a polytype change see for example the effect of Al in Cr-Nb-Al [18,160].*

The addition of Fe to Cr_2Nb implies a change of structure polytype from C15 to C14. The two structure polytypes, cubic C15 and hexagonal C14 are closely related [10,18,160]. The change of structure polytype is due to an increase of the electron concentration by adding Fe, more favorable as C14 structure polytype. Furthermore the C14 crystal structure is more flexible with respect to the addition of a third element [160,161], which results in the frequent occurrence of C14 type Laves phases in ternary systems.

The C15 Laves phase can dissolve a certain amount of Fe, estimated up to 7 at. % by Grujicic et al. [68] at 1200°C. The two higher isothermal sections (Figure 44 and Figure 45) of the present work suggest a lower amount of Fe dissolving into the C15 laves phase (3.6 at. % Fe at 1050°C and 5 at.% Fe at. % 1350°C). By increasing the temperature, a higher amount of Fe can be dissolved into the C15. The dissolution of Cr into the C14 is also higher at higher temperature (i.e. 59.2 and 61.9 at. % Cr at 1050 and 1350°C, respectively).

Due to the structural similarities, the two phase field [C15-Cr_2Nb C14-Fe_2Nb] is difficult to determine and was established from the combined results obtained by SEM, EBSD and XRD. With microstructure evaluations from SEM, it was not possible to distinguish the two different Laves phases (see *Figure 46). Nevertheless, the XRD evaluation suggested the presence of two different Laves phase polytypes in the relevant samples (21, 22, 48, 49 on the Cr-rich side and samples 24, 25, 45, 46 on the Nb-rich side, see Table 34). Electron backscattered diffraction (EBSD) was therefore employed for the evaluation of the two phase field. EBSD phase maps are shown as examples for two different samples 22 ($Cr_{69}Fe_6Nb_{25}$) and 25 ($Cr_{54}Fe_6Nb_{40}$) (Figure 47) annealed at 1050°C on each side of the*

Figure 47. The two different polytypes of Laves phase can then be observed as a fine microstructure (salt and pepper mixture). From these results, we estimated the two phase region C14-C15 to be about 4.9-5.8 at. % at 1050°C and about 2-2.8 at. % at 1350°C. On the Cr-rich side the two phase field region is narrower.

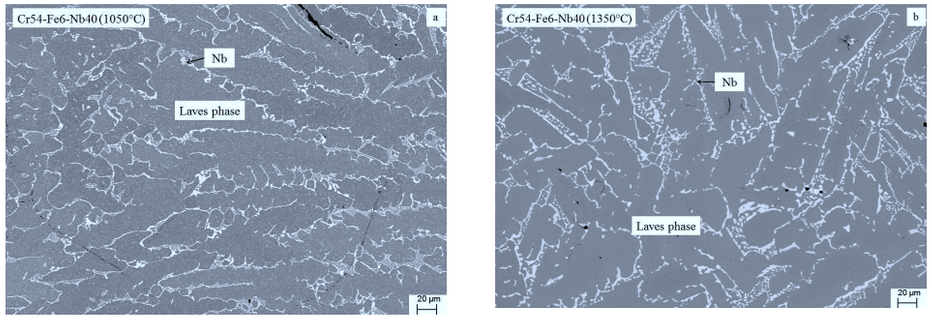

Figure 46 - Metallography investigation of sample 25 (Cr54Fe6Nb40) in the three phase field (C15+C14+Nb) annealed at a) 1050°C, b) 1350°C.

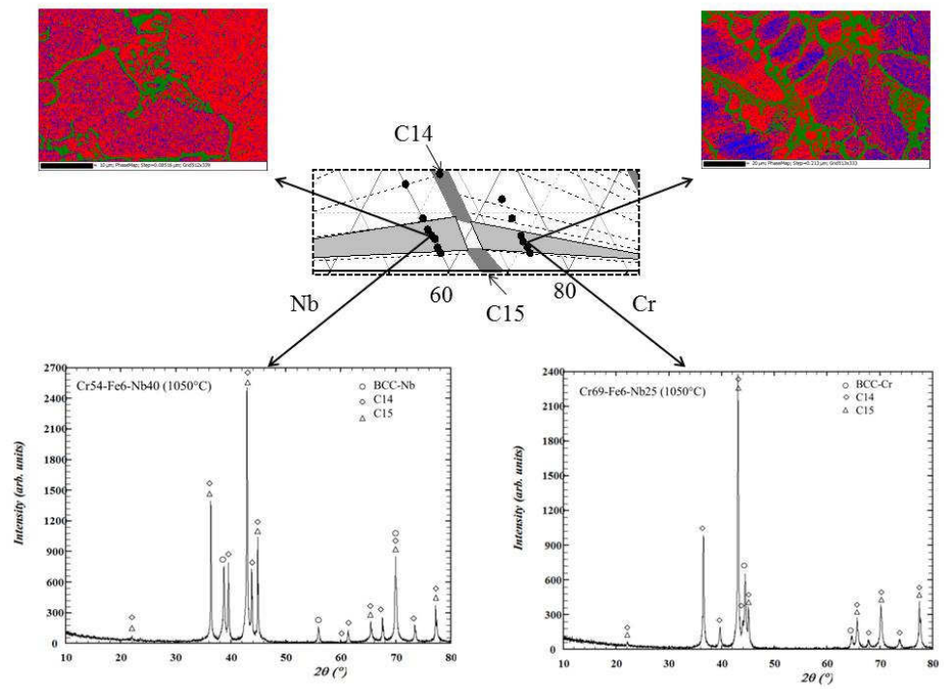

Figure 47 –EBSD phase maps for the 1050°C isothermal section for the determination of the phase field between the C14 and C15 Laves phase together with the evaluation of the structures with XRD. For the two upper pictures, the different colors represent, red=C14, blue=C15 and green=BCC.

On each side of the Laves phase, the lattice parameters, volumes as well as c/a ratio in C14 were determined from samples placed along 25 and 40 at.% Nb and annealed at 1050°C and 1350°C, respectively (*Figure 48* and *Figure 49*). The lattice parameter in the C14 laves phase follow a linear tendency with the increase of Cr content which is consistent with a continuous solid solution. There is then a discontinuity on the lattice parameters once the system reaches the boundary of the two phase field (C14-C15), this is shown by the dotted line in *Figure 48* and *Figure 49*. The lattice parameters as well as the c/a and volumes show a deviation from the linear tendency observed at higher Cr content. At 1350°C, the two phase field region is reached at 56.1 at. % Cr showed by a break in the increase of the linear tendency of the c/a ratio.

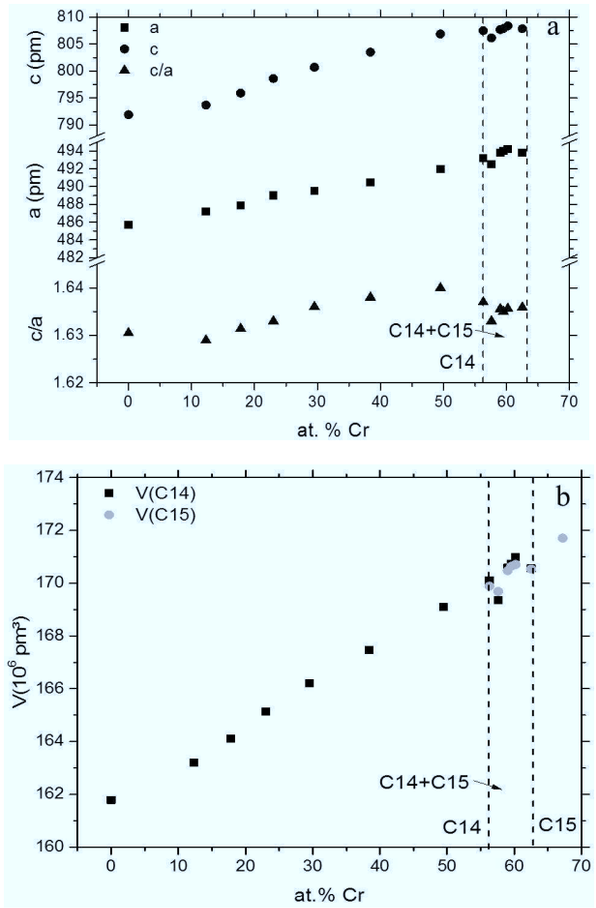

Figure 48 – a) Lattice parameters and b) unit cell volume of the Laves phase determined by XRD for samples with 40 at. % Nb after annealing at 1050 °C. Data for binary Cr_2Nb and Fe_2Nb at 1100 °C were taken from reference [34].

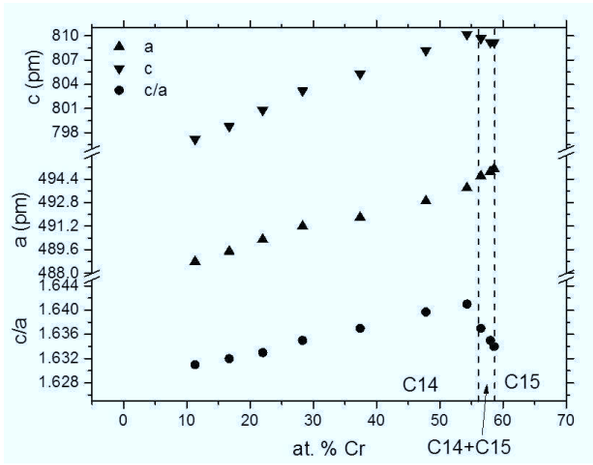

Figure 49 – Lattice parameters and c/a ratio of the C14 phase at 1350°C along the section of 40 at. % Nb.

Some samples show the presence of C36 laves phase structure (Sample 47 at 1350°C for example, see Table 35). Grujicic et al. [68] also found this phase in their investigation on the addition of Fe into Cr_2Nb. This phase is metastable and is an intermediate phase between C14 and C15 [14], its formation was found in samples which are close to the boundary between the two phase field and the C14 phase. The C36 phase forms during quenching, which can be difficult at high temperature and if done too slowly result in the formation of this phase.

2.2 <u>The Nb rich side</u>

With the highest melting point from the three pure compounds, Nb solid solution extends into the ternary system with an increase of solubility of Fe and Cr by increasing the temperature. The Nb solid solution forms two three phase fields:

- A three phase field is formed on the Fe-Nb side, Nb is in equilibrium with the [illegible] *Figure 50)*
- On the Cr-Nb side, where Nb, C15 and C14 laves phase are in equilibrium and form a narrow three phase field region. This phase was already previously discussed.

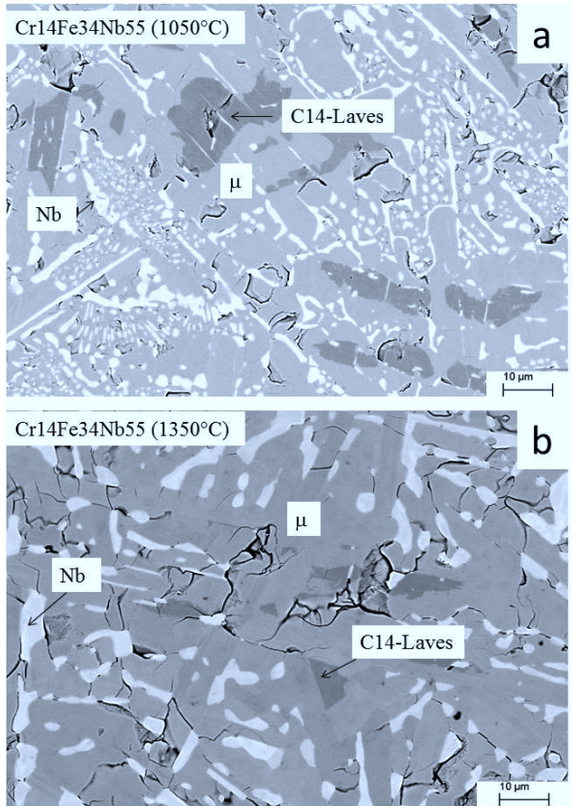

Figure 50 – Backscattered electron SEM images of the microstructure of the sample 28 (Cr14Fe34Nb55) annealed at a) 1050°C and b) 1350°C showing the three phase fields Nb+μ+C14.

The μ

μ *Figure 51 as a function of Cr content. As the concentration of Cr increases the lattice parameters (a and c) increase linearly which is consistent with the homogeneity range of the* μ

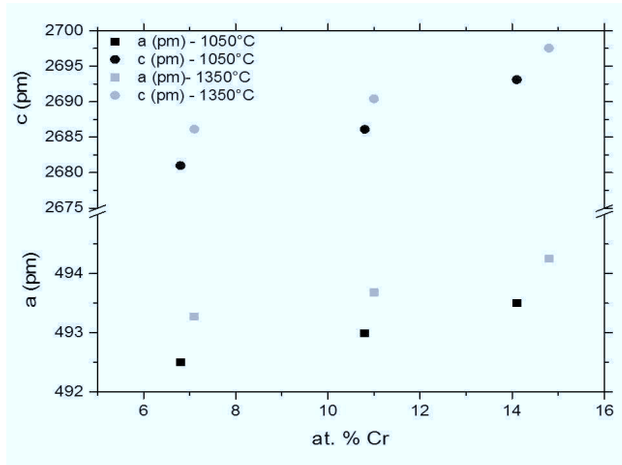

Figure 51 - Lattice parameters of the μ phase as a function of the Cr content after annealing at 1050°C and 1350°C.

In the isothermal section at 1050°C, for several samples surrounding the μ *Table 34) with a composition very close to the* μ *Table 32). This phase is in equilibrium with the* μ η η

Table 32 – Refinement of the crystal structure T (η).

In the ternary Cr-Fe-Nb phase diagram, Kaloev etal. [66] did not mention the presence of this phase. In addition, Malfliet et al. [164] investigated the influence of oxygen on Cr-Fe-Nb (in the Fe-Nb rich side). For the samples without oxygen treatment, their findings agreed well with the results of Kaloev et al. [66]. Nevertheless, they found that only a small amount of oxygen can lead to the formation of a quaternary phase with a structure type $NiTi_2$. Our evaluation of the crystal structure T shows that Nb occupies the 48f Wyckoff position, Fe and Cr shared the 16d and 32e positions. Refining the atomic position showed that Fe and Cr shared at 1:1 the 16d position whereas Fe fully occupies the 32e Wyckoff position. This finding is in very good agreement with the results of the oxygen treated Cr-Fe-Nb samples of Malfliet et al. [164] (see Table 5 of the original paper). As shown by the literature [162,164] this η [illegible]

2.3 <u>The Cr-Fe side</u>

In the binary Cr-Fe, there is one intermetallic phase σ([illegible]

σ [illegible] σ [illegible] *Figure 52* [illegible] *a) and the XRD evaluation (Figure 52b).*

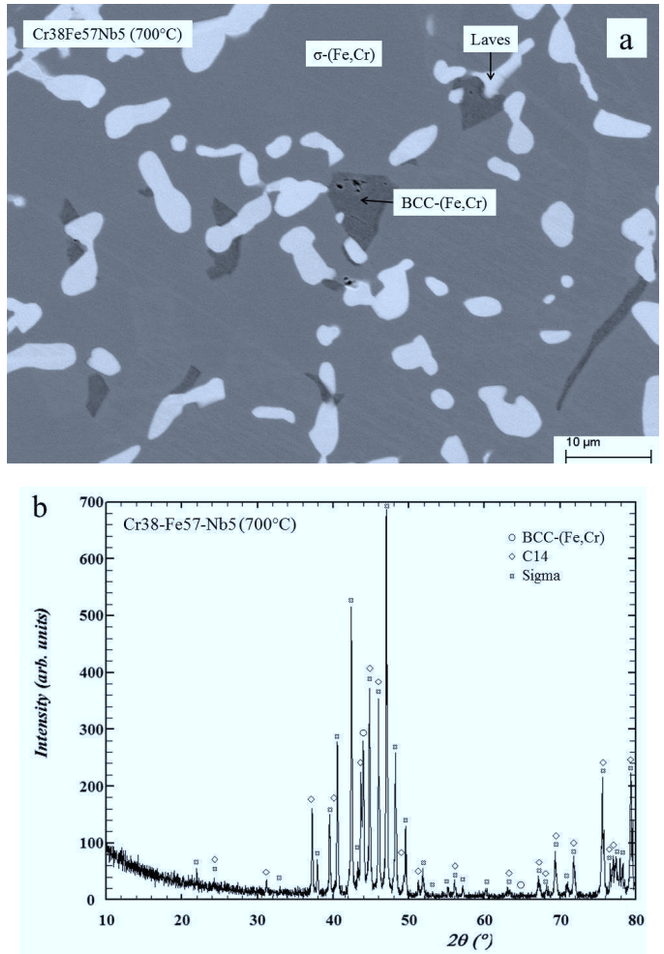

Figure 52 – Microstructure and XRD analysis of the three phase field C14+σ+BCC on the Fe-Cr-rich side at 700°C. a) SEM image of the microstructure of the sample 15 (Cr38Fe57Nb5) annealed at 700°C showing the three phase field equilibrium between BCC, σ and C14 Laves phase and b) XRD evaluation of the sample.

At high temperature (i.e. 1350°C), the Cr-Fe side of the phase diagram features by a continuous solid solution of BCC-(Cr,Fe) phase. At lower temperature (i.e. 1050°C) this phase is interrupted at low Cr content by the FCC γ [illegible] γ [illegible]

Conclusion

Three isothermal sections of the Cr-Fe-Nb phase equilibria were presented. This work highlighted the phase field region of the two different Laves phases as these intermetallic phases are of primary importance for the development of high temperature materials. It was not found that Nb dissolved in

Sample No.	nominal composition at.%	annealing	Phases	Space Group	XRD lattice parameters pm		Composition (EDX) Cr	Fe	Nb
								at.%	
Isothermal section 700°C									
15	Cr38Fe57Nb5	700°C, 108 d	(Fe,Cr)$_2$Nb	$P6_3/mmc$	a=483.0(4)	c=787.9(6)	17.5	55.1	27.5
			σ						
			bcc-(Fe,Cr)	Im-3m	a=288.4(4)		32.8	67.2	0.1
16	Cr36Fe54Nb10	700°C, 108 d	σ						
			(Fe,Cr)$_2$Nb	$P6_3/mmc$	a=482.9(6)	c=787.7(5)	20.0	52.7	27.3
17	Cr32Fe48Nb20	700°C, 108 d	bcc-(Fe,Cr)	Im-3m	a=287.8(7)		57.4	42.6	0.0
			(Fe,Cr)$_2$Nb	$P6_3/mmc$	a=484.3(0)	c=790.8(3)	21.6	49.6	28.8
18	Cr57Fe38Nb5	700°C, 108 d	bcc-(Fe,Cr)	Im-3m	a=292.3(6)		64.3	35.7	0.0
			(Fe,Cr)$_2$Nb	$P6_3/mmc$	a=484.5(1)	c=796.2(9)	25.5	46.8	27.8
19	Cr54Fe36Nb10	700°C, 108 d	bcc-(Fe,Cr)	Im-3m	a=296.7(5)		68.7	31.2	0.1
			(Fe,Cr)$_2$Nb	$P6_3/mmc$	a=477.9(3)	c=789.6(3)	26.5	45.3	28.2
20	Cr48Fe32Nb20	700°C, 108 d	bcc-(Fe,Cr)	Im-3m	a=288.1(4)		84.3	18.9	0.2
			(Fe,Cr)$_2$Nb	$P6_3/mmc$	a=486.5(5)	c=795.4(9)	36.2	33.9	29.9
30	Cr20Fe30Nb50	700°C, 108 d	(Fe,Cr)$_2$Nb	$P6_3/mmc$	a=489.1(4)	c=798.8(1)	26.9	38.5	34.7
			Fe_7Nb_6	R-3m	a=493.8(1)	c=2697.(8)	17.0	36.3	46.8
			(Nb)	Im-3m	a=329.6(2)		3.5	3.4	93.1

Table 33 - Results of the phase analysis by SEM/EDX and XRD of samples annealed at 700°C.

Sample No.	nominal composition at.%	annealing	Phases	Space Group	XRD lattice parameters pm		Composition (EDX) Cr	Fe at.%	Nb
Isothermal section 1050 °C									
1	Cr32Fe60Nb8	1050 °C, 28 d	bcc-(Fe,Cr)	Im-3m	a=287.7(2)		39.4	60.2	0.3
			(Fe,Cr)$_2$Nb	P6$_3$/mmc	a=483.4(2)	c=788.3(4)	17.1	54.4	27.6
3	Cr64Fe20Nb16	1050 °C, 28 d	bcc-(Fe,Cr)	Im-3m	a=288.7(2)		90.3	9.4	0.2
			(Fe,Cr)$_2$Nb	P6$_3$/mmc	a=489.0(3)	c=798.8(14)	38.1	30.8	31.1
4	Cr35.75Fe35Nb29.25	1050 °C, 28 d	bcc-(Fe,Cr)	Im-3m	a=288.5(8)		84.5	15.3	0.3
			(Fe,Cr)$_2$Nb	P6$_3$/mmc	a=487.1(1)	c=796.6(2)	33.7	35.9	30.4
5	Cr44Fe20Nb36	1050 °C, 28 d	(Fe,Cr)$_2$Nb	P6$_3$/mmc	a=491.4(1)	c=805.6(2)	45.4	20.3	34.2
			(Nb)	Im-3m	a=329.3(6)		6.1	1.6	92.2
6	Cr29.25Fe35Nb35.75	1050 °C, 28 d	(Fe,Cr)$_2$Nb	P6$_3$/mmc	a=489.4(1)	c=800.7(2)	30.4	35.2	34.4
			Phase T	Fd-3m	a=1132.4(5)		17.7	32.4	49.9
			(Nb)	Im-3m	a=329.4(4)		4.6	4.5	90.9
7	Cr36Fe20Nb44	1050 °C, 28 d	(Fe,Cr)$_2$Nb	P6$_3$/mmc	a=491.3(1)	c=804.5(2)	42.4	23.3	34.4
			(Nb)	Im-3m	a=329.7(2)		6.2	2.0	91.8
8	Cr10Fe35Nb55	1050 °C, 28 d	□-Fe$_7$Nb$_6$	R-3m	a=493.7(3)	c=2692(3)	12.9	39.9	47.3
			Phase T	Fd-3m	a=1130.4(5)		9.7	41.9	48.4
			(Nb)	Im-3m	a=329.3(2)		1.8	3.3	94.8
			(Fe,Cr)$_2$Nb	P6$_3$/mmc	a=487.3(7)	c=792(2)	Not found in EDX		
15	Cr38Fe57Nb5	1050°C, 34d	(Fe,Cr)$_2$Nb	P6$_3$/mmc	a=483.0	c=787	18.2	53.3	28.5
			bcc-(Fe,Cr)	Im-3m	a=287.8		42.6	57.1	0.3
16	Cr36Fe54Nb10	1050°C, 34d	(Fe,Cr)$_2$Nb	P6$_3$/mmc	a=4.835(1)	c=788.6(4)	18.5	53.3	28.2
			bcc-(Fe,Cr)	Im-3m	a=287.6(5)		45.2	54.5	0.3
21	Cr72Fe3Nb25	1050°C, 34d	bcc-(Fe,Cr)	Im-3m	a=288.6(2)		98.6	0.7	0.7
			(Fe,Cr)$_2$Nb	P6$_3$/mmc	a=492.2(1)	c=807.2(2)	Not found in EDX		
			Cr$_2$Nb	Fd-3m	a=697.8(1)		63.9	3.5	32.6

Sample No.	nominal composition at.%	annealing	Phases	Space Group	XRD lattice parameters pm		Composition (EDX) Cr	Fe	Nb
							at.%		
22	Cr69Fe6Nb25	1050°C, 34d	bcc-(Fe,Cr)	Im-3m	a=288.6(2)		97.6	1.5	0.9
			$(Fe,Cr)_2Nb$	$P6_3/mmc$	a=491.4(2)	c=806.2(5)	Not found in EDX		
			Cr_2Nb	Fd-3m	a=696.3(3)		61.2	6.4	32.4
23	Cr66Fe9Nb25	1050°C, 34d	bcc-(Fe,Cr)	Im-3m	a=288.5(4)		96.1	2.3	1.6
			$(Fe,Cr)_2Nb$	$P6_3/mmc$	a=491.5(7)	c=805.8(8)	57.7	10.1	32.2
24	Cr57Fe3Nb40	1050°C, 34d	(Nb)	Im-3m	a=328.3(1)		7.4	0.3	92.2
			$(Fe,Cr)_2Nb$	$P6_3/mmc$	a=493.8(2)	c=807.6(8)	Not found inEDX		
			Cr_2Nb	Fd-3m	a=698.6(8)		62.5	2.9	34.7
25	Cr54Fe6Nb40	1050°C, 34d	(Nb)	Im-3m	a=328.9(1)		7.5	0.7	91.8
			$(Fe,Cr)_2Nb$	$P6_3/mmc$	a=493.8(5)	c=807.6(1)	Not found in EDX		
			Cr_2Nb	Fd-3m	a=698.6(1)		59.0	6.3	34.7
26	Cr51Fe9Nb40	1050°C, 34d	(Nb)	Im-3m	a=328.8(0)		6.8	1.1	92.2
			$(Fe,Cr)_2Nb$	$P6_3/mmc$	a=493.2(1)	c=807.4(8)	56.3	9.3	34.4
			Cr_2Nb	Fd-3m	a=697.8(1)		Not found in EDX		
27	Cr5Fe48Nb47	1050°C, 34d	(Nb)	Im-3m	a=329.5(9)		1.0	6.3	92.7
			□-Fe_7Nb_6	R-3m	a=492.4	c=2679.2	4.7	47.9	47.4
			$(Fe,Cr)_2Nb$	$P6_3/mmc$	a=486.5(6)	c=792.3(9)	9.5	55.6	34.9
28	Cr14Fe34Nb55	1050°C, 34d	(Nb)	Im-3m	a=329.4(5)		2.3	3.4	94.3
			□-Fe_7Nb_6	R-3m	a=493.8(4)	c=2693.3	14.7	37.9	47.4
			$(Fe,Cr)_2Nb$	$P6_3/mmc$	a=488.9(9)	c=795.9(7)	24.8	40.1	35.1
			Phase T	Fd-3m	a=1131.1		Not found in EDX		
29	Cr5Fe40Nb55	1050°C, 34d	(Nb)	Im-3m	a=329.1(6)		1.0	5.3	93.7
			□-Fe_7Nb_6	R-3m	a=493.5(3)	c=2685.2(5)	5.8	45.6	48.6
30	Cr20Fe30Nb50	1050°C, 37d	(Nb)	Im-3m	a=329.4		2.9	2.9	94.2
			□-Fe_7Nb_6	R-3m	a=493.7	c=2695.(4)	16.2	36.3	47.5
			$(Fe,Cr)_2Nb$	$P6_3/mmc$	a=489.3	c=799.5(4)	26.2	37.9	35.9

Sample No.	nominal composition at. %	annealing	Phases	Space Group	XRD lattice parameters pm		Composition (EDX) Cr	Fe at.%	Nb
31	Cr10Fe50Nb40	1050°C, 34d	□-Fe_7Nb_6	R-3m	a=492.5(8)	c=2681.0(4)	6.8	46.0	47.2
			$(Fe,Cr)_2Nb$	$P6_3/mmc$	a=487.2(5)	c=793.7(7)	12.3	53.0	34.7
32	Cr15Fe45Nb40	1050°C, 34d	□-Fe_7Nb_6	R-3m	a=492.99	c=2686.1(0)	10.8	41.9	47.3
			$(Fe,Cr)_2Nb$	$P6_3/mmc$	a=487.9(1)	c=795.9(8)	17.8	46.9	35.3
33	Cr20Fe40Nb40	1050°C, 34d	(Nb)	Im-3m	a=329.0(6)		3.2	5.1	91.8
			□-Fe_7Nb_6	R-3m	a=493.5(8)	c=2693.1(5)	14.1	38.8	47.1
			$(Fe,Cr)_2Nb$	$P6_3/mmc$	a=488.7(4)	c=798.3(1)	23.0	42.1	35.0
34	Cr15Fe37Nb48	1050°C, 34d	(Nb)	Im-3m	a=329.2(3)		2.4	4.2	93.4
			□-Fe_7Nb_6	R-3m	a=493.8(3)	c=2693.(2)	13.6	38.9	47.4
			$(Fe,Cr)_2Nb$	$P6_3/mmc$	a=489.1(4)	c=798.9(11)	22.7	42.2	35.1
			Phase T	Fd-3m	a=1130.6(6)		Not found in EDX		
35	Cr45Fe15Nb40	1050°C, 35d	$(Fe,Cr)_2Nb$	$P6_3/mmc$	a=491.9(9)	c=806.8(6)	49.5	16.3	34.2
			(Nb)	Im-3m	a=329.3(9)		6.5	1.3	92.2
36	Cr35Fe25Nb40	1050°C, 35d	$(Fe,Cr)_2Nb$	$P6_3/mmc$	a=490.5(6)	c=803.4(9)	38.4	27.2	34.4
			(Nb)	Im-3m	a=329.4(4)		6.3	2.8	90.9
37	Cr27Fe33Nb40	1050°C, 35d	$(Fe,Cr)_2Nb$	$P6_3/mmc$	a=489.5(8)	c=800.7(6)	29.5	36.2	34.3
			(Nb)	Im-3m	a=329.5(4)		4.2	3.1	92.7
			Phase T	Fd-3m	a=1132.9(8)		Not found in SEM		
38	Cr63Fe12Nb25	1050°C, 35d	$(Fe,Cr)_2Nb$	$P6_3/mmc$	a=491.1(4)	c=805.6(4)	54.7	13.2	32.1
			(Nb)	Im-3m	a=288.6(4)		95.3	3.5	1.2
39	Cr55Fe20Nb25	1050°C, 35d	$(Fe,Cr)_2Nb$	$P6_3/mmc$	a=489.2(5)	c=801.5(9)	44.8	23.5	31.6
			bcc-(Fe,Cr)	Im-3m	a=288.5(9)		93.1	6.3	0.6
40	Cr45Fe30Nb25	1050°C, 35d	$(Fe,Cr)_2Nb$	$P6_3/mmc$	a=487.6(5)	c=797.5(9)	35.0	34.4	30.6
			bcc-(Fe,Cr)	Im-3m	a=288.4(9)		87.4	12.3	0.3

Sample No.	nominal composition at. %	annealing	Phases	Space Group	XRD lattice parameters pm		Composition (EDX) Cr	Fe at.%	Nb
41	Cr35Fe40Nb25	1050°C, 35d	$(Fe,Cr)_2Nb$	$P6_3/mmc$	a=485.7(7)	c=793.6(4)	27.2	43.3	29.6
			bcc-(Fe,Cr)	Im-3m	a=287.8(9)		73.5	26.3	0.3
42	Cr25Fe50Nb25	1050°C, 35d	$(Fe,Cr)_2Nb$	$P6_3/mmc$	a=484.1(8)	c=790.7(5)	20.8	50.6	28.6
			bcc-(Fe,Cr)	Im-3m	a=287.8(9)		52.7	47.0	0.3
43	Cr15Fe60Nb25	1050°C, 35d	$(Fe,Cr)_2Nb$	$P6_3/mmc$	a=482.7(6)	c=787.6(3)	12.9	59.3	27.8
			bcc-(Fe,Cr)	Im-3m	a=287.6(3)		29.4	70.4	0.4
44	Cr5Fe70Nb25	1050°C 35d	$(Fe,Cr)_2Nb$	$P6_3/mmc$	a=481.8(7)	c=785.7(5)	4.5	67.9	27.6
			bcc-(Fe,Cr)	Im-3m	a=287.0(4)		32.3	91.3	0.5
45	Cr56Fe4Nb40	1050°C 35d	Cr_2Nb	Fd-3m	a=698.9(2)		61.7	4.2	34.1
			$(Fe,Cr)_2Nb$	$P6_3/mmc$	a=494.2(1)	c=808.3(6)	60.2	4.7	35.0
			(Nb)	Im-3m	a=329.2(7)		15.9	1.1	83.0
46	Cr55Fe5Nb40	1050°C 35d	Cr_2Nb	Fd-3m	a=698.82(2)		60.4	5.6	34.1
			$(Fe,Cr)_2Nb$	$P6_3/mmc$	a=493.9(9)	c=807.8(8)	59.5	6.3	34.2
			(Nb)	Im-3m	a=329.2(8)		2.1	0.0	97.9
47	Cr53Fe7Nb40	1050°C 35d	Cr_2Nb	Fd-3m	a=697.5(2)		58.8	7.1	34.2
			$(Fe,Cr)_2Nb$	$P6_3/mmc$	a=492.5(2)	c=806.1(4)	56.4	8.7	34.9
			(Nb)	Im-3m	a=288.6(8)		2.2	0.4	97.4
48	Cr71Fe4Nb25	1050°C 35d	Cr_2Nb	Fd-3m	a=697.2(6)		63.6	4.4	32.0
			$(Fe,Cr)_2Nb$	$P6_3/mmc$	a=493.4(3)	c=807.2(6)	62.6	5.9	31.5
			bcc-(Fe,Cr)	Im-3m	a=297.6(9)		97.9	1.2	0.9
49	Cr70Fe5Nb25	1050°C 35d	Cr_2Nb	Fd-3m	a=696.8(4)		62.7	5.1	32.2
			$(Fe,Cr)_2Nb$	$P6_3/mmc$	a=491.5(8)	c=804.5(5)	60.7	7.1	32.2
			bcc-(Fe,Cr)	Im-3m	a=288.4(7)		95.1	1.6	3.2

Table 34 –Experimental results of the phase analysis of samples annealed at 1050°C.

Sample No.	nominal composition at.%	annealing	Phases	Space Group	XRD lattice parameters (pm)	Composition (EDX) Cr	Fe	Nb
						at.%		
Isothermal section 1350°C								
1	Cr32Fe60Nb8	1350 °C, 5 d	bcc-(Fe,Cr) $(Fe,Cr)_2Nb$	Im-3m $P6_3/mmc$	a=288.1(2) a=482.9(2) c=787.6(2)	37.4 19.5	61.3 53.8	1.3 26.7
2	Cr48Fe40Nb12	1350 °C, 5 d	bcc-(Fe,Cr) $(Fe,Cr)_2Nb$	Im-3m $P6_3/mmc$	a=288.3(2) a=485.1(3) c=791.7(3)	59.4 29.5	39.7 42.9	0.9 27.6
3	Cr64Fe20Nb16	1350 °C, 5 d	bcc-(Fe,Cr) $(Fe,Cr)_2Nb$	Im-3m $P6_3/mmc$	a=288.7(2) a=488.5(2) c=799.1(6)	85.0 44.6	14.0 25.6	1.0 29.8
4	Cr35.75Fe35Nb29.25	1350 °C, 5d	$(Fe,Cr)_2Nb$	$P6_3/mmc$	a=486.5(1) c=795.3(1)	35.5	35.7	28.8
5	Cr44Fe20Nb36	1350 °C 5 d	$(Fe,Cr)_2Nb$ (Nb)	$P6_3/mmc$ Im-3m	a=492.7(1) c=807.2(2) not found in XRD	44.1 8.6	19.9 2.7	36.0 88.7
6	Cr29.25Fe35Nb35.75	1350 °C, 5d	$(Fe,Cr)_2Nb$	$P6_3/mmc$	a=490.2(1) c=802.2(2)	29.5	34.9	35.5
7	Cr36Fe20Nb44	1350 °C, 5 d	$(Fe,Cr)_2Nb$ (Nb)	$P6_3/mmc$ Im-3m	a=492.7(2) c=806.9(5) a=327.2(2)	41.3 7.7	22.7 2.7	36.0 89.6
9	Cr10Fe56.67Nb33.33	1350 °C, 6d	$(Fe,Cr)_2Nb$	$P6_3/mmc$	- -	10.2	56.2	33.7
10	Cr20Fe46.67Nb33.33	1350 °C, 6d	$(Fe,Cr)_2Nb$	$P6_3/mmc$	- -	20.2	46.1	33.7
11	Cr30Fe36.67Nb33.33	1350 °C, 6d	$(Fe,Cr)_2Nb$	$P6_3/mmc$	- -	30.4	36.3	33.3
12	Cr40Fe26.67Nb33.33	1350 °C, 6d	$(Fe,Cr)_2Nb$	$P6_3/mmc$	- -	39.9	26.5	33.6
13	Cr50Fe16.67Nb33.33	1350 °C, 6d	$(Fe,Cr)_2Nb$	$P6_3/mmc$	- -	49.7	16.7	33.6
14	Cr60Fe6.67Nb33.33	1350 °C, 6d	$(Fe,Cr)_2Nb$	$P6_3/mmc$	- -	59.8	6.6	33.6
21	Cr72Fe3Nb25	1350°C, 10d	Cr_2Nb (Cr)	Fd-3m Im-3m	a=696.2(9) a=288.5(1)	64.8 97.5	3.3 1.2	32.0 1.4

Sample No.	nominal composition at.%	annealing	Phases	Space Group	XRD lattice parameters (pm)		Composition (EDX) Cr	Fe	Nb
								at.%	
22	Cr69Fe6Nb25	1350°C, 10d	$(Fe,Cr)_2Nb$	$P6_3/mmc$	a=491.0(4)	c=806.0(1)	61.4	6.8	31.8
			(Cr)	Im-3m	a=288.8(7)		96.2	2.5	1.4
23	Cr66Fe9Nb25	1350°C, 10d	$(Fe,Cr)_2Nb$	$P6_3/mmc$	a=491.2(4)	c=805.7(9)	58.0	10.6	31.4
			bcc-(Fe,Cr)	Im-3m	a=288.9(5)		94.6	3.7	1.4
24	Cr57Fe3Nb40	1350°C, 10d	Cr_2Nb	Fd-3m	a=700.8(1)		60.7	3.3	36.1
			(Nb)	Im-3m	a=326.8(9)		10.5	0.5	89
25	Cr54Fe6Nb40	1350°C, 10d	$(Fe,Cr)_2Nb$	$P6_3/mmc$	a=494.9(4)	c=809.2(3)	58	6.3	35.7
			Cr_2Nb	Fd-3m	a=700.0(2)				
			(Nb)	Im-3m	a=326.8(5)		10.6	1	88.4
26	Cr51Fe9Nb40	1350°C, 10d	$(Fe,Cr)_2Nb$	$P6_3/mmc$	a=493.8(2)	c=810.2(9)	54.3	9.8	35.9
			Nb	Im-3m	a=326.7(8)		11	1.4	87.7
27	Cr5Fe48Nb47	1350°C, 10d	□-Fe_7Nb_6	R-3m	a=492.7(7)	c=2681.6(1)	5	47.6	47.3
			$(Fe,Cr)_2Nb$	$P6_3/mmc$	a=497.7(9)	c=7.912(2)	8	55.8	36.3
28	Cr14Fe34Nb55	1350°C, 10d	□-Fe_7Nb_6	R-3m	a=494.4(9)	c=2698.0(0)	15.1	37.1	47.9
			(Nb)	Im-3m	a=327.2(2)		3.6	5.1	91.3
					Not found		21.7	41	37.3
29	Cr5Fe40Nb55	1350°C, 10d	□-Fe_7Nb_6	R-3m	a=494.4(8)	c=2688.9(7)	5.5	44.3	50.2
			(Nb)	Im-3m	a=327.4(7)		1.2	6.2	92.6
31	Cr10Fe50Nb40	1350°C, 10d	□-Fe_7Nb_6	R-3m	a=493.2(7)	c=2686.1(8)	7.1	45.4	47.5
			$(Fe,Cr)_2Nb$	$P6_3/mmc$	a=488.8(2)	c=797.2	11.3	52.3	36.3
32	Cr15Fe45Nb40	1350°C, 10d	□-Fe_7Nb_6	R-3m	a=493.6(8)	c=2690.4(6)	11	41	48
			$(Fe,Cr)_2Nb$	$P6_3/mmc$	a=489.5(2)	c=798.8(9)	16.7	46.6	36.8
33	Cr20Fe40Nb40	1350°C, 10d	□-Fe_7Nb_6	R-3m	a=494.2(5)	c=2697.5(4)	14.8	37.1	48.1
			$(Fe,Cr)_2Nb$	$P6_3/mmc$	a=490.3(5)	c=800.8(4)	22	41.3	36.8

Sample No.	nominal composition at.%	annealing	Phases	Space Group	XRD lattice parameters (pm)		Composition (EDX) Cr	Fe	Nb
								at.%	
34	Cr15Fe37Nb48	1350°C, 10d	□-Fe_7Nb_6	R-3m	a=494.4(6)	c=2697.4(5)	14.6	37	48.4
			$(Fe,Cr)_2Nb$	$P6_3/mmc$	a=490.4(7)	c=801.1(3)	21.7	41.2	37.1
			(Nb)	Im-3m	a=327.7		3.6	5.5	91.1
35	Cr45Fe15Nb40	1350°C, 13d	$(Fe,Cr)_2Nb$	$P6_3/mmc$	a=492.9(3)	c=808.2(7)	47.8	16.4	35.7
			(Nb)	Im-3m	a=326.7(7)		9.1	2.1	88.8
36	Cr35Fe25Nb40	1350°C, 13d	$(Fe,Cr)_2Nb$	$P6_3/mmc$	a=491.8(5)	c=805.3(5)	37.4	26.4	36.2
			(Nb)	Im-3m	a=327.1(7)		6.9	3.4	89.6
37	Cr27Fe33Nb40	1350°C, 13d	$(Fe,Cr)_2Nb$	$P6_3/mmc$	a=491.2(4)	c=803.2(7)	28.3	35.0	36.7
			(Nb)	Im-3m	a=327.3		5.1	4.5	90.4
38	Cr63Fe12Nb25	1350°C, 13d	$(Fe,Cr)_2Nb$	$P6_3/mmc$	a=490.4(2)	c=803.9(7)	54.4	14.1	31.5
			(Cr)	Im-3m	a=288.7(7)		93.3	5.4	1.3
39	Cr55Fe20Nb25	1350°C, 13d	$(Fe,Cr)_2Nb$	$P6_3/mmc$	a=489.0(9)	c=801.2(9)	47.4	21.8	30.8
			bcc-(Fe,Cr)	Im-3m	a=288.9(5)		88.3	10.5	1.2
40	Cr45Fe30Nb25	1350°C, 13d	$(Fe,Cr)_2Nb$	$P6_3/mmc$	a=487.1	c=797.1(3)	38.9	31.7	29.4
			bcc-(Fe,Cr)	Im-3m	a=288.5(8)		77.7	21.3	1.1
41	Cr35Fe40Nb25	1350°C, 13d	$(Fe,Cr)_2Nb$	$P6_3/mmc$	a=485.5(8)	c=792.4(7)	31.1	40.8	28.1
			bcc-(Fe,Cr)	Im-3m	a=288.6(6)		62.3	36.4	1.3
42	Cr25Fe50Nb25	1350°C, 13d	$(Fe,Cr)_2Nb$	$P6_3/mmc$	a=483.3(6)	c=788.6(2)	23.0	49.7	27.3
			bcc-(Fe,Cr)	Im-3m	a=295.6(2)		44.6	54.2	1.2
43	Cr15Fe60Nb25	1350°C, 13d	$(Fe,Cr)_2Nb$	$P6_3/mmc$	a=482.1(6)	c=786.4(1)	13.7	59.4	26.9
			bcc-(Fe,Cr)	Im-3m	a=292.6(3)		25.5	73.0	1.5
44	Cr5Fe70Nb25	1350°C, 13d	$(Fe,Cr)_2Nb$	$P6_3/mmc$	a=482.0(6)	c=786.2(6)	4.5	68.8	26.6
					Too small to be quantify		8.1	90.1	1.8
45	Cr56Fe4Nb40	1350°C, 13d	Cr_2Nb	Fd-3m	a=700.3(6)		59.7	4.4	35.9
			(Nb)	Im-3m	a=326.9(1)		11.4	0.6	87.9

Sample No.	nominal composition at.%	annealing	Phases	Space Group	XRD lattice parameters (pm)		Composition (EDX) Cr	Fe	Nb
								at.%	
46	Cr55Fe5Nb40	1350°C, 13d	$(Fe,Cr)_2Nb$	$P6_3/mmc$	a=495.1	c=809.2(1)	58.3	6.0	35.7
			Cr_2Nb	Fd-3m	a=700.1(7)				
			(Nb)	Im-3m	a=326.7(8)		11.2	0.9	87.9
47	Cr53Fe7Nb40	1350°C, 13d	$(Fe,Cr)_2Nb$	$P6_3/mmc$	a=494.6(5)	c=809.7(9)	56.5	7.7	35.8
			C36	$P6_3/mmc$	a=497.7(8)	c=1619.5(6)			
			(Nb)	Im-3m	a=326.8(6)		11.1	1.1	87.8
48	Cr71Fe4Nb25	1350°C, 13d	$(Fe,Cr)_2Nb$	$P6_3/mmc$	a=493.2(3)	c=806.0(6)			
			Cr_2Nb	Fd-3m	a=697.5(2)		62.4	4.8	32.9
			(Cr)	Im-3m	a=289.1(6)		96.6	1.8	1.6
49	Cr70Fe5Nb25	1350°C, 13d	$(Fe,Cr)_2Nb$	$P6_3/mmc$	a=492.6(7)	c=805.8(3)	62.0	5.8	32.1
			Cr_2Nb	Fd-3m	a=697.1(1)				
			(Cr)	Im-3m	a=289.0(9)		96.4	2.2	1.5

Table 35 – Results of the analysis by SEM/EDX and XRD of the samples annealed at 1350°C.

II. Thermal and solidification behavior of the Cr-Fe-Nb system

Thermal analysis and determination of characteristic temperatures have not been carried out so far in this system and no liquidus projection is available in the literature. The invariant reactions of the limiting binary systems are given in *Table 36. Nevertheless the liquidus projection of phase equilibria is rather important for the understanding of the liquid-solid phase changes. In addition, in the thermodynamic optimization of phase diagram (i.e. Calphad method), the invariant reactions data are taken with a higher priority for the determination of the thermodynamic parameters of the considered system.*

Reactions	Type	Temperature (°C)	References
Nb-Cr			
L=NbCr$_2$	**C**	**1727□2**	**[18]**
L=C15□Nb	**e1**	**1681□2**	**[18]**
L=C15□Cr	**e2**	**1660□2**	**[18]**
Fe-Nb			
L□C14=□	**p1**	**1523□2**	**[35]**
L=Nb□	**e4**	**1508□2**	**[35]**
L=bcc-Fe□C14	**e3**	**1373□2**	**[35]**
Fe-Cr			
L = bcc	**C**	**1515.7**	**[24]**
fcc = bcc	**C**	**853.3**	**[24]**
bcc = σ			
σ□□ □□□	□□□□□ □	□□ □□□□	□ □□□ □□

Table 36 – Invariant reactions in the binary boundary systems of the Cr-Fe-Nb phase diagram.

The present work aims to investigate the solidification behavior of the system as well as the liquidus projection.

The samples have been prepared as explained in the previous part (see p. 109). For the study of the solidification behavior, the microstructures of the as-cast samples were studied by SEM.

The DTA measurements have been done on a Setsys Evolution using alumina crucibles with a heating rate of 5°C/min. However, some problems have been encountered using alumina crucibles as they are not stable at high temperature. New crucibles to carry out the DTA measurements were therefore necessary for the investigation of the temperature dependence of the samples.

1. Results

The nominal compositions as well as the results of the phase analysis after alloying of the as-cast samples are summarized in *Table 38*. The composition and the primary crystallization of the as-cast samples are given in *Figure 53*.

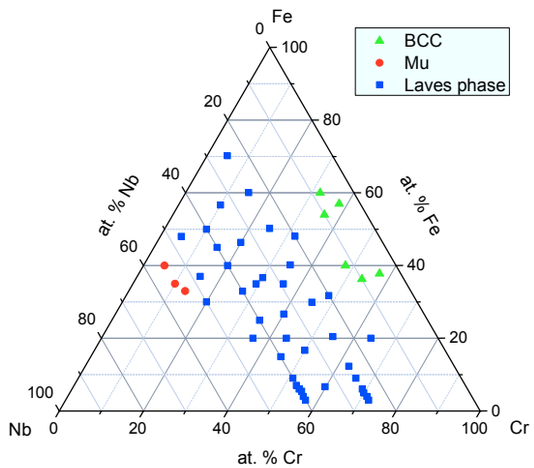

Figure 53 – Compositions and primary crystallization of the as-cast samples.

As shown by the isothermal sections presented in the previous chapter, the Cr-Fe-Nb phase diagram does not contain ternary compounds but instead a high solubility of a third element in the different binary compounds (except for σ phase which has no perceptible solubility of Nb according to the results obtained at 700°C).

The presented primary crystallizations of the as-cast samples as well as the binary invariant reactions (from literature, see *Table 36*) were used to construct the liquidus projection (*Figure 55*). The compositions of the ternary invariant reactions and their types (i.e. type I-Eutectic, type II-U, type III-Peritectic) have to be consistent with the data obtained for the isothermal sections:

- At the eutectic point which is a local minimum, the liquid is in equilibrium with three solid phases, C14 + BCC + μ. The eutectic point must lie within the three phase field as shown in the scheme below;

Sketch of a E type reaction: L ↔ μ + C14 + (Nb)

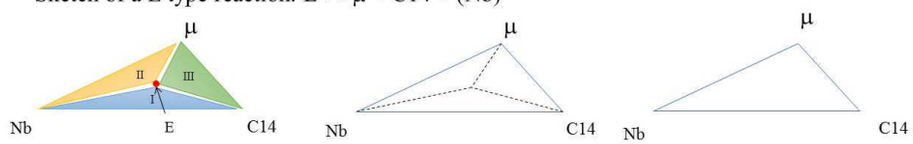

- In a U type reaction, liquid and one solid phase are in equilibrium with two other solids, so the composition of this point cannot be in the three phase equilibrium as seen as sketched below.

Sketch of a U type reaction: L+C15↔C14+(Nb)

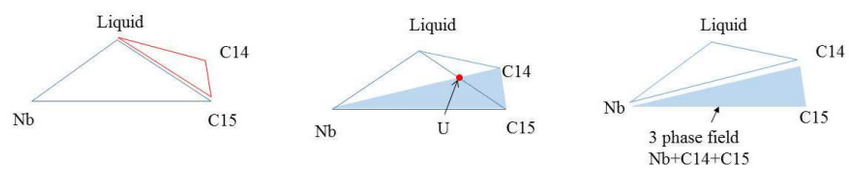

The invariant reaction types were determined from the study of the microstructure of the as-cast samples by SEM. Following the sketches of the different types of the invariant reactions, the three phase field (C14 + μ + Nb) of the different isothermal sections have been superposed for the determination of the eutectic point. In the same way, following the sketch of the U-type reaction, their respective places were determined.

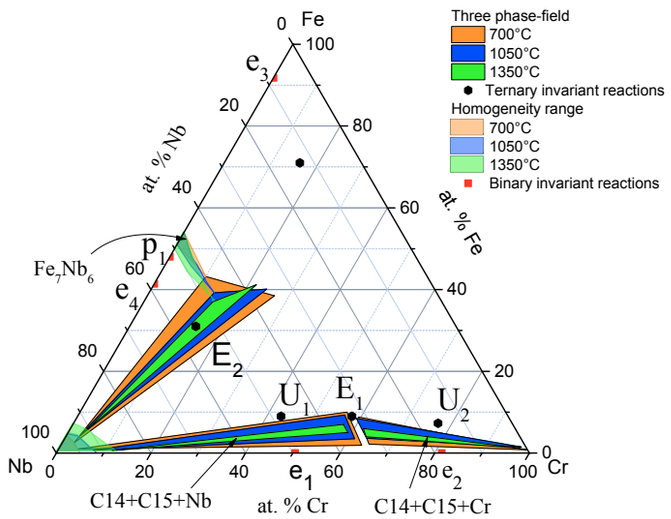

Figure 54 - Superposition of the three phase fields obtained from the studied of the isothermal sections as given in Figure 43, Figure 44 and Figure 45 as well as the binary invariant reactions as a guide to place the ternary invariant reactions in consistency with the isothermal sections.

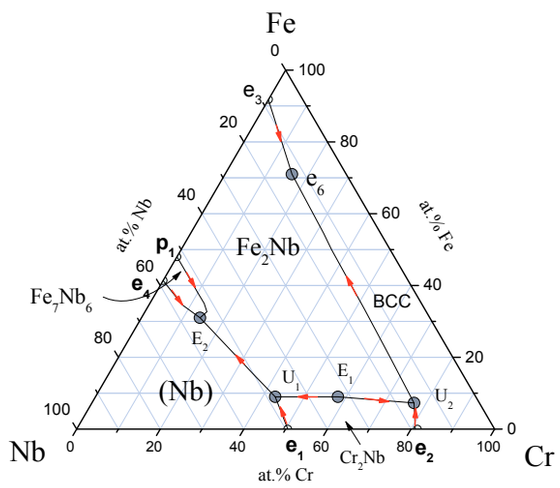

Figure 55 – Liquidus projection of the Cr-Fe-Nb system.

Table 37, where preliminary DTA measurements allowed the determination of their respective temperature. Nevertheless, further measurements are necessary for a better accuracy of these data.

Reactions		**Type**		**Temperature (°C)**
L ↔ □		**E1**		**unknown**
L □ C15 ↔ □ □		**1□**		**1637**
L □ C15 ↔ □ □ □		□ □ □		□ □
↔ □□ □ □	□	□		
↔ □ □ □ □		□	□	

Table 37 – Invariant reaction in the ternary Cr-Fe-Nb system.

2. Discussion

2.1 <u>Cr-Nb side</u>

The Cr-Nb phase diagram exhibits two eutectic invariant reactions as shown by Stein et al. □1□□(see Fig. 1 of the original paper) around the C15 Laves phase. This phase extends into the ternary phase diagram with a dissolution of Fe into it until a change of Laves phase polytype to C14 occurs. The change of Laves phase polytypes is characterized by the presence of a two phase field region which becomes narrower as the temperature is high (see isothermal section at 1050 and 1350C)*, Figure 44 and Figure 45). The microstructures of as-cast samples on each side of this two phase field region containing 9 at. % of Fe are shown in Figure 56 and Figure 57. These two samples are composed of primary crystallized C14 Laves phase surrounded by a fine microstructure (Laves phase + BCC) characteristic of an eutectic.*

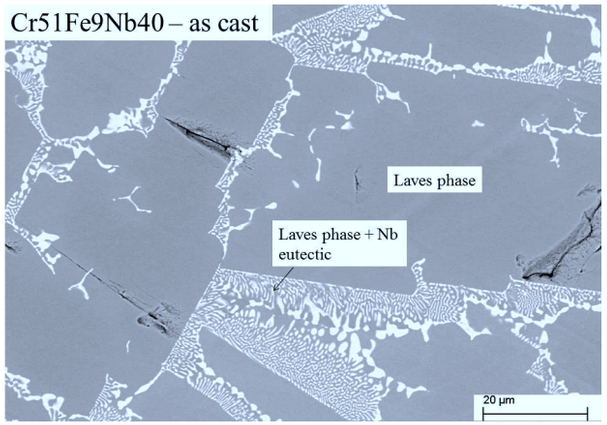

Figure 56 - As cast microstructure of the sample 26 - Cr51Fe9Nb40 with primary crystallized the Laves phase (dark) and (Nb)+C14 eutectic.

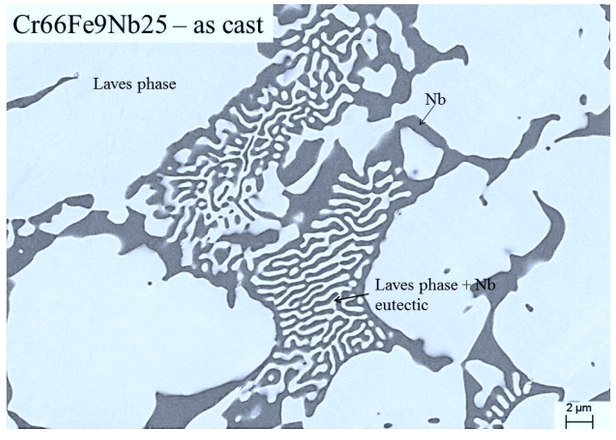

Figure 57 - As cast microstructure of the sample 23 – Cr66Fe9Nb25 with the primary crystallized Laves phase (light) and C14+ (Cr) in eutectic.

The ternary system is characterized by two U type reactions on each side of the C14-C15 Laves phase. The two invariant reaction points are symbolized as U_1 and U_2 on the liquidus projection (Figure 55), U_1 (L + C15 ↔ □ □□ ↔ □ □

1.1. Fe-Nb side

In the Fe-Nb system, there are two invariant reactions surrounding the [illegible] ↔ μ [illegible] μ [illegible] ↔ μ [illegible] *Figure 58) named* E_2 *in the liquidus projection (Figure 55), forming a local minimum on this part of the phase diagram.*

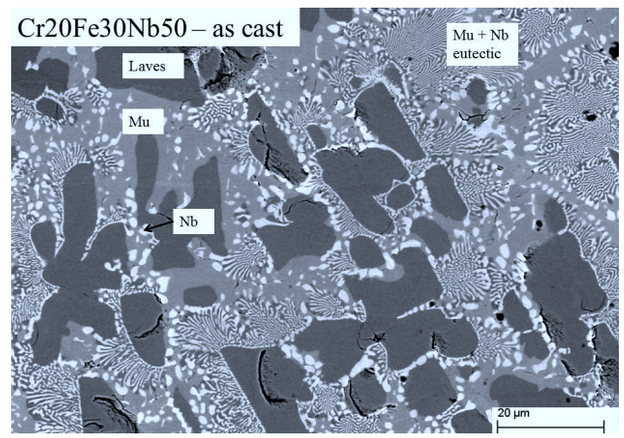

Figure 58 – SEM micrograph of cast sample 30 (Cr20Fe30Nb50), C14 Laves phase being the primary crystallization surrounded by an eutectic microstructure formed by μ and Nb.

1.2. Cr-Fe side

The Cr-Fe side is characterized by BCC primary crystallization (see *Figure 53). The positions of our different samples allow the determination of a liquidus valley in this region (around 17 at. % Nb). The evaluation of the microstructure of the as-cast sample 15 revealed a fine eutectic microstructure (C14+BCC) with BCC as primary crystallization (Figure 59). A local minimum exists in the liquidus valley, which is named* e_6 *on the liquidus projection (Figure 55).*

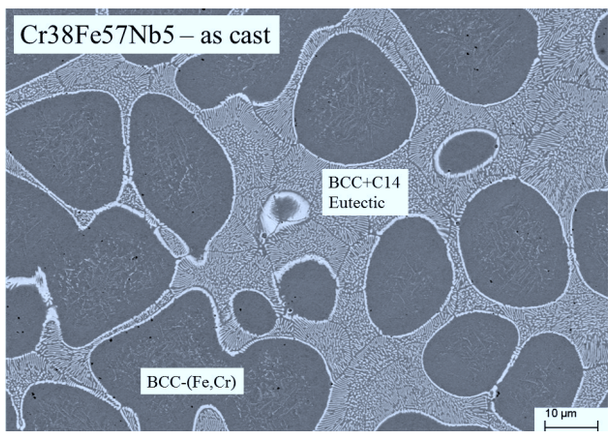

Figure 59 – SEM image of the microstructure of the sample 15 (Cr38Fe57Nb5) as cast showing BCC as primary crystallization and a eutectic microstructure (C14+BCC).

1.3. Ternary invariant reaction

Along two different isopleths with 25 and 40 at. Nb, several samples have been placed in order to construct vertical sections. The DTA measurements of these samples are ongoing and will allow to obtain the temperature of solidus and liquidus as function of the composition. With this, temperatures and compositions of the invariant reactions will be determined with better accuracy. Nevertheless, DTA measurements have been done for a couple of samples allowing an estimation of the temperature of the invariant reactions (given in *italic) in the reaction scheme Figure 60. These data should be considered preliminary results and are subject of changes with the investigation of the isopleths.*

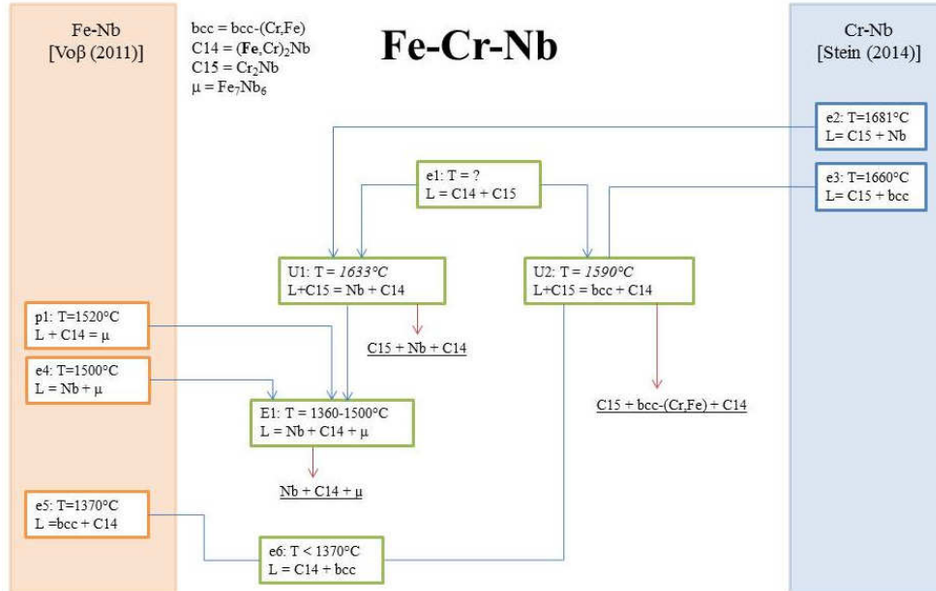

Figure 60 - Reaction scheme of the Cr-Fe-Nb phase equilibria without taking into account the Cr-Fe side. The data for the binary Cr-Nb and Fe-Nb and were taken from Stein et al. [18] *and Voss et al.* [35]*, respectively.*

Conclusion

Using data on primary crystallization and the knowledge of the invariant reactions in the binary system, the liquidus surface of the Cr-Fe-Nb system has been constructed. Further DTA measurements are necessary for the determination of the temperature of the invariant reactions and for the determination of the U type compositions (obtained from the isopleth).

Sample	nominal composition at.%	annealing	Phases		Space Group	XRD lattice parameters pm		EDX results Cr	Fe at.%	Nb
as cast series; * = primary crystallization										
1	Cr32Fe60Nb8	as cast	$(Fe,Cr)_2Nb$	*	$P6_3/mmc$	a=483.4(3)	c=788.3(7)	35.9	36.4	27.7
			bcc-(Fe,Cr)		Im-3m	a=288.0(2)		61.2	37.7	1.1
			unknown phase					38.6	44.3	17.1
2	Cr48Fe40Nb12	as cast	$(Fe,Cr)_2Nb$		$P6_3/mmc$	a=485.1(3)	c=792.9(6)	21.3	52.3	26.4
			bcc-(Fe,Cr)	*	Im-3m	a=288.2(2)		37.6	61.6	0.8
3	Cr64Fe20Nb16	as cast	$(Fe,Cr)_2Nb$	*	$P6_3/mmc$	a=488.6(4)	c=800.7(6)	50.0	20.8	29.3
			bcc-(Fe,Cr)		Im-3m	a=288.9(2)		80.3	17.9	1.8
4	Cr35.75Fe35Nb29.25	as cast	$(Fe,Cr)_2Nb$	*	$P6_3/mmc$	a=487.2(2)	c=797.1(3)	33.9	35.8	30.2
			bcc-(Fe,Cr)		Im-3m			58.7	40.2	1.0
5	Cr44Fe20Nb36	as cast	$(Fe,Cr)_2Nb$	*	$P6_3/mmc$	a=491.9(2)	c=806.1(3)	11.7	3.2	85.0
			(Nb)		Im-3m	a=328.5(7)		45.1	19.8	35.1
6	Cr29.25Fe35Nb35.75	as cast	$(Fe,Cr)_2Nb$	*	$P6_3/mmc$	a=490.1(2)	c=801.0(4)	30.1	35.0	34.8
			(Nb)		Im-3m	a=328.5(7)		5.8	5.2	89.1
7	Cr36Fe20Nb44	as cast	$(Fe,Cr)_2Nb$	*	$P6_3/mmc$	a=493.9(2)	c=809.0(3)	42.5	20.8	36.8
			$(Fe,Cr)_2Nb$		$P6_3/mmc$	In eutectic		34.2	27.6	38.2
			(Nb)		Im-3m	a=326.9(2)		9.2	6.1	84.7
8	Cr10Fe35Nb55	as cast	Phase T (η							
			Fe_7Nb_6	*	R-3m	a=495.5(4)	c=2699(2)	8.5	40.9	50.5
			(Nb)		Im-3m	a=329.3(4)		2.5	8.9	88.6
9	Cr10Fe56.67Nb33.33	as cast	$(Fe,Cr)_2Nb$	*	$P6_3/mmc$	a=485.7(1)	c=792.5(2)	10.4	56.3	33.3
			Fe_7Nb_6		R-3m	not found		5.8	36.6	42.7

Sample	nominal composition at.%	annealing	Phases		Space Group	XRD lattice parameters pm		EDX results Cr	Fe at.%	Nb
10	Cr20Fe46.67Nb33.33	as cast	(Fe,Cr)$_2$Nb	*	$P6_3/mmc$	a=487.2(1)	c=795.8(2)	20.4	46.0	33.6
			□-Fe_7Nb_6		R-3m	not found		9.6	32.3	44.0
11	Cr30Fe36.67Nb33.33	as cast	(Fe,Cr)$_2$Nb	*	$P6_3/mmc$	a=488.2(1)	c=798.7(2)	30.2	36.6	33.1
			Nb-oxide traces			not found				
12	Cr40Fe26.67Nb33.33	as cast	(Fe,Cr)$_2$Nb	*	$P6_3/mmc$	a=490.2(1)	c=802.8(2)	40.0	26.2	33.8
			Nb-oxide traces			not found				
13	Cr50Fe16.67Nb33.33	as cast	(Fe,Cr)$_2$Nb	*	$P6_3/mmc$	a=491.3(1)	c=805.9(2)	50.2	16.2	33.6
			Nb-oxide traces			not found				
14	Cr60Fe6.67Nb33.33	as cast	(Fe,Cr)$_2$Nb	*	$P6_3/mmc$	a=493.0(1)	c=809.2(2)	59.7	6.7	33.7
			bcc-(Fe,Cr)		Im-3m	not found		83.6	8.5	8.0
15	Cr38Fe57Nb5	as cast	bcc-(Fe,Cr)	*	Im-3m	a=288.1(2)		41.9	57.3	0.8
			(Fe,Cr)$_2$Nb		$P6_3/mmc$	a=483.5(3)	c=797.2(40)	Too small to be quantified		
16	Cr36Fe54Nb10	as cast	(Fe,Cr)$_2$Nb	*	$P6_3/mmc$	a=484.1(3)	c=790.0(7)	25.4	47.4	27.2
			bcc-(Fe,Cr)		Im-3m	a=288.0(2)		41.3	58.0	0.8
17	Cr32Fe48Nb20	as cast	(Fe,Cr)$_2$Nb	*	$P6_3/mmc$	a=485.0(3)	c=792.4(7)	26.3	41.6	32.1
			bcc-(Fe,Cr)		Im-3m	a=288.0		45.7	53.8	0.5
18	Cr57Fe38Nb5	as cast	(Fe,Cr)$_2$Nb		$P6_3/mmc$	a=484.7	c=793.1	33.4	41.4	25.2
			bcc-(Fe,Cr)	*	Im-3m	a=288.6		62.7	36.2	1.2
19	Cr54Fe36Nb10	as cast	(Fe,Cr)$_2$Nb		$P6_3/mmc$	a=487.1	c=797.8	36.7	34.3	29.1
			bcc-(Fe,Cr)	*	Im-3m	a=288.5		68.2	30.2	1.7
20	Cr48Fe32Nb20	as cast	(Fe,Cr)$_2$Nb	*	$P6_3/mmc$	a=486.2	c=794.6	40.7	28.8	30.5
			bcc-(Fe,Cr)		Im-3m	a=288.5		62.1	37.1	0.8
21	Cr72Fe3Nb25	as cast	(Fe,Cr)$_2$Nb	*	$P6_3/mmc$	a=492.6(2)	c=808.6(3)	65.6	2.5	31.8
			bcc-(Fe,Cr)		Im-3m	a=289.4(2)		93.7	2.6	3.6
22	Cr69Fe6Nb25	as cast	(Fe,Cr)$_2$Nb	*	$P6_3/mmc$	a=492.1(2)	c=807.5(3)	62.7	5.5	31.8
			bcc-(Fe,Cr)		Im-3m	a=289.3(2)		91.8	5.7	2.5

Sample	nominal composition at.%	annealing	Phases		Space Group	XRD lattice parameters pm		EDX results		
								Cr	Fe	Nb
								at.%		
23	Cr66Fe9Nb25	as cast	$(Fe,Cr)_2Nb$	*	$P6_3/mmc$	a=491.4(4)	c=806.1(4)	60.0	8.5	31.5
			bcc-(Fe,Cr)		Im-3m	a=289.4(2)		90.0	7.4	2.5
24	Cr57Fe3Nb40	as cast	C36-Cr_2Nb	*	$P6_3/mmc$	a=496.0(2)	c=1623.8(10)	61.2	2.9	35.9
			(Nb)		Im-3m	a=326.5(4)		18.6	0.9	80.5
25	Cr54Fe6Nb40	as cast	$(Fe,Cr)_2Nb$	*	$P6_3/mmc$	a=495.3(3)	c=812.7(4)	58.5	5.7	35.7
			(Nb)		Im-3m	a=326.3(3)		17.2	1.6	81.3
26	Cr51Fe9Nb40	as cast	$(Fe,Cr)_2Nb$	*	$P6_3/mmc$	a=494.7(2)	c=808.6(3)	55.6	8.8	35.6
			(Nb)		Im-3m	a=326.7(4)		14.7	2.7	82.7
27	Cr5Fe48Nb47	as cast	□Fe_7Nb_6		R-3m	a=494.8(2)	c=2692(2)	4.2	46.1	49.7
			$(Fe,Cr)_2Nb$	*	$P6_3/mmc$	a=489.6(2)	c=797.9(7)	7.5	55.3	37.2
			(Nb)		Im-3m	a=329.6(6)		1.2	13.0	85.3
28	Cr14Fe34Nb55	as cast	□Fe_7Nb_6	*	R-3m	a=495.5(3)	c=2705(2)	10.5	39.9	49.7
			Phase T (η)		□□□□□□				□□□	
			$(Fe,Cr)_2Nb$		$P6_3/mmc$	a=492.4(7)	c=804(2)	22.4	38.8	38.8
			(Nb)		Im-3m	a=327.4(3)		4.7	7.9	87.4
29	Cr5Fe40Nb55	as cast	□Fe_7Nb_6	*	R-3m	a=495.5(3)	c=2694.8(16)	6.3	43.5	50.2
			□Fe_7Nb_6[a]		R-3m	---		3.9	45.2	50.9
			(Nb)		Im-3m	a=327.8(3)		1.6	10.4	88.1
30	Cr20Fe30Nb50	as cast	□Fe_7Nb_6		R-3m	a=495.5	c=2707	15.5	35.2	49.4
			$(Fe,Cr)_2Nb$	*	$P6_3/mmc$	a=491.8	c=804.9	28.4	33.3	38.2
			(Nb)		Im-3m	a=327.8		6.0	7.2	86.8
31	Cr10Fe50Nb40	as cast	□Fe_7Nb_6		R-3m	a=494.0(2)	c=2690(2)	6.9	44.6	48.5
			$(Fe,Cr)_2Nb$	*	$P6_3/mmc$	a=489.2(2)	c=797.4(4)	11.6	52.2	36.2
32	Cr15Fe45Nb40	as cast	□Fe_7Nb_6		R-3m	a=494.7	c=2696	9.6	37.6	52.9
			$(Fe,Cr)_2Nb$	*	$P6_3/mmc$	a=489.9	c=799.3	16.5	44.3	39.2
			(Nb)		Im-3m	a=330.5		6.0	28.6	65.4

Sample	nominal composition at.%	annealing	Phases		Space Group	XRD lattice parameters pm		EDX results Cr	Fe	Nb
								at.%		
33	Cr20Fe40Nb40	as cast	□-Fe_7Nb_6		R-3m	a=492.2	c=2702	13.3	34.2	52.6
			$(Fe,Cr)_2Nb$	*	$P6_3/mmc$	a=490.7	c=801.5	23.1	38.7	38.3
			(Nb)		Im-3m	a=330.4		6.1	17.0	76.9
34	Cr15Fe37Nb48	as cast	□-Fe_7Nb_6	*	R-3m	a=495.4	c=2702.5	13.3	33.8	52.9
			$(Fe,Cr)_2Nb$		$P6_3/mmc$	a=491.5	c=802.6	20.4	38.7	41.0
			(Nb)		Im-3m	a=327.9		4.4	10.4	85.2
35	Cr45Fe15Nb40	as cast	$(Fe,Cr)_2Nb$	*	$P6_3/mmc$	a=493.7	c=809.5	47.9	15.9	36.3
			(Nb)		Im-3m	a=326.4		13.3	4.5	82.2
36	Cr35Fe25Nb40	as cast	$(Fe,Cr)_2Nb$	*	$P6_3/mmc$	a=492.4	c=806.1	37.5	25.6	37.2
			(Nb)		Im-3m	a=326.8		9.1	6.4	84.6
37	Cr27Fe33Nb40	as cast	$(Fe,Cr)_2Nb$	*	$P6_3/mmc$	a=491.6(8)	c=804.2	28.9	34.1	37.0
			□-Fe_7Nb_6		R-3m	a=496.3	c=2711.3	15.8	35.3	48.9
			(Nb)		Im-3m	a=327.5(1)		6.4	6.8	86.9
38	Cr63Fe12Nb25	as cast	$(Fe,Cr)_2Nb$	*	$P6_3/mmc$	a=490.4	c=803.9	56.7	11.4	31.8
			bcc-(Fe,Cr)		Im-3m	a=288.9		86.6	11.4	2.0
39	Cr55Fe20Nb25	as cast	$(Fe,Cr)_2Nb$	*	$P6_3/mmc$	a=489.1	c=801.3	49.8	19.3	30.9
			bcc-(Fe,Cr)		Im-3m	a=288.7		80.7	17.2	2.1
40	Cr45Fe30Nb25	as cast	$(Fe,Cr)_2Nb$	*	$P6_3/mmc$	a=487.2	c=797.2	40.9	28.2	30.9
			bcc-(Fe,Cr)		Im-3m	a=288.1		66.0	33.0	1.0
41	Cr35Fe40Nb25	as cast	$(Fe,Cr)_2Nb$	*	$P6_3/mmc$	a=486.3	c=795.7	31.3	38.9	29.8
			bcc-(Fe,Cr)		Im-3m	a=288.3		52.7	46.1	1.3
42	Cr25Fe50Nb25	as cast	$(Fe,Cr)_2Nb$	*	$P6_3/mmc$	a=484.9	c=789.8	22.4	46.5	31.1
			bcc-(Fe,Cr)		Im-3m	a=287.4		39.2	60.2	0.6
43	Cr15Fe60Nb25	as cast	$(Fe,Cr)_2Nb$	*	$P6_3/mmc$	a=482.6	c=790.2	13.0	57.0	30.0
			bcc-(Fe,Cr)		Im-3m	a=287.4		23.3	75.2	1.4
44	Cr5Fe70Nb25	as cast	$(Fe,Cr)_2Nb$	*	$P6_3/mmc$	a=482.2	c=786.2	7.0	83.7	9.3
			bcc-(Fe,Cr)		Im-3m	a=2.872		4.4	65.6	30.0

Sample	nominal composition at.%	annealing	Phases		Space Group	XRD lattice parameters pm		EDX results		
								Cr	Fe	Nb
								at.%		
45	Cr56Fe4Nb40	as cast	$(Fe,Cr)_2Nb$	*	$P6_3/mmc$	a=495.4	c=812.9	59.4	4.0	36.6
			Cr_2Nb		Fd-3m	a=701.6				
			(Nb)			a=326.4		19.1	1.2	79.7
46	Cr55Fe5Nb40	as cast	$(Fe,Cr)_2Nb$	*	$P6_3/mmc$	a=494.9	c=812.2	58.9	5.2	35.9
			(Nb)		Im-3m	a=326.1		17.3	1.7	81.2
47	Cr53Fe7Nb40	as cast	$(Fe,Cr)_2Nb$	*	$P6_3/mmc$	a=494.8	c=811.9	56.6	7.1	36.4
			(Nb)		Im-3m	a=325.9		16.5	1.9	81.6
48	Cr71Fe4Nb25	as cast	$(Fe,Cr)_2Nb$	*	$P6_3/mmc$	a=492.2	c=807.4	64.3	3.8	32.0
			bcc-(Fe,Cr)		Im-3m	a=289.3		92.4	4.2	3.4
49	Cr70Fe5Nb25	as cast	$(Fe,Cr)_2Nb$	*	$P6_3/mmc$	a=492.2	c=807.9	63.8	4.9	31.3
			bcc-(Fe,Cr)		Im-3m	a=289.4		91.8	4.1	4.1

*Table 38 – Composition of the different alloys with their nominal composition. The identified phases, their respective lattice parameters and the chemical composition of each phase is also given. * denotes the primary crystallization of the samples.*

[a]- in eutectic

III. Thermodynamic modeling of the Cr-Fe-Nb ternary system

The commercial databases TCFE6 shows a deficiency in predicting Laves phase formation in the alloy Crofer 22H [165]. The present work aims to provide a better description of the calculated Cr-Fe-Nb phase diagram. The optimization of phase diagrams can only be successfully done if there are enough experimental data of the phase diagram to be studied (e.g. experimental phase diagram and thermodynamic data). The experimental data obtained and previously described were used as basis for the optimization of the phase diagram. In the present work, we propose a computation of the Cr-Fe-Nb phase diagram using the Calculation of Phase Diagram (Calphad) method via an optimization of the Gibbs energy. In addition to experimental data, DFT calculations were done to describe the energies of the end-members.

1. Literature review

1.1. Fe-Nb

A literature survey was given in the Introduction (p. 13). Several optimizations of the Fe-Nb system are available in the literature [34-40]. For the present study we used the latest assessment, which was proposed by Khvan et al. [40]. For their assessment they have used DFT calculations for the description of the end-members as given by Liu et al. [3].

1.2. Fe-Cr

A lot of studies are devoted to the Fe-Cr system due to its importance in many functional and structural materials, e.g. stainless steel. A review of the system has been done by [73]. This review has shown the lack of the previous assessment to describe the magnetic order. Based on this conclusion, a new reassessment down to 0K has been done including experimental data and first principles calculations [73]. They have used a two-sublattice model to describe the σ

1.3. Cr-Nb

An extensive literature review was provided by Schmetterer et al.[2] for this system. They have shown the necessity of reassessing this system as it was proved by Aufrecht et al.[2] that the high temperature laves phase C14 is not stable in Cr-Nb. In their assessment, Schmetterer et al.[2] have used a two-sublattices model for the description of the C15, the energy of formation of which was obtained from DFT calculations (see p. 71 for details and *Figure 30). For the calculation in the ternary system, we used their description of Cr-Nb [29].*

1.4. Cr-Fe-Nb

Regarding its importance in industrial application, the literature on the Cr-Fe-Nb phase diagram is scarce. There is no thermodynamic optimization of the phase diagram available in the literature. The obtained calculated phase diagram from a thermodynamic database (TCFE) is an extrapolation from the lower order boundary systems.

Due to the restricted literature data on this system and the new findings of the Cr-Nb boundary phase diagram, the phase diagram was experimentally reinvestigated providing three different isothermal sections at 700, 1050 and 1350°C, respectively. The results of the study of the isothermal sections have been described previously in part I of this chapter.

The Cr-Fe-Nb phase diagram is characterized by a solid solution of the C14 and C15 Laves phases cutting the phase diagram in two. In addition Cr dissolves in the binary Fe-Nb σ *Figure 43) reveals that this phase does not dissolve Nb.*

Table 31. Thermal analysis and determination of characteristic temperatures has not yet been carried out in this system and no liquidus projection is available in the literature. At the present time, DTA measurements are ongoing for its determination. The invariant reactions from the limiting binary systems are given in Table 37.

2. Thermodynamic modeling

The CALculation of PHAse Diagrams (CALPHAD) method was used for the optimization of the thermodynamic modeling of Cr-Fe-Nb phase diagram. Each phase present in the system is described by its Gibbs energy which is described by an appropriate mathematical model. In the present work, the calculations were carried out with Thermo-Calc [144]. The Gibbs energies of the pure elements were defined according to the Dinsdale polynomial [81].

2.1. Solution phases: BCC, FCC and Liquid

The solution phases were modeled with a substitutional model (one-sublattice model). The molar Gibbs energy is given according to equation:

$$G_m^{\alpha} = x_{Cr}\ {}^0G_{Cr}^{\alpha} x_{Cr} + x_{Fe}\ {}^0G_{Fe}^{\alpha} + x_{Nb}\ {}^0G_{Nb}^{\alpha} + RT(x_{Cr}\ln x_{Cr} + x_{Fe}\ln x_{Fe} + x_{Nb}\ln x_{Nb}) + x_{Cr}x_{Fe}x_{Nb}L_{Cr,Fe,Nb}^{\alpha} \quad \text{Eq. 59}$$

The excess Gibbs energy was only used for the liquid phase.

2.2. σ phase

The σ [illegible] *Table 11 in the Calphad chapter).*

$$G^{\sigma} = \sum_{i}\sum_{j}\sum_{z} y_i^1 y_j^2 y_z^3 G_{i:j:z}^{\sigma} + RT\left(10\sum_{i,j,z} y_{i,j,z}^1 \ln y_{i,j,z}^1 + 4\sum_{i,j,z} y_{i,j,z}^2 \ln y_{i,j,z}^2 + 16\sum_{i,j,z} y_{i,j,z}^3 \ln y_{i,j,z}^3\right) \quad \textit{Eq. 60}$$

Where y_i^k [illegible] $G_{i:j:z}^{\sigma}$ [illegible]

2.3. Laves phases C14 and C15

The Laves phases are the largest group of intermetallic phases with an ideal stoichiometry AB_2. The C14 and C15 are closely related by their structure. Although C14 contain three different Wyckoff positions, it is common to model it as a two sublattices model $(A,B)(A,B)_2$, first due to the occupancy of each atom in one sublattice and secondly to be consistent with the C15 Laves phase which contains only two independent positions. The two-sublattice model can be as well used by extension into the ternary system $(A,B,C)(A,B,C)_2$.

The total Gibbs energy of C14 and C15 Laves phases according to the two-sublattice models is written:

$$G^{\lambda} = \sum_i \sum_j y_i^1 y_j^2 \, G_{i:j}^{\lambda} + RT\left(2\sum_i y_i^1 \ln y_i^1 + \sum_i y_i^2 \ln y_i^2\right) + \sum_i \sum_j \sum_k y_i^1 y_j^2 y_k^3 L_{i:j,k}^{\lambda} \qquad \textit{Eq. 61}$$

Where λ [illegible] y_i^1 [illegible] y_j^2 [illegible] y [illegible] $G_{i:j}^{\lambda}$ [illegible]

2.4. <u>μ phase</u>

The μ [illegible]

3. DFT calculations

The DFT calculations were carried out using the VASP software package [96] using the GGA:PBE for the description of the exchange and correlation energy and the projector augmented waves (PAW) [145] as basis set. For all calculations, the ground state energies were reached in three steps: 1) the volume and the ion positions were relaxed; 2) the stresses and forces were relaxed; 3) the tetrahedron method was used for accurate calculations of the ground state energy using a k-mesh point for the description of the periodicity of the crystal structure according to Monshort-Pack (i.e. 9x9x5 for [illegible] μ [illegible] *Eq. 25 according to the chosen sublattice model.*

The energies of the pure elements calculated in their stable form are given in Table 39, the comparison of these results were compared in Chapter III dedicated to the pure elements.

Phase	*k-points*	*E (kJ.mol^{-1}.atom^{-1})*	*a (Å)*
α [illegible]	[illegible]	[illegible]	
[illegible]	[illegible]	[illegible]	[illegible]
[illegible]	[illegible]	[illegible]	[illegible]

Table 39 – Total Energy ground state of the pure elements calculated by DFT.

The energy of formation of the end-members which were available in the literature were not recalculated, they are given in Table 40-43 with their respective references. For the C14 Laves phase, the calculated enthalpies of formation in the Fe-Nb system were taken from Liu et al. [38]. The end-members of C15

71).

4. Results and discussions

4.1 DFT calculations

The energies of formation of the different end-members calculated for each phase are reported in Table *40-43. For the different phases, some tendency on the stability of the end-members can be seen according to these results.*

a. σ phase

The energies of the end-members according to the three sublattices model (Fe,Nb)$_{10}$(Cr,Nb)$_4$(Fe,Nb,Cr)$_{16}$ are given in *Table 40. The present results are compared with available literature data.*

				FM			*NM*			
$A_2^{12}D_8^{12}$	*B_4^{15}, 4f*	*$C_8^{14}E_8^{14}$*	*Compound*	Δ			Δ			

Table 40 – Energies of formation of the different end-members calculated in the σ phase.

The results of the enthalpies of formation in the σ phase are plotted as an iso-contour plot in *Figure 61* as a function of composition.

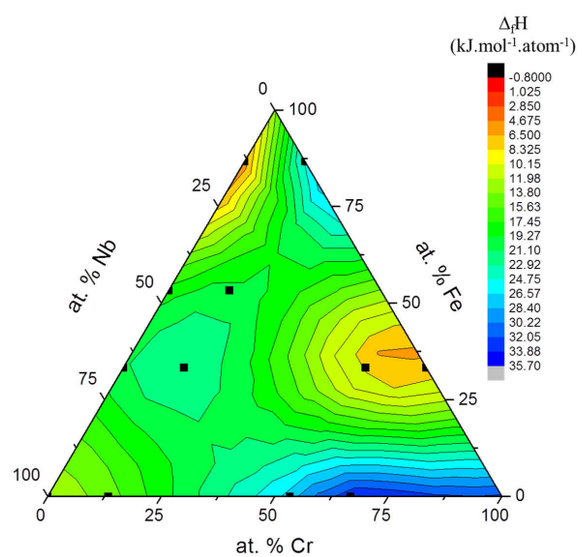

Figure 61 – Ternary iso-contour of the relaxed structure (given in kJ.mol^{-1}.atom^{-1}) of the hypothetical end-members calculated by DFT in the σ phase according to a three sublattices model.

According to the chosen sublattice model to describe the σ phase, none of the end-members are stables (*Table 40* and *Figure 61*) which are consistent with experimental data (see isothermal section at 700°C – *Figure 43*– indicating that no Nb dissolves in the σ phase).

b. Laves phase C14 and C15

The total energies of the end-members in the C14 and C15 Laves phase are given in *Table 41* and *Table 42*, respectively.

		Δ			Δ			
		-11.88	4.82	7.88	-10.06	4.77	7.8	present work
		-13.16	4.822	7.839	-12.99	4.766	7.811	[38]
		-14.5	-	-				[156]
		-14.5	4.768	7.875				[157]
	Nb_2Fe	60.39	5.44	8.29	81.29	5.36	8.30	present work
		60.01	5.42	8.59	79.03	5.23	8.587	[38]
		2.1	-	-				[137]
		2.03	5.248	8.198				[157]
	Fe_2Fe	25.6	4.68	7.75	37.3	4.49	7.46	present work
		14.71	4.68	7.62	35.42	4.531	7.29	[38]
		38.81	-	-				[156]
		14.7	4.69	7.668				[137]
		31.1	-	-				[157]
		38.27	4.53	7.23				[155]
	Nb_2Nb				14.23	5.59	8.54	present work
					16.54	5.47	8.7	[38]
					15.602	-	-	[156]
					15.6	5.492	8.642	[157]
					15.4			[137]
					16.2	5.5	8.68	[26]
	Cr_2Cr	27.48	4.64	7.66	27.48	4.64	7.66	Present work
		28	4.67	7.691				[157]
		28.63	4.64	7.66				[26]
		25.4	-	-				[137]
	Cr_2Nb	-6.58	4.88	8.06	-6.58	4.88	8.06	Present work
		-3.38	4.9	8083				[157]
		-1.81	4.88	8.06				[26]
		-0.61						[133]
	Nb_2Cr	68.99	5.34	8.32	70.32	5.47	8.01	Present work
		71.7	5.482	8.033				[157]
		76.52	5.38	8.36				[26]
	Cr_2Fe	29.8	4.61	7.42	30.84	4.61	7.42	Present work
		31.1	4.634	7.459				[157]
	Fe_2Cr	23.96	4.64	7.56	22.95	4.56	7.27	Present work
		16.8	4.65	7.47				[157]

Table 41 – Energies of the end-members of the C14 Laves phase compared with available literature data.

		Δ			Δ			
		-1.83	6.96	337.2	-1.72	6.93	332.8	Present work (ADF) [29]
		-3.31	6.93	333.1				[26]
		-2.48	6.82	317.2				[133]
		-2.31	6.93	332.8				[135]
		-2.1	6.94	334.3				[134]
		2.34						[136]
		-4.63	6.949	335.6				[157]
	Nb_2Cr	75.38	7.51	423.6	75.39	7.50	422.38	Present work [29]
		75.33	7.5	421.2				[26]
		60.4	7456	414.5				[157]
	Cr_2Cr	30.56	6.64	292.75	33.55	6.66	287.5	Present work [29]
		27.29	6.58	284.9				[26]
		26.4	-					[137]
		26.6	6.616	289.6				[157]
	Nb_2Nb				15.33	7.74	463.7	Present work [29]
					16.2	7.69	455.5	[26]
					16.2	-		[137]
					15.7	7.678	452.6	[157]
	Cr_2Fe	27.72	6.7	287.5	27.72	6.88	325.7	present work
		28.7	6.521	277.3				[157]
	Fe_2Cr	18.6	6.82	317.2	29.5	6.8	314.4	Present work
		25.4	6.44	267.1				[157]
	Fe_2Fe	39.43	6.8	314.4	52.04	6.75	307.5	Present work
		34.6	6.44	267.6				[157]
	Nb_2Fe	50.23	7.94	428.6	80.0155	7.4388	411.6	Present work
		75.3	7.393	404.1				[157]
	Fe_2Nb	-14.4	6.82	317.9	-9.88	7.13	362.4	Present work
		-14.3	6.799	314.3				[157]

Table 42 – Enthalpies of formation of the different end-members of the C15 Laves phase. The similar end-members as for the Cr-Nb system were calculated using ADF as described in p. 72 and in reference [29].

The enthalpies of formation of the end-members of C14 and C15 (Table 41, Table 42) are compared in Figure 62. The assessed enthalpies of formation of C14-Fe_2Nb and C15-Cr_2Nb are also given for comparison.

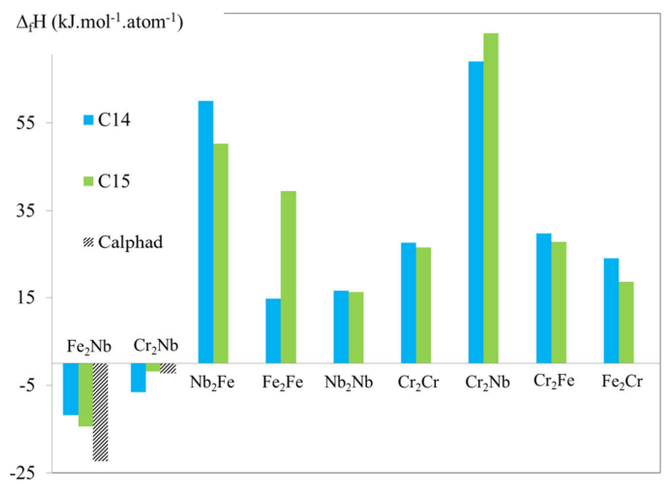

Figure 62 – Comparison of the enthalpies of formation of C14 and C15 Laves phase. For the stable end-members, i.e. C14-Fe_2Nb and C15-Cr_2Nb the Calphad optimized values have been added for comparison from references [29,40] *for Fe-Nb and Cr-Nb, respectively.*

The enthalpies of formation of the two different polytypes of Laves phase are very close. For the two stable end-members, the respective metastable end-members are more stable energetically according to the DFT calculations. As the two polytypes are closely related, these results are not surprising, furthermore within the approximation done to do the DFT calculations the difference of energies between the two polytypes is in the range of the accepted error. For C14-Fe_2Nb and C15-Cr_2Nb, the Calphad optimized value is lower (i.e. more stable) that its respective value obtained from DFT. For both thermodynamic assessments the optimization of the energy of formation of the stable end-members was obtained by taking into account experimental data.

c. μ phase

According to the DFT results (*Table 43*), the plot of the energies of the end-members of the μ phase in the Cr-Fe-Nb is given in *Figure 63*.

					Δ[illegible]			Δ[illegible]			[illegible]
[illegible]				[illegible]	[illegible]	[illegible]	[illegible]	[illegible]	[illegible]		
[illegible]				[illegible]	[illegible]	[illegible]	[illegible]	[illegible]	[illegible]	[illegible]	Present work
Fe	Nb	Fe	Nb	Fe_3Nb_{10}	32.81	5.42	27.53	34.69	5.44	27.37	[38]
Fe	Nb	Nb	Fe	$FeNb_6$	-12.55	4.86	27.00	-9.05	4.88	26.25	[38]
					-13.50	4.87	26.64	-	-	-	[157]
Fe	Nb	Nb	Cr	$FeNb_5Cr_6$	-6.60	4.85	29.07	-6.60	4.85	27.82	Present work
Fe	Nb	Nb	Nb	$FeNb_{12}$	13.54	5.42	28.14	13.71	5.48	27.44	[38]
Fe	Nb	Cr	Fe	$FeNb_4Cr_2$	-12.06	4.76	27.01	-9.71	4.77	26.60	Present work
Fe	Nb	Cr	Cr	$FeNb_3Cr_3$	-4.18	4.76	28.11	-4.16	4.76	28.11	Present work
Fe	Nb	Cr	Nb	$FeNb_{10}Cr_2$	14.38	5.43	28.01	16.13	5.43	27.99	Present work
Cr	Nb	Fe	Fe	$CrNb_2Fe_8$	-6.46	4.78	26.76	-4.88	4.79	26.39	Present work
Cr	Nb	Fe	Cr	$Cr_2Nb_4Fe_2$	-0.23	4.77	28.22	1.45	4.75	28.13	Present work
Cr	Nb	Fe	Nb	$CrNb_9Fe_2$	21.08	5.29	29.00	21.08	5.29	29.00	Present work
Cr	Nb	Nb	Fe	$CrNb_2Fe_6$	-19.35	4.88	27.85	-16.39	4.92	27.17	Present work
Cr	Nb	Nb	Nb	$CrNb_{12}$	4.03	5.44	29.31	4.05	5.44	29.29	Present work
Cr	Nb	Nb	Cr	Cr_2Nb_6	-6.93	4.90	28.85	-7.30	4.97	29.17	Present work
					-0.77	4.92	27.64	-	-	-	[157]
Cr	Nb	Cr	Fe	$Cr_2Nb_4Fe_6$	-8.45	4.80	8.92	-6.62	4.82	26.32	Present work
Cr	Nb	Cr	Cr	Cr_3Nb_4	-0.68	4.79	28.03	-0.68	4.79	26.77	Present work
Cr	Nb	Cr	Nb	Cr_2Nb_{10}	16.42	5.45	28.07	17.86	5.44	28.07	Present work
Nb	Nb	Fe	Fe	Nb_3Fe_8	-2.11	4.85	26.66				[38]
Nb	Nb	Fe	Cr	$Nb_5Fe_2Cr_6$	5.34	4.82	28.84	7.03	4.79	28.79	Present work
Nb	Nb	Fe	Nb	$Nb_{11}Fe_2$	38.40	5.45	28.49	38.44	5.45	28.52	[38]
Nb	Nb	Nb	Fe	Nb_7Fe_6	-10.11	4.97	27.03	-7.60	5.02	26.10	[38]
					67.98	5.25	25.82	-	-	-	[157]
Nb	Nb	Nb	Cr	Nb_7Cr_6	-2.75	4.97	29.17	-2.75	4.97	29.17	Present work
					66.11	5.30	26.22				[157]
Nb	Nb	Nb	Nb	Nb_3	-	-	-	17.50	5.46	28.83	[38]
					-	-	-	20.70	-	-	[137]
					-	-	-	16.10	4.43	9.52	[157]
Nb	Nb	Cr	Fe	$Nb_5Cr_2Fe_6$	-8.41	4.86	27.30	-6.52	4.90	26.69	Present work
Nb	Nb	Cr	Cr	Nb_3Cr_8	3.27	4.84	28.70	3.27	4.84	28.70	Present work
Nb	Nb	Cr	Nb	$Nb_{11}Cr_2$	15.21	5.41	29.18	17.03	5.44	28.89	Present work

Table 43 – Enthalpies of formation of the end-members of the μ phase obtained from DFT calculations.

According to the DFT results, Cr dissolving in the binary Fe-Nb μ phase is more favorable on the 3b Wyckoff position as it can be seen by comparing the enthalpies of formation of Fe:Nb:Nb:Cr ($FeNb_6Cr_6$, Δ_fH= -6.60 kJ.mol^{-1}.atom^{-1}) and Cr:Nb:Nb:Fe ($CrNb_6Fe_6$, Δ_fH = -19.35 kJ.mol^{-1}.atom^{-1}).

The contour map of the results of the enthalpies of formation is given in *Figure 63*.

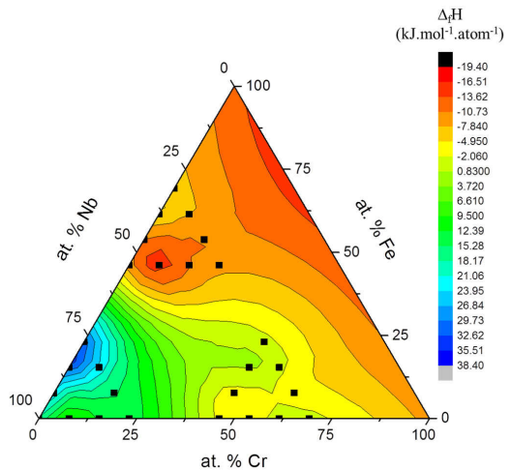

Figure 63 – Ternary iso-contour plot of the ground state energies of the hypothetical end-members (black point) calculated by DFT in the μ phase according to a four sublattices model $(Fe,Cr,Nb)(Nb)_4(Fe,Cr,Nb)_2(Fe,Cr,Nb)_6$. The enthalpies of formation are given in kJ.mol^{-1}.atom^{-1}.

The results of the enthalpies of formation of the end-members show that this phase is stable throughout a large part of phase diagram, which is inconsistent with the stability of the μ phase determined experimentally. In the Nb-rich corner, the enthalpies of formation of the end-members are positive and therefore unstable, which is consistent with experimental evidence. Nevertheless, on the Cr-Nb side, the end-members are rather too stable, stabilizing the μ phase on this side of the phase diagram. Because this phase should not be stable in the Cr-Nb side, the end-members on this side of the phase diagram will have to be optimized in order to fit to the experimental evidence.

4.2 Optimization of the phase diagram

The optimization of the phase diagram was obtained according to the Calphad formalism using Thermo-Calc software [8]. For the description of the different phases, the energies of formation of the end-members obtained by DFT were used.

At first the phase diagram was calculated using the energies of the hypothetical end-members obtained from DFT without any modification. The calculated Cr-Fe-Nb phase equilibria are given in *Figure 64*.

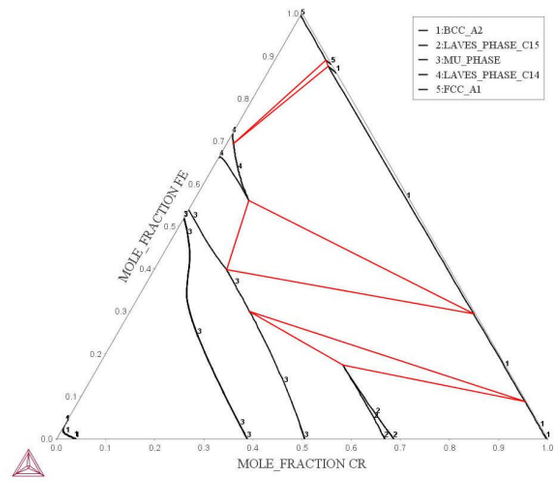

Figure 64 – Calculated isothermal section at 1050°C of the Cr-Fe-Nb phase diagram using the DFT values for the description of the end-members.

As the μ phase is rather too stable according to the DFT calculations, this phase appears to be quite stabilized on the Cr-Nb side which is inconsistent with experimental evidence. In addition the description of the C14 Laves phase is not stable enough. According to this result, the σ phase does not appear which is consistent with the experimental results.

a. BCC, FCC

These two phases are well represented by using the binary interaction parameters. In the present work, no ternary interaction was used to describe these phases.

b. Liquid

The liquidus values are not yet available for the present optimization of the phase diagram. The ternary interaction parameters cannot be accurately optimized. Nevertheless, the liquid phase appeared in the highest calculated isothermal section (i.e. 1350°C) which is in contradiction to experimental evidence (*Figure 45*).

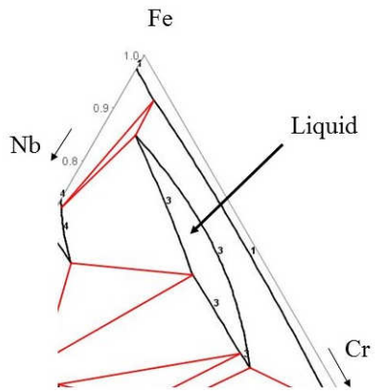

Figure 65 – Calculated iron reach corner of the Cr-Fe-Nb phase diagram at 1350°C showing the presence of the liquid phase.

As the liquid should not be present at this temperature, interaction parameters were guessed in such way that the liquid is not present at this temperature. To describe the liquid phase, ${}^{0}L_{Cr,Fe,Nb}={}^{1}L_{Cr,Fe,Nb}={}^{2}L_{Cr,Fe,Nb}=30000$ were used. In this way, the excess Gibbs energy is desymmetrized and the liquid is not stable at 1350°C. Nevertheless, further data are necessary for an accurate description of the liquid phase.

c. *Intermetallic phases*

As the DFT calculations of the end-members of the different phases are considered accurate, most of the enthalpies of formation are kept as obtained by this calculation. In order to modify the stability of the phases, the temperature dependence parameters of specific key end-members were optimized instead.

Nevertheless, as the C14 and C15 are closely related by their crystal structure, by their energy and symmetry in this system, the enthalpies of formation of the end-members have to be consistent with the stability of the Laves phases polytypes.

C14 and C15 Laves phase

In the present Cr-Fe-Nb system, the two Laves phase are symmetric to each other and cross the phase diagram from one binary side (i.e. Fe-Nb) to the other (i.e. Cr-Nb). This feature has to be taken into account for the optimization of the phase diagram. The parameters of one side of the phase diagram were fixed according to the other side. For example the parameters of the C15-CrNb binary system from Schmetterer et al. [29] were used to describe the interactions parameters of the C14-CrNb. It results:

$$ {}^{0}L^{C15}_{Cr,Nb:Cr} = {}^{0}L^{C15}_{Cr,Nb:Nb} = {}^{0}L^{C14}_{Cr,Nb:Cr} = {}^{0}L^{C14}_{Cr,Nb:Nb} \quad \text{Eq. 62} $$

$$ {}^{0}L^{C15}_{Cr:Cr,Nb} = {}^{0}L^{C15}_{Nb:Cr,Nb} = {}^{0}L^{C14}_{Cr:Cr,Nb} = {}^{0}L^{C14}_{Nb:Cr,Nb} \quad \text{Eq. 63} $$

As C14-Cr_2Nb is not stable, the enthalpy of formation of this end-member was first set up to 500 $J.mol^{-1}$ lower than for C15-Cr_2Nb and keeping the same temperature dependence. The two parameters were then optimized by taking into account the two experimental three phase fields (i.e. Nb+C14+C15 and Cr+C14+C15). For C15 Fe_2Nb, the enthalpy of formation by DFT was taken as it is lower than the Calphad optimized value of C14-Fe_2Nb value. Its temperature dependence was optimized.

Interactions parameters ${}^{0}L^{C14}_{Cr:Fe,Nb}$

μ phase

As the μ [illegible] Table 44, +80 and +20, respectively).

On the Fe-Nb side, the Cr:Nb:Nb:Fe end-member is rather too stable which makes the μ [illegible]

4.3 Results of the optimization of the phase diagram

***The obtained calculated isothermal sections are presented in** Figure 66 and Figure 67 and compared with experimental data. The proposed optimized parameters lead – in general – to a good description of the phase diagram.*

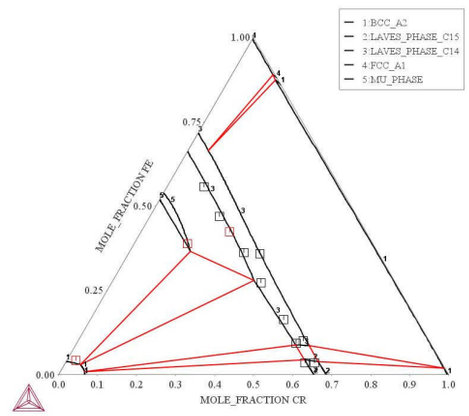

Figure 66 – Calculated isothermal sections at 1050°C obtained from the present optimized parameters as given in Table 44 and compared with experimental data (black squares, phase boundary of the Laves phase and red squares, the three phase field C14+μ+BCC).

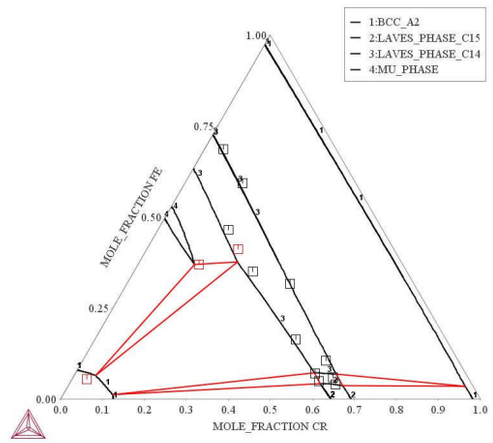

Figure 67 – Calculated isothermal sections at 1350°C from the present optimization compared with experimental data (black squares phase boundary of the Laves phases and red squares the three phase field μ+C14+(Nb)).

Table 44 provide a good accuracy of the description of the different phases for the highest isothermal sections (i.e. 1350°C, see Figure 67). Nevertheless, at lower temperatures, the μ

	${}^{0}L^{L}_{Cr,Fe,Nb} = {}^{1}L^{L}_{Cr,Fe,Nb} = {}^{2}L^{L}_{Cr,Fe,Nb} = 30000$	
	${}^{0}G^{C14}_{Cr:Nb} = -3704.2 - 11.687 \times \mathrm{T}$	
	${}^{0}L^{C14}_{Cr,Nb:Cr} = {}^{0}L^{C14}_{Cr,Nb:Nb}$ ${}^{0}L^{C15}_{Cr,Nb:Cr} = {}^{0}L^{C15}_{Cr,Nb:Nb} =$	
	${}^{0}L^{C14}_{Cr:Cr,Nb} = {}^{0}L^{C14}_{Nb:Cr,Nb}$ ${}^{0}L^{C15}_{Cr:Cr,Nb} = {}^{0}L^{C15}_{Nb:Cr,Nb} =$	
	${}^{0}L^{C14}_{Cr:Fe,Nb} = -100000$	
	${}^{0}G^{C15}_{Fe:Nb} = -43200 + 7.347 \times T$	
μ	${}^{0}G^{\mu}_{Cr:Nb:Nb:Cr} = -90090 + 80 \times T$	
	${}^{0}G^{\mu}_{Fe:Nb:Nb:Cr} = -85761 + 30 \times T$	
	${}^{0}G^{\mu}_{Nb:Nb:Cr:Fe} = -109330 - 60 \times T$	
	${}^{0}G^{\mu}_{Cr:Nb:Nb:Fe} = -251550 + 80 \times T$	

Table 44 – Optimized parameters for the description of the calculated Cr-Fe-Nb phase diagram.

Chapter VI – Thermodynamic modeling of the Fe-Nb-Si system

Introduction

The Fe-Nb-Si ternary system is important for industrial applications. As explained in the introduction, silicon plays an important role on the stabilization and promotion of the Laves phases. The reason that Froitzheim [3] proposed to add Si in addition to Nb and W in the interconnector steel called Crofer 22 AP was to prevent Si-diffusion at the Cr_2O_3/alloy interface by forming a dense isolating SiO_2 by oxidation and to promote the formation of Laves phase. This modified steel is known under the name Crofer 22H [1].

Several studies outlined the importance of this system because of:

- the extension of the Laves phase into the ternary phase diagram [15]
- the precipitation of Laves phase in ferritic steel which improve the mechanical properties of structural materials [2]
- the ternary compound $Nb_6Fe_2Si_7$ with its high oxidation resistance can be used as coating for Nb-silicide applications [71].

Furthermore the calculated phase diagram would be of great importance for a better understanding of the chemical driving forces between the phases especially in the middle of the phase diagram (30 at. % Si) [71], where several ternary compounds surround each other. The different ternary compounds have closely related structures and their formation would be well understood by knowledge of their Gibbs energy function obtained from a thermodynamic assessment of this system.

I. Literature

Only few studies of the Fe-Nb-Si ternary system are available in the literature. An intensive discussion about the literature of this system has been given in the Literature survey (p. 20).

Table 7.

II. Thermodynamic modeling

The thermodynamic modeling of Fe-Nb-Si is not available in the literature. In commercial thermodynamic databases (i.e. TCFE6), the representation of this system does not include the different ternary compounds. Furthermore as silicon is not included for the description of Laves phase, this phase appears as a mutual solid solution crossing the complete phase diagram from the Fe-Nb to the Nb-Si side (see *Figure 13).*

The experimental and calculated phase diagrams (See Figures 8-13 in the literature survey, p. 20) are in disagreement to each other. The thermodynamic modeling is relevant for the understanding of the phase

Figure 68 with their respective references.

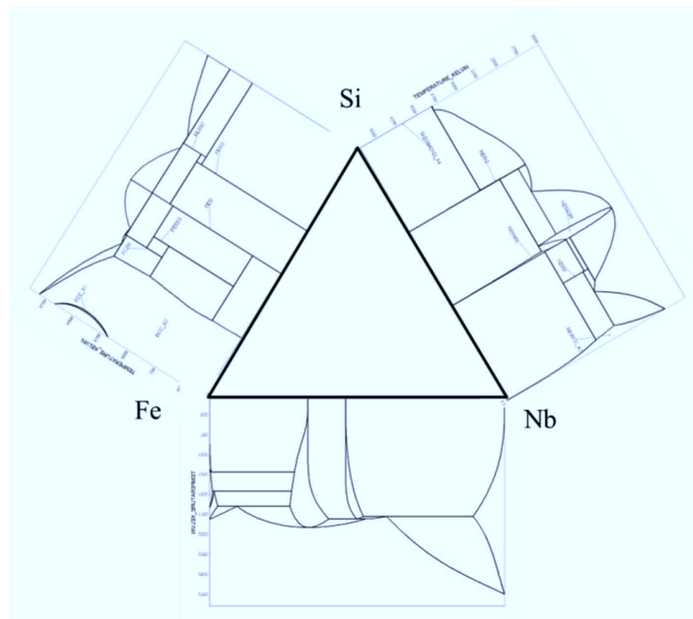

Figure 68 – Binary boundary phase diagrams as given in the literature: Fe-Nb [40], Nb-Si [75] and Fe-Si [175].

1. Fe-Nb

The Fe-Nb system has been assessed several times during the last couple of years [38–40,156] and is still subject of new studies due to some difficulties to use the binary calculated phase equilibria for higher

$(Fe,Nb)_2(Fe,Nb)$ and a four sublattice model for the description of the μ $(Fe,Nb)(Nb)_4(Fe,Nb)_2(Fe,Nb)_6$.

2. Nb-Si

There are several assessments of this system available in the literature. In the TCFE6 database, the optimization of this system has been taken from Fernandes et al. [176]. In their assessment, they described the high temperature and the low temperature Nb_3Si phases as two different phases with different sublattice models. Whereas

3. Fe-Si

The Fe-Si system was recently subject of discussion as the description of Lacaze and Sundman [127], used in commercial databases and in higher order systems, contains a high temperature miscibility gap and it is not recommended to use it for higher order system. This system is rather important for industrial materials such as steel. It is so necessary to have a correct representation of the calculated phase diagram. One of the major difficulties for the calculated description of the Fe-Si phase diagram is the α_3-B2/DO phase transition. In the assessment of Lacaze and Sundman [127] the α_3 phase is not described.

Ohnuma et al. [74] made experimental work and used diffusion couples to study the α_3/B2/DO transition. Then they proposed a thermodynamic assessment with ordered/disordered phases (A2, B2 and DO

4. Fe-Nb-Si

There is no thermodynamic modeling of the Fe-Nb-Si system in the literature. In addition to the dissolution of a third element into the binary phases, there are six ternary compounds as mentioned in the literature survey. Their crystallographic structures have been investigated and are available in the literature (given in *Table 7, p. 20). For the thermodynamic modeling of the Fe-Nb-Si ternary system, we take into account the dissolution of a third element into the binary phases (e.g. Si in Laves and μ phases) as well as the ternary phases. The ternary phases have no perceptible homogeneity range, they were therefore defined as stoichiometric compound for the Calphad modeling.*

The optimization of the phase diagram was done using Thermo-Calc [8] based on experimental data [15]. In addition, enthalpies of formation of the different end-members have been calculated using the DFT method. The thermodynamic modeling of this system can only be done partially as there are no reliable liquidus data, which are nevertheless of great importance for the optimization of a phase diagram.

4.1 Laves phase

The C14 Laves phase polytype crystallizes in the space group $P6_3/mmc$ with three different occupied Wyckoff positions. Within its usual formula AB_2, A occupies the 4f position and B the 2a and 6h

4.2 μ phase

The *μ □□□ □□ □□□□ □ R-3m. The atoms are allocated into five different Wyckoff positions. In the ternary Fe-Nb-Si system, significant amounts of Si dissolve in this phase. Following the principle of the sublattice model where each atom may occupy each different Wyckoff position would yield to 243 different end-members according to:*

(Fe,Nb,Si)(Fe,Nb,Si)$_2$(Fe,Nb,Si)$_2$(Fe,Nb,Si)$_2$(Fe,Nb,Si)$_6$.

This would be rather computationally expensive. In order to reduce the number of end-members, some sublattices were combined. Joubert and Dupin [85] suggested a four-sublattice model where the second and the third sublattices are combined and only contain Nb:

(Fe,Nb,Si)(Nb)$_4$(Fe,Nb,Si)$_2$(Fe,Nb,Si)$_6$.

This model has been described in the Calphad part (p. 37).

4.3 Ternary compounds

The ternary compounds have been modelled as line compounds as they do not show homogeneity range.

The Gibbs energy of the considered phases are written:

FeNbSi

$$G^{FeNbSi} - \sum x_i^0 H_i(298.15K) = a + bT + 0.333\ {}^0G_{Fe}^{BCC} + 0.333\ {}^0G_{Nb}^{BCC} + 0.333\ {}^0G_{Si}^{Diamond} \quad \text{Eq. 64}$$

FeNbSi₂

$$G^{FeNbSi_2} - \sum x_i^0 H_i(298.15K) = a + 0.25\ {}^0G_{Fe}^{BCC} + 0.25\ {}^0G_{Nb}^{BCC} + 0.5\ {}^0G_{Si}^{Diamond} \quad \textit{Eq. 65}$$

$Fe_4Nb_4Si_7$

$$G^{Fe_4Nb_4Si_7} - \sum x_i^0 H_i(298.15K) \quad \textit{Eq. 66}$$

$$= a + bT + 0.267\ {}^0G_{Fe}^{BCC} + 0.267\ {}^0G_{Nb}^{BCC} + 0.467\ {}^0G_{Si}^{Diamond}$$

$Fe_3Nb_4Si_5$

$$G^{Fe_3Nb_4Si_5} - \sum x_i^0 H_i(298.15K) \quad \textit{Eq. 67}$$

$$= a + 0.25\ {}^0G_{Fe}^{BCC} + 0.333\ {}^0G_{Nb}^{BCC} + 0.4167\ {}^0G_{Si}^{Diamond}$$

$FeNb_4Si$

$$G^{FeNb_4Si} - \sum x_i^0 H_i(298.15K) \quad \textit{Eq. 68}$$

$$= a + bT + 0.167\ {}^0G_{Fe}^{BCC} + 0.667\ {}^0G_{Nb}^{BCC} + 0.167\ {}^0G_{Si}^{Diamond}$$

With a is expressing the enthalpy of formation of the considered compound and b is the temperature contribution term to the Gibbs energy. The a terms were obtained from DFT calculation for the ternary compounds with no mixed occupation in their Wyckoff position (i.e. Nb_4FeSi, FeNbSi, $Fe_4Nb_4Si_7$ and $FeNbSi_2$) in order to have a primary overview of their thermodynamic stability.

III. DFT calculations

The enthalpy of formation at 0 K of the end-members was obtained according to the formula *Eq. 25) taking into account the energy of the pure elements in their stable structure (Pure elements chapter, p. 59).*

The DFT calculations were done using the VASP software package [96] within the framework of the projector augmented wave method [103] using the PBE exchange correlation-potential [121]. An energy cutoff of 400 eV was chosen for all calculations. The Brillouin zone was chosen carefully according to the

μ [illegible]

[illegible]

Table 47 with the results of their respective enthalpy of formations and lattice parameters. For each structure, the minimization of the energy to reach the ground state was obtained in three steps: 1) Relaxation of the ionic positions and volume, 2) Forces, stresses and volume were relaxed, 3) Tetrahedron method was used for an accurate calculation of the total energy. As the studied system contains Fe, we took into account the magnetism. Calculations were done for non-magnetic (NM) and ferromagnetic (FM) compounds in order to check the most stable state.

IV. Results and discussion

1. DFT calculations

As previously mentioned, the enthalpies of formation of the different end-members were calculated using VASP. Some of the different end-members (i.e. Laves and [illegible] *Table 45 and Table 46).*

1.1 C14 Laves phase

The results of the enthalpy of formation and the lattice parameters according to the two sublattice model are presented in*Table 45 for the Laves phase.*

Compound		FM				NM				References
		$\Delta_f H$ (kJ.mol-1.atom-1)	Lattice parameters		V (Å³)	$\Delta_f H$ (kJ.mol-1.atom-1)	Lattice parameters			
			a (Å)	c (Å)			a (Å)	c (Å)	V (Å³)	
C14 Laves phase	Fe_2Nb	**-11.88**	4.82	7.88	160.2	-10.06	4.77	7.8	153.7	present work
		-13.16	4.822	7.839	157.9	-12.99	4.766	7.811	157.9	[38]
		-14.5	-	-	-					[156]
		-14.5	4.768	7.875	155.04					[157]
	$FeNb_2$	**60.39**	5.44	8.29	212.46	81.29	5.36	8.3	206.51	present work
		60.01	5.42	8.59	218.54	79.03	5.23	8.587	218.7	[38]
		2.1	-	-						[137]
		2.03	5.248	8.198	195.54					[157]
	$FeFe_2$	**37.2**	4.52	7.23	127.92					present work
		14.71	4.68	7.62	144.54	35.42	4.531	7.288	129.6	[38]
		38.81	-	-						[156]
		14.7	4.69	7.668	146.07					[157]
		31.1	-	-						[137]
		38.27	4.53	7.23	128.49					[155]
	$NbNb_2$					**14.23**	5.59	8.54	230.9	present work
						16.54	5.47	8.7	229.6	[38]
						15.602	-	-		[156]
						15.6	5.492	8.642	225.74	[157]
						15.4				[137]
						16.2	5.5	8.68	227.39	[26]
	$SiSi_2$					47.46	5.6	6.92	187.94	present work
						2.5				[137]
						56.52	5.6	6.91	187.67	[155]
	$NbSi_2$					-6.17	4.99	7.93	171.00	present work
	$SiNb_2$					40.38	5.42	8.58	218.94	present work
	$FeSi_2$	37.03	5.28	6.79	163.93					present work
		48.92	5.11	6.93	156.71					[155]
	$SiFe_2$	8.59	4.66	7.67	144.24					present work
		19.91	4.55	7.56	135.54					[155]

Table 45 – Calculated enthalpies of formation of the C14 Laves phase end-members in the Fe-Nb-Si ternary system. In red, the enthalpies of formation which have been used for the assessment.

1.2 <u>μ phase</u>

Enthalpies of formation computed by DFT for the μ phase are given in *Table 46* according to the four sublattice model.

End-members					FM			NM			Ref.
(Fe,Si,Nb)	**$(Nb)_4$**	**$(Fe,Nb,Si)_2$**	**$(Fe,Si,Nb)_6$**	Compound	$\Delta_f H$ ($kJ.mol^{-1}.atom^{-1}$)	a (Å)	c (Å)	$\Delta_f H$ ($kJ.mol^{-1}.atom^{-1}$)	a (Å)	c (Å)	
Fe	Nb	Fe	Fe	Fe_9Nb_4	**-7.71**	4.84	25.43	0.32	4.71	25.79	[38]
Nb	Nb	Fe	Fe	Fe_8Nb_5	**-2.11**	4.85	26.66				[38]
Fe	Nb	Nb	Fe	Fe_7Nb_6	-13.04	4.88	26.74				**Present work**
					-12.55	4.86	27.00	-9.05	4.88	26.25	[38]
					-13.50	4.87	26.64	-	-	-	[157]
Nb	Nb	Nb	Fe	Fe_6Nb_7	**-10.11**			-7.60	5.02	26.10	[38]
Fe	Nb	Fe	Nb	Fe_3Nb_{10}	**32.81**	5.42	27.53	34.69	5.44	27.37	[38]
Nb	Nb	Fe	Nb	Fe_2Nb_{11}	**38.44**	5.45	28.49	38.40	5.45	28.52	[38]
Fe	Nb	Nb	Nb	$FeNb_{12}$	**13.54**	5.42	28.14	13.71	5.48	27.44	[38]
Nb	Nb	Nb	Nb	Nb_{13}	-	-	-	**17.50**	5.46	28.83	[38]
					-	-	-	20.70	-	-	[137]
								16.10	5.43	9.52	[157]
Si	Nb	Nb	Nb	$Nb_{12}Si_1$	-	-	-	4.72	5.31	29.47	**Present work**
Nb	Nb	Nb	Si	Nb_7Si_6	-	-	-	-32.62	5.11	26.80	**Present work**
Si	Nb	Nb	Si	Nb_6Si_7	-	-	-	-22.36	5.08	26.24	**Present work**
Fe	Nb	Nb	Si	$FeNb_6Si_6$	**-43.38**	5.03	26.01	-43.38	5.03	26.01	**Present work**
Si	Nb	Fe	Nb	$Fe_2Nb_{10}Si$	**21.01**	5.23	28.52	21.00	5.22	28.62	**Present work**
Nb	Nb	Fe	Si	$Fe_2Nb_5Si_6$	**-19.79**	4.99	26.26	-19.79	4.99	26.26	**Present work**
Si	Nb	Fe	Si	$Fe_2Nb_4Si_7$	**-7.77**	4.92	25.80	-7.77	4.92	25.80	**Present work**
Fe	Nb	Fe	Si	$Fe_3Nb_4Si_6$	**-32.59**	4.93	25.07	-28.97	4.93	25.07	**Present work**
Si	Nb	Nb	Fe	Fe_6Nb_6Si	**-25.21**	4.90	26.60	-19.41	4.93	25.85	**Present work**
Si	Nb	Fe	Fe	Fe_8Nb_4Si	**-16.24**	4.77	25.78	-11.85	4.79	25.13	**Present work**
Fe	Nb	Si	Fe	$Fe_7Nb_4Si_2$	**-20.73**	4.78	27.44	-13.34	4.75	27.09	**Present work**
Fe	Nb	Si	Si	$FeNb_4Si_8$	**-24.99**	5.16	25.87	-24.79	5.13	25.80	**Present work**
Fe	Nb	Si	Nb	$FeNb_{10}Si_2$	**8.02**	5.34	29.28	8.02	5.34	29.27	**Present work**
Si	Nb	Si	Fe	$Fe_6Nb_4Si_3$	**-37.62**	4.77	27.41	-28.94	4.79	26.78	**Present work**
Si	Nb	Si	Si	Nb_4Si_9	-	-	-	**-2.08**	4.94	29.35	**Present work**
Si	Nb	Si	Nb	$Nb_{10}Si_3$	-	-	-	**-1.28**	5.30	29.90	**Present work**
Nb	Nb	Si	Fe	$Fe_6Nb_5Si_2$	**-14.21**	4.86	28.03	-8.69	4.88	27.26	**Present work**
Nb	Nb	Si	Si	Nb_5Si_8	-	-	-	**-16.48**	5.57	25.74	**Present work**
Nb	Nb	Si	Nb	$Nb_{11}Si_2$	-	-	-	**8.68**	5.35	30.22	**Present work**

Table 46 – Enthalpies of formation and lattice parameters of the end-members in the μ phase of the Fe-Nb-Si system calculated with VASP and compared with available literature data. In red, the data which have been used for the thermodynamic optimization.

The projection of the results of the enthalpy of formation at 0K as function of the composition in the μ phase has been plotted in *Figure 69* for a better overview of the stability of the end-members.

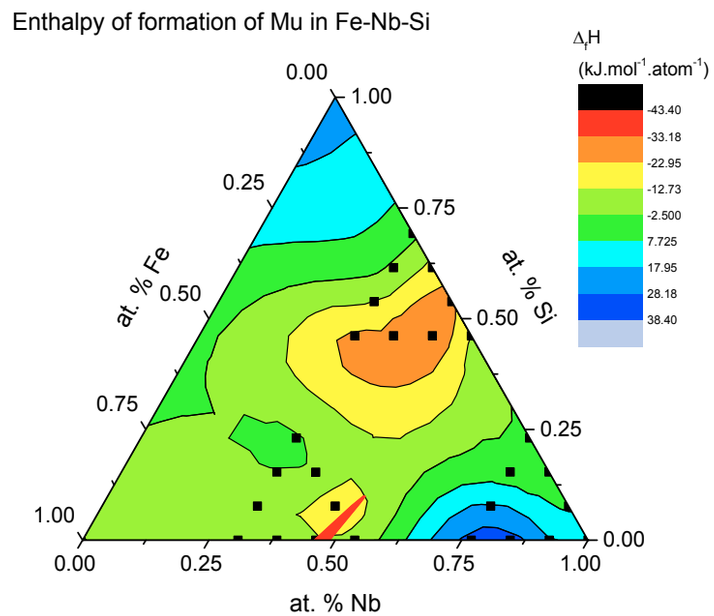

Figure 69 – Mapping of the stability of the end-members of the μ phase calculated by DFT at 0K. The different end-members are represented by the black square. The homogeneity range of the μ phase at 1000°C from Wang et al. [15] *is given in red for comparison.*

In general, the end-members with ideal compositions on the Nb-Si side are favorable (e.g. Nb_7Si_6 and Nb_6Si_7). The addition of Fe stabilizes these end-members. As an example $FeNb_6Si_6$ (Fe:Nb:Nb:Si) which is highly favorable, this end-member has the Nb in the 6c positions (favorable). The $SiNb_6Fe_6$ end-member is less negative, so Si has a site preference on the 18h Wyckoff position.

Fe is not favorable in the 6c positon. Si is more favorable at this position (see Fe:Nb:Si:Fe and Fe:Nb:Fe:Si).

1.3 Ternary phases

The enthalpies of formation of the ternary compounds have been computed by DFT in order to get a first idea of the stability of the compounds and to avoid to have to guess them. The compounds with mixed occupation on certain Wyckoff positions have not been calculated by DFT (e.g. $Fe_4Nb_4Si_5$ and $FeNb_2Si_2$). The data of the energy of the compounds and their lattice parameters are reported in Table 47. *The lattice parameters are compared with the experimental data available from the literature (given in brackets). Only a small deviation of the calculated/experimental lattice parameters can be noticed. Three of the ternary compounds (i.e. FeNbSi, $Fe_4Nb_4Si_7$ and $FeNbSi_2$) have similar enthalpies of formation, which is consistent with their respective position in the phase diagram.*

Phase	*k-mesh points*	Δ	Δ			

Table 47– Enthalpy of formation of the ternary compound in Fe-Nb-Si phase diagram. The lattice parameters on brackets are the experimental data from literature for comparison.

2. Thermodynamic optimization of the phase diagram

Using the binary phase boundary systems and the calculated enthalpies of formation of the end-members the calculated phase diagram is shown in *Figure 70.*

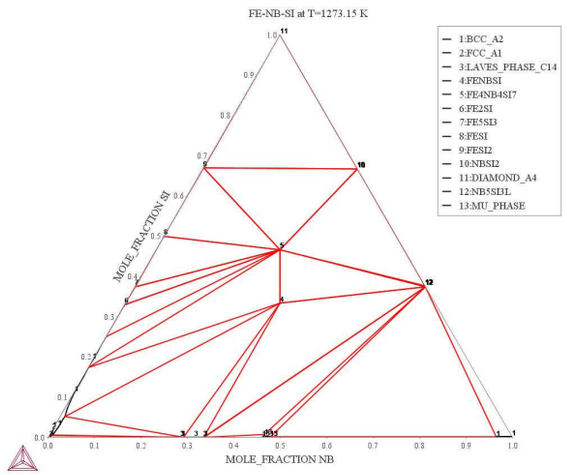

Figure 70 – Calculated isothermal section of the Fe-Nb-Si phase diagram at 1000°C without optimization.

Using only the DFT calculations, the phase diagram was calculated at 1000°C (*Figure 70*), four of ternary compounds are not shown in this calculation. In addition, the dissolution of Si in the Laves and μ phases on the Fe-Nb rich side is not shown.

At first the DFT calculations of the ternary compounds were used without any modification. The enthalpies of formation of the two ternary compounds which were not calculated by DFT (i.e. $Fe_3Nb_4Si_5$ and $FeNb_2Si_2$) were estimated to be similar to the other phases in the surrounding (i.e. $NbFeSi_2$, $Nb_4Fe_4Si_7$ and NbFeSi). The starting values were taken around 60 $kJ.mol^{-1}.atom^{-1}$. Temperature dependences to the enthalpies of formation were introduced to stabilize or destabilize certain phases. Nevertheless no temperature dependences were used for the description of $Fe_3Nb_4Si_5$ and $FeNb_2Si_2$.

In the Nb-rich corner, $FeNb_4Si$ is not shown in the non-optimized phase diagram. This phase was stabilized by introducing negative temperature dependence to its enthalpy of formation.

2.1 Dissolution of Si in the Laves phase

As Si should dissolve into the ternary system, therefore ternary interactions parameters were introduced. The interaction parameter $^0L^{C14}$(Fe,Si:Nb) was introduced allowing dissolution of Si into the Laves phase. A second ternary interaction parameter $^0L^{C14}$(Fe,Si:Fe) was then introduced to simulate the widest range of the homogeneity of the Laves phase. For both interaction parameters, a linear temperature dependence was used. Their respective values are given in *Table 48.*

2.2 Si in the μ phase

The dissolution of Si is not featured in the calculated phase diagram obtained from the DFT calculations. In order to dissolve Si in the μ [illegible]

[illegible]

2.3 Results of the thermodynamic assessment

For the first time, a thermodynamic assessment is given for the Fe-Nb-Si phase diagram. This assessment is only tentative as further experimental data would be required for a full assessment of this system. For example, liquidus and invariant reaction data would be of great importance in order to fix the liquid phase and the temperature dependence of the different phases.

Parameters obtained for the optimization of the phase diagram are given in *Table 48.*

Phase	Thermodynamic parameters	Remark
Fe-Nb	-	[40]
Fe-Si	-	[175]
Nb-Si	-	[75]
C14 (Fe,Si)$_2$Nb	${}^{0}L^{C14}_{Fe,Si:Fe} = -410000 - 10 \times T$	Optimized
	${}^{0}L^{C14}_{Nb,Si:Nb} = -320000$	Optimized
	${}^{0}L^{C14}_{Fe,Si:Nb} = -481000 - 35 \times T$	Optimized
μ	${}^{0}G^{\mu}_{Si:Nb:Nb:Fe} = -327728 - 100 \times T$	Optimized
	${}^{0}L^{\mu}_{Si:Nb:Fe,Fe} = -120000$	Optimized
FeNbSi	${}^{0}G^{FeNbSi} = -178680 - 7 \times T$	Optimized
FeNbSi$_2$	${}^{0}G^{FeNbSi_2} = -232160$	DFT
FeNb$_2$Si$_2$	${}^{0}G^{FeNb_2Si_2} = -320000$	Optimized
Fe$_3$Nb$_4$Si$_5$	${}^{0}G^{Fe_3Nb_4Si_5} = -743500$	Optimized
Fe$_4$Nb$_4$Si$_7$	${}^{0}G^{Fe_4Nb_4Si_7} = -894000 + 60 \times T$	Optimized
FeNb$_4$Si	${}^{0}G^{FeNb_4Si} = -172020 - 45 \times T$	Optimized

Table 48 – Optimized parameters for the thermodynamic description of the Fe-Nb-Si system.

It results the present phase diagrams given at 1000 and 1200°C (*Figure 71* and *Figure 72*, respectively) which are compared with some literature data.

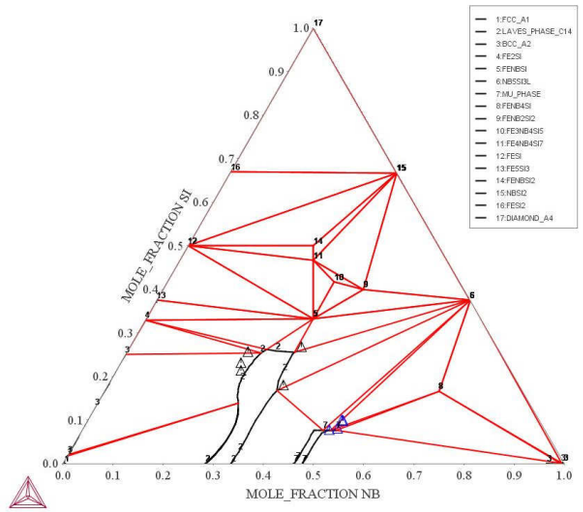

Figure 71 - Calculated isothermal section at 1000°C in comparison to experimental data given by Wang et al. [15]*, triangle symbols in black for the Laves phase and in blue for the μ phase.*

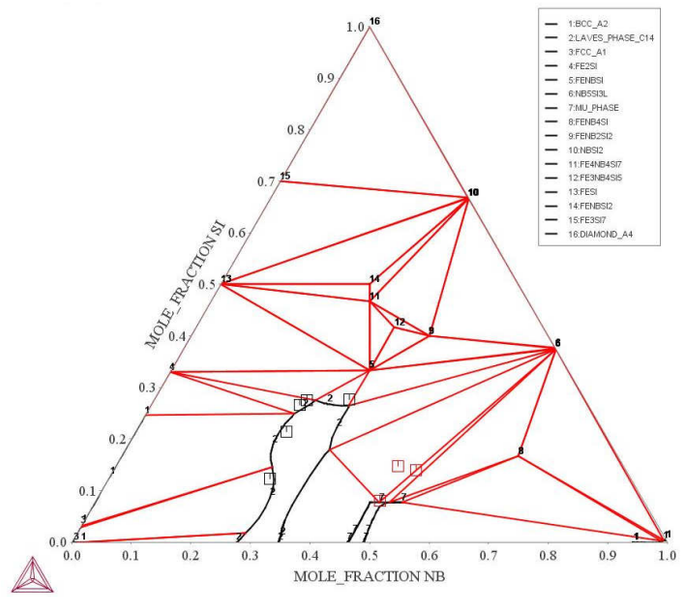

Figure 72 – Calculated isothermal section given at 1200°C in comparison with data from Wang et al., black squares (Laves phase), red squares (μ phase).

There is an overall good agreement of the calculated phase diagram with experimental data (*Figure 71* and *Figure 72*). The dissolution of Si into the μ phase is lower in the calculated phase diagram. Further optimization of this phase would be required for a better description of the μ phase.

The calculated phase diagram shows an equilibrium C14+Fe_2Si+FeNbSi which is not shown by Wang et al. [15], this is due to the description of Fe_2Si given by Yuan et al. [175] in the description of Fe-Si system.

In the highest isothermal section the laves phase and the FeNbSi ternary phase are experimentally in equilibrium with the liquid [15], but this is not shown in the calculated phase diagram.

Conclusion

A tentative optimization of the Fe-Nb-Si phase diagram has been given here. There is an overall good description of the phase equilibria. Nevertheless, for an improvement of the thermodynamic optimization of this phase diagram further experimental data are necessary. At first, the liquidus projection of the present phase diagram is required as well as the temperature dependence of the thermodynamic properties of the ternary compounds.

Chapter VII – Microstructure of alloys and phase equilibria of sub-system Laves phase containing systems

In the present work, phase equilibria of binary and ternary systems containing Laves phase have been determined by experiment and/or modeling. The knowledge of phase equilibria is of great importance when developing materials with specific properties.

Many technically relevant materials are composed of about 10 to 15 elements, whereas the study of phase equilibria is often restricted to a maximum of four elements (as it is not easy to visualize with more elements). Nevertheless, it is often possible to predict the formation of certain phases by studying the binary, ternary or quaternary phases as each individual phase will be formed with less than 5 elements.

The studies of sub-systems like Cr-Nb, Fe-W, Cr-Fe-Nb and Fe-Nb-Si in the present study are compared with the development and studies of model alloys which can be then in successful cases being produced at an industrial scale.

During the development of new alloys, different compositions of elements are tried or the additions of new elements are studied.

I. Development of laves phase strengthened ferritic steel

During the development of the high chromium ferritic steel Crofer 22H, different additions of elements have been tested in order to check their effect on the properties of new steels, especially oxidation behavior and creep strength. Froitzheim et al. [142] have proposed different additions of element in order to promote the formation of strengthening Laves phase particles. In this study, the direct influence of sub-system phase diagram was pointed out. In the alloy reference Crofer 22AP, where the ferritic matrix is composed of α

Figure 73).

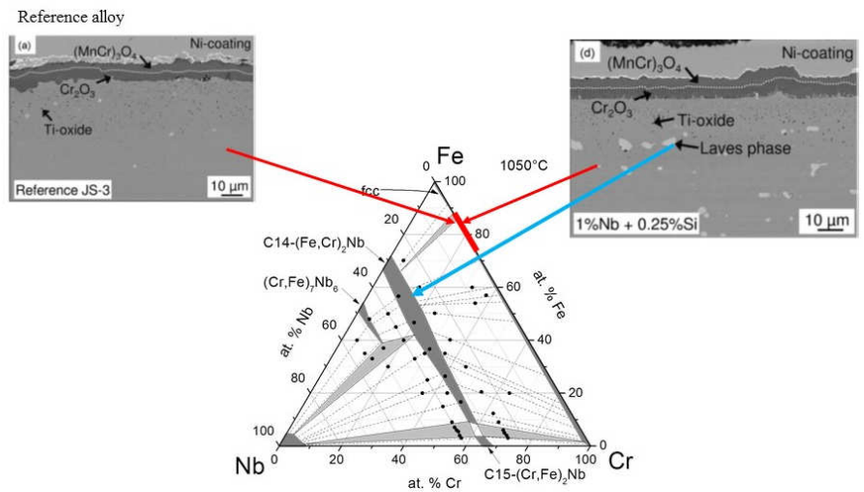

Figure 73 – Comparison of the microstructure of model alloy [142] *with the Cr-Fe-Nb phase equilibria (present work). The two microstructure images are taken from Froitzheim et al.* [142]*, the left microstructure is the reference alloy (model alloy with a similar composition as Crofer APU) and on the right microstructure of the model alloy with the addition of Nb and Si.*

The Laves phase in the newly developed alloy as given by Froitzheim et al. [142] has a similar composition as expected from the Cr-Fe-Nb phase equilibria. Si dissolves in the Laves phase. The formation of the Laves phase is promoted by Si, the comparison with the ternary Cr-Fe-Nb system from the present work is done in a lower order system. As mentioned by the authors [142] "*There are limited thermodynamic data available for the Fe-Cr-Nb-Si system*" which limits the understanding of the chemical driving forces behind the formation of the different phases. The only article related to the quaternary phase diagram is given by Vilasi et al. [179] but they do not provide a lot of information about Si dissolving in the ternary Laves phase. Nevertheless, according to several studies on the Laves phase, Si promotes the formation of the Laves phase, stabilized it and occupies the position of Fe and Cr in the crystal structure. The overall Laves phase formula is written as $(Fe,Cr,Si)_2Nb$.

II. Development of Nb-silicide

Even if the goal of the present study is an improvement of the thermodynamic database for steel, this database could also be used for the development of other materials (i.e. Ni-superalloys, Nb-silicides) as soon as they contain the same elements and the phases of interest as in the present study.

For the replacement of Ni-superalloys, Nb is one of the materials which is attractive for high temperature structural materials but has a poor oxidation resistance.

**In order to develop further Nb alloys, several authors have tested different alloy composition as well as their casting process. Zhang et al. [181] have studied the addition of Fe on such alloys in order to improve the oxidation resistance. The addition of Fe into Nb-silicides has promoted the formation of Fe_4Si compound. This phase was observed in the Fe-Nb-Si phase diagram [15] (*Figure 74).*

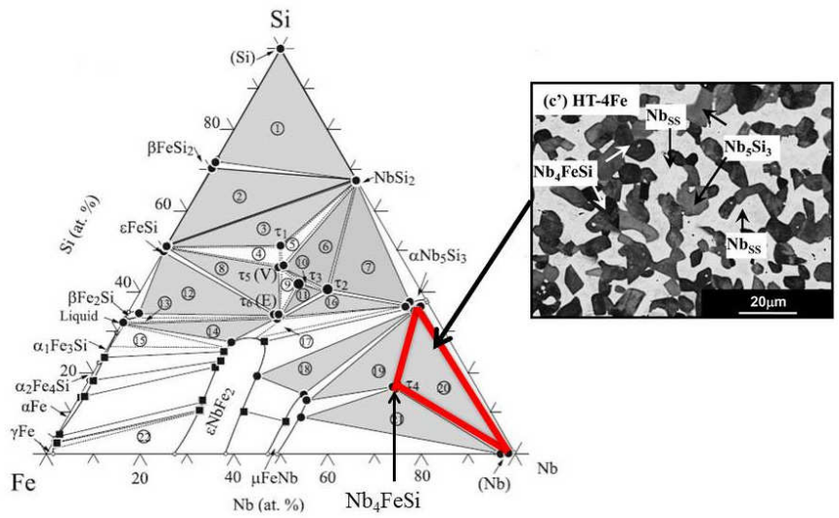

Figure 74 –Comparison of the Fe-Nb-Si phase diagram (reproduced from Wang et al. [15]) with Fe+Nb-silicide microstructure (micrograph reproduced from [181]*). The three phase field region Nb+Nb_4FeSi+Nb_5Si_3 is observed on the micrograph.*

III. Phase diagram vs ferritic steel alloy

The present comparison between model alloys and sub-systems of binary, ternary and quaternary alloys is of great importance for the development of new materials. Nevertheless, in addition to the different systems studied in the present work, other systems containing Laves phases are of great importance but are not well studied in the literature. For more clarity, the different sub-systems of Laves phase containing systems are reported in *Figure 75*. A color code is used to show which systems have been already studied and which systems would need to be studied for better understanding of the Laves phase containing systems in Crofer 22H and similar ferritic steels.

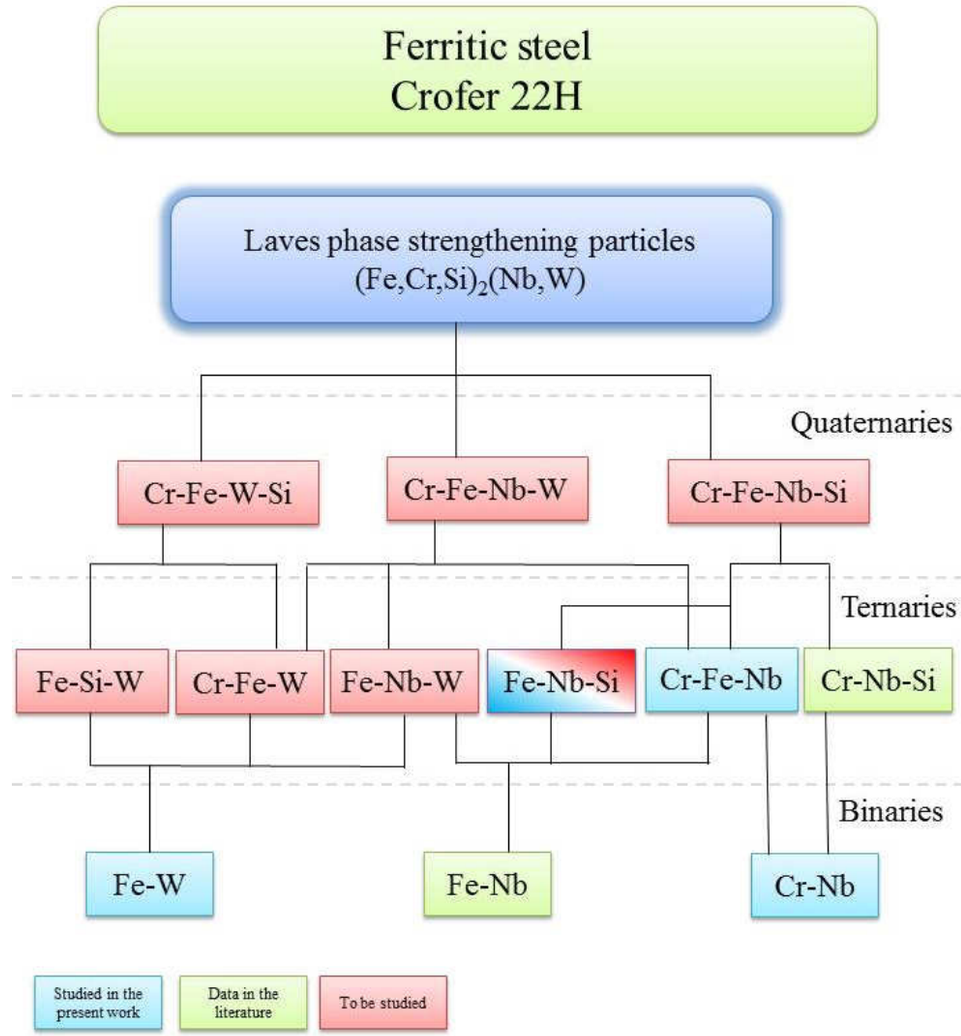

Figure 75 - Schematic representation of the different sub-systems containing Laves phase in Crofer 22H.

As can be seen on *Figure 75*, several ternaries and quaternaries systems would require further investigations. A careful literature survey would reveal where there is a need for investigation (i.e. experimental and/or modelisation). At first, it would be relevant to study the ternary Fe-W-Si and Cr-Fe-W.

Conclusion

In the present work, several methods have been used for the thermodynamic assessment of the phase diagrams related to ferritic steels containing Laves phases e.g. Crofer 22H. For the different systems several approaches were used to obtain suitable input data for the thermodynamic modeling.

In the two binary systems Cr-Nb and Fe-W, the available experimental data were sufficient and a computational approach based on DFT was used for the determination of the energies of formation of the compounds present in the system. In the Fe-W system, a new approach was tried by using phonon calculations to model the different end-members according to the chosen sublattice models. It was found that to model a disordered phase, the use of phonon calculation could lead to the creation of an unrealistic miscibility gap. So these data should be treated with care in thermodynamic modeling. In this system, two optimizations of the phase diagrams have been proposed which can be used for higher order systems.

In ternary systems Cr-Fe-Nb and Fe-Nb-Si, the literature survey revealed a lack of experimental data. It was therefore decided to reevaluate these phase diagrams experimentally. In the Fe-Nb-Si phase diagram, new experimental data from the literature became available during the time of the present work. So these data were used for the thermodynamic modeling. In addition DFT calculations were performed for the determination of the energy of formation of the different compounds. These data were of great help for the ternary compounds. Using these data (i.e. experimental and DFT), a partial thermodynamic modeling is given in the present work. Nevertheless, further experimental investigations are required for the determination of the liquidus surface and of the temperature dependence of the thermodynamic properties of the different phases for a suitable thermodynamic modeling of the Fe-Nb-Si system. In addition further thermodynamic experiments (e.g. calorimetry, KEMS measurements) would be of great help for a successful thermodynamic optimization.

In the Cr-Fe-Nb ternary system, experimental work was done to obtain different isothermal sections to have a suitable picture of the system. DFT calculations were done for the determination of the energy of

μ

μ

Bibliography

[1] J. Quadakkers, L. Niewolak, P. Ennis, Offer 22H, 2006, Patent Numbers: PCT/DE2007/000166, WO2007093148-A1; DE102006007598-A1 (18.2.2006).

[2] B. Kuhn, C.A. Jimenez, L. Niewolak, T. H□ttel, T. Beck, H. Hattendorf, et al., Effect of Laves phase strengthening on the mechanical properties of high Cr ferritic steels for solid oxide fuel cell interconnect application, Mater. Sci. Eng. A. 528 (2011) 5888–5899.

[3] J.H. Froitzheim, Ferritic Steel Interconnectors and Their Interactions with Ni Base Anodes in Solid Oxide Fuel Cells (SOFC), Forschungs, Forschungszentrum Julich GmbH - Zentralbibliothek, Verlag, 2008.

[4] B. Kuhn, M. Talik, L. Niewolak, J. Zurek, H. Hattendorf, P.J. Ennis, et al., Development of high chromium ferritic steels strengthened by intermetallic phases, Mater. Sci. Eng. A. 594 (2014) 372–380.

[5] A. Agha□ani, F. Richter, C. Somsen, S.G. Fries, I. Steinbach, G. Eggeler, On the formation and growth of Mo-rich Laves phase particles during long-term creep of a 12% chromium tempered martensite ferritic steel, Scr. Mater. 61 (2009) 1068–1071.

[6] C. Asensio, a. Chyrkin, L. Niewolak, V. Konoval, H. Hattendorf, B. Kuhn, et al., Subsurface Depletion and Enrichment Processes During Oxidation of a High Chromium, Laves-Phase Strengthened Ferritic Steel, Electrochem. Solid-State Lett. 14 (2011) P17.

[7] □T. Chiu, C.-K. Lin, Effects of Nb and W additions on high-temperature creep properties of ferritic stainless steels for solid oxide fuel cell interconnect, J. Power Sources. 198 (2012) 149–157.

[8] J-O Andersson, T. Helander, L. H□glund, P. Shi, B. Sundman, THERMO-CALC □ DICTRA, Computational Tools For Materials Science, Calphad. 26 (2002) 273–312.

[9] P. Paufler, Early work on Laves phases in East Germany, Intermetallics. 19 (2011) 599–612.

[10] F. Stein, M. Palm, G. Sauthoff, Structure and stability of Laves phases . Part I. Critical assessment of factors controlling Laves phase stability, Intermetallics. 12 (2004) 713–720.

[11] F. Stein, M. Palm, G. Sauthoff, Structure and stability of Laves phases part II□structure type variations in binary and ternary systems, Intermetallics. 13 (2005) 1056–1074.

[12] D.J. Thoma, J.H. Perepezko, A geometric analysis of solubility ranges in Laves phases, J. Alloys Compd. 224 (1995) 330–341.

[13] I. Ansara, T.G. Chart, A.F. Guillermet, F.Hayes, J.R. Kattner, D.G. Pettifor, et al., Phase Characteristics and Thermodynamic elling of the Concentration Dependence, Calphad. 21 (1997) 171–218.

[illegible]

σ

μ σ σ

η [illegible]

[illegible]

[illegible]

[

□

Acknowledgements

Doing a PhD is a bit like hiking in the mountains. It is a lot of going up and down. Being on top of the mountain is exiting and allows to see the next climbs. Nevertheless, it is often that we are at the bottom of the mountain and that we do not know how to reach the top of the next mountain. Furthermore a lot of difficulties can be encountered and it is not with a straight line that we are able to climb.

It is often that I have been at the bottom of the mountains during my PhD, but I could count on the help of many people, in order to be able to climb and not fail. For all these helps I would like to acknowledge:

First, I would like to thanks Prof. Singheiser for giving me the opportunity of working in his institute, also for his pleasing leadership and for all his help, advices and discussions given for the thesis.

I would also like to thanks Dr. D. Grüner for his advices and the measurements. In addition, I would like to thanks colleagues for their help carrying the measurements Dr. E. Wessel, V. Gutzeit, J. Bartsch and Mr. Ziegner from IEK-2 and C. Thomas from PGI-5 institute.

Many thanks from colleagues of other institutions for their help during my PhD: Dr. A. Watson from University of Leeds, Prof. K. Richter as well Dr. T.Reichman from University of Vienna for their help in Calphad and XRD evaluations, respectively. I would also like to thank Dr. A. Khvan from MISIS (Russia) for measurements as well as her help in Calphad.

I would like to give my special thanks to Dr. Bengt Hallstedt for all his advices and useful discussions for the Calphad part.

I would to thanks Dr. Angus Gray-Weale for hosting me during my stay in Melbourne and for his kind advices. And also all the colleagues there, for the nice time I spent with them, I will not forget our quiz time.

In addition, I would like to address my thanks to my colleagues of the thermochemistry group and especially Siau as a nice office mate and Nathan for all his happy and craziness as an institute mate.

Band / Volume 261
Influence of the surface composition and morphology on the reflectivity of diagnostic mirrors in a fusion reactor
M. Matveeva (2015), 158 pp
ISBN: 978-3-95806-051-7

Band / Volume 262
Very High Cycle Fatigue Behavior of Riblet Structured High Strength Aluminum Alloy Thin Sheets
S. Stille (2015), XII, 123 pp
ISBN: 978-3-95806-054-8

Band / Volume 263
The role of soil heterogeneity on field scale evapotranspiration: 3D integrative modelling and upscaling of root water uptake
K. Huber (2015), xii, 128 pp
ISBN: 978-3-95806-057-9

Band / Volume 264
Strontium-Diffusion in Cer-Gadolinium-Oxid als Degradationsmechanismus der Festoxid-Brennstoffzelle
T. Mandt (2015), iii, 160 pp
ISBN: 978-3-95806-058-6

Band / Volume 265
Cluster analysis of European surface ozone observations for evaluation of MACC reanalysis data
O. Lyapina (2015), 187 pp
ISBN: 978-3-95806-060-9

Band / Volume 266
Real-time quantification of oxygen isotope exchange between carbon dioxide and leaf/soil water in terrestrial ecosystems with laser-based spectroscopy
L. Gangi (2015), XX, 156 pp
ISBN: 978-3-95806-061-6

Band / Volume 267
Secondary Uranium Phases of Spent Nuclear Fuel – CoXnite, $USiO_4$, and Studtite, UO_44H_2O – Synthesis, Characterization, and Investigations Regarding Phase Stability
S. Labs (2015), 153, xlii pp
ISBN: 978-3-95806-063-0

Band / Volume 268
Chemische, verfahrenstechnische und ökonomische Bewertung von Kohlendioxid als Rohstoff in der chemischen Industrie
A. Otto (2015), viii, 272 pp
ISBN: 978-3-95806-064-7

Band / Volume 269
Energetische und wirtschaftliche Optimierung eines membranbasierten Oxyfuel-Dampfkraftwerkes
Y. Nazarko (2015), IV, 337 pp
ISBN: 978-3-95806-065-4

Band / Volume 270
Investigation of light propagation in thin-film silicon solar cells by dual-probe scanning near-field optical microscopy
S. Lehnen (2015),120 pp
ISBN: 978-3-95806-066-1

Band / Volume 271
Characterization of soil water content variability at the catchment scale using sensor network and stochastic modelling
W. Qu (2015), XVI, 123 pp
ISBN: 978-3-95806-067-8

Band / Volume 272
Light Absorption and Radiative Recombination in Thin-Film Solar Cells
T. C. M. Müller (2015), ii, 146 pp
ISBN: 978-3-95806-068-5

Band / Volume 273
Innenbeschichtung poröser Körper mittels Atomlagenabscheidung zur Redoxstabilisierung anodengestützter Festoxidbrennstoffzellen
T. Keuter (2015), XII, 133 pp
ISBN: 978-3-95806-069-2

Band / Volume 274
Thermochemical Modeling of Laves Phase Containing Ferritic Steels
A. Jacob (2015), 200 pp
ISBN: 978-3-95806-070-8

Weitere ***Schriften des Verlags im Forschungszentrum Jülich*** unter
http://wwwzb1.fz-juelich.de/verlagextern1/index.asp

Energie & Umwelt
Energy & Environment

274

Thermochemical Modeling of Laves Phase Containing Ferritic Steels

Aurélie Jacob

Member of the Helmholtz Association

JÜLICH FORSCHUNGSZENTRUM

Energie & Umwelt / Energy & Environment
Band / Volume 274
ISBN 978-3-95806-070-8

JÜLICH FORSCHUNGSZENTRUM

Thermochemical Modeling of Laves Phase Containing Ferritic Steels

Aurélie Jacob

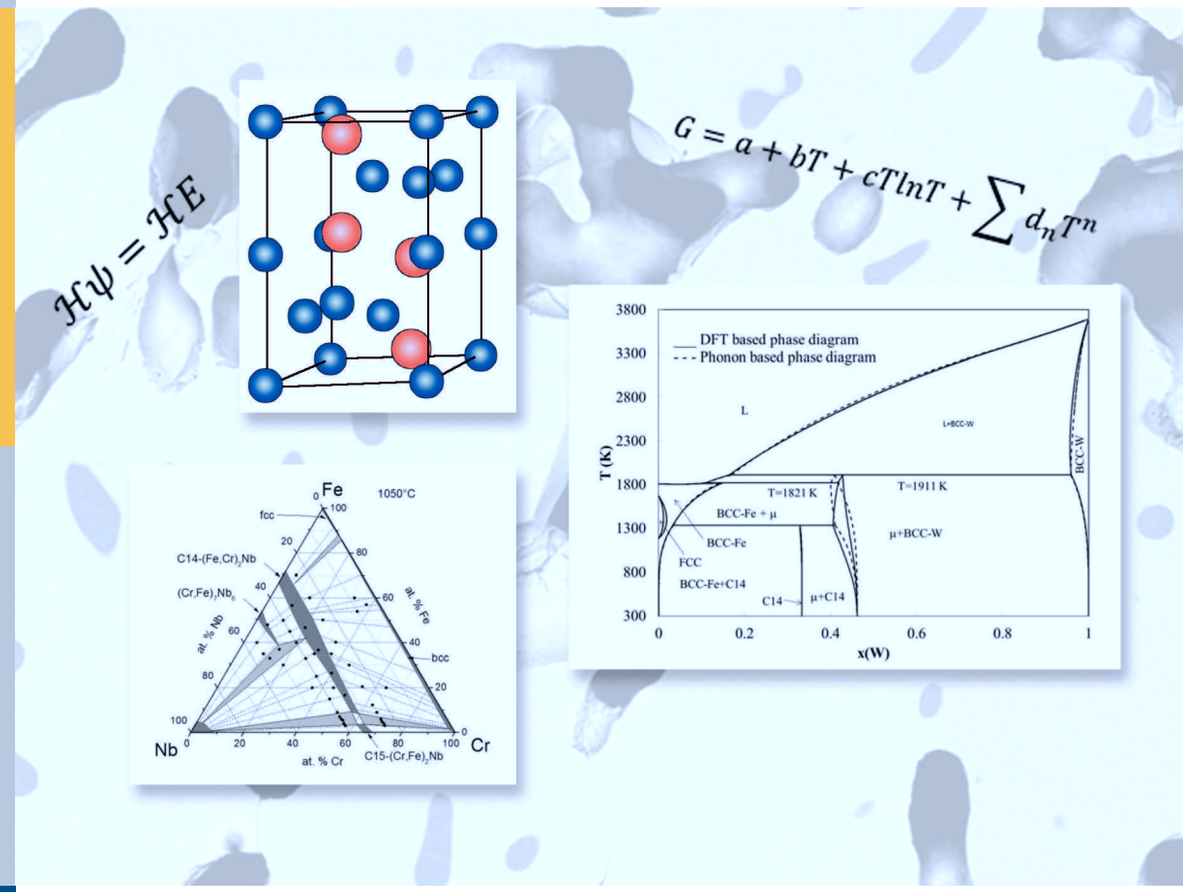

Energie & Umwelt / Energy & Environment
Band / Volume 274
ISBN 978-3-95806-070-8

JÜLICH FORSCHUNGSZENTRUM